SCALING AND PATTERN FORMATION IN CONDENSED MATTER SYSTEMS

BY

PAK YUEN CHAN

B.S., The Chinese University of Hong Kong, 2003

DISSERTATION

Submitted in partial fulfillment of the requirements
for the degree of Doctor of Philosophy in Physics
in the Graduate College of the
University of Illinois at Urbana-Champaign, 2007

Urbana, Illinois

Abstract

In this dissertation, I present analytical and numerical work regarding the scaling behavior of three physical systems, with increasing levels of complexity.

I begin by analyzing the scaling behavior of Griffiths ferromagnets near the Griffiths-paramagnetic transition point. By deriving the asymptotic behavior of the magnetization of the system using an ansatz for the Yang-Lee zero density, which is a generic form of the density with the presence of disorder, I find that the scaling behavior of Griffiths ferromagnet is completely different from that of conventional (pure) ferromagnets—the scaling is dominated by an essential singularity in the external magnetic field, due to the ferromagnetic response of arbitrarily large pure (disorder free) ferromagnetic islands in the system. Excellent agreement is found by comparing this prediction to the experimental data on $La_{0.7}Ca_{0.3}MnO_3$, from which I also extract the critical exponents.

Next I report on studies of landscape formation due to carbonate precipitation near geothermal hot springs. This system forms complex patterns due to coupling between the fluid flow, precipitation kinematics and landscape dynamics. I formulate a mathematical framework to describe this complex geological process. I derive analytically the shape and stability of the spherically symmetric domes. The solution agrees with field observations and simulation results, up to a point at which surface tension becomes important and the fluid breaks into rivulets. Although our theory does not take into account surface tension, it does describe its own failure and predicts a scaling behavior about the angle at which rivulets begin. This scaling behavior is

confirmed by computer simulations.

In addition, I apply a similar conceptual framework to study the formation and stability of stalactites in limestone caves. The shape of stalactites is calculated and the solution is found to be unconditionally stable, as opposite to the unstable dome solutions. We attributed this difference in stability to the difference roles of surface tension in the two systems. By studying the linear stability of a uniform sheet of fluid flowing down a constant slope, moreover, I show that our theory gives results that are consistent with the scale-free terraced landscapes observed.

In the final project, I study complex, multiscale patterns in polycrystalline materials, with the phase field crystal (PFC) model. I first show that the PFC model can be rewritten in terms of complex amplitudes, using renormalization group concepts. Such a representation incorporates the correct form of nonlinear elasticity. I then analyze the plastic properties of the model by applying a shearing force. Dislocation creation, annihilation and avalanches are observed, resembling the scaling behavior in driven ferromagnetic systems and other dislocation avalanching systems. Critical exponents are extracted from power laws extending over 5 decades.

I extend the PFC model to accommodate actual atomic configurations and vacancies by forbidding the order parameter to be negative. In so doing, the PFC model becomes a molecular dynamics simulation machine. I use the PFC model to simulate a liquid and reproduce the correct form of the two-point correlation functions. Finally, I extend the PFC model to describing binary systems. The resulting theory describes both atomic hopping events on microscopic scales and diffusion on macroscopic scales. It also reproduces the activated Arrhenius form of the diffusion coefficient. These developments indicate that the PFC model is a flexible and reliable approach to study multiscale phenomena in polycrystalline materials.

To my parents

The eternal mystery of the world is its comprehensibility.

—Albert Einstein (1879-1955)

Acknowledgments

First of all, I would like to thank the Department of Physics in the University of Illinois at Urbana-Champaign for giving me this opportunity to pursue my Ph.D. in this wonderful department. My professional experience here has been eye opening and brain rewiring.

I would like to express my deepest gratitude to my adviser, Prof. Nigel Goldenfeld. He has always been a patient, enthusiastic and resourceful adviser to me, both professionally and personally. Besides all the technical insights and skills, he has taught me how to do science in a fun way. I thank him for letting me contribute to the research projects I present in this dissertation, from which I have made my first steps into the exciting world of multidisciplinary research. In fact, the word 'multidisciplinary' does not sound accurate to describe his research, as he always overlooks boundaries between different domains of science and chases only after the natural phenomena he is interested in, be they physics, biology, geology, finance, or even psychology. His broad interest and appetite, which can be summarized by his official research interest posted on his webpage—*interested in everything*—will have an everlasting impact on my understanding of what it means to be a scientist. His unique way of looking at nature through the lens of renormalization group, together with his beloved minimal modeling and universality, have completely altered my understanding of complex systems.

I appreciate his patience and willingness to share with me and advise me on several personal occasions, as well as his invaluable advice on my career.

I am also grateful to four other professors in the University of Illinois at Urbana-Champaign. Prof. Bruce Fouke, with whom I worked in the Yellowstone project, has shown me what is meant by "getting your hands dirty" and understanding experimental data in every single detail. The successful communication and collaboration between Nigel and Bruce had set me a role model of how to work with people, which, I am sure, is a skill that I desperately need in my future. Prof. Jonathan Dantzig, who taught me not to just focus on theoretical beauty, but to focus also on what the end users of the theory are interested in, has always be a friendly and knowledgable adviser. Prof. Myron Salamon has shown me the necessity of knowing, down to earth, various theories before you can understand any experimental data. Prof. Karin Dahmen, whose expertise in non-equilibrium critical and scaling phenomena had fueled the last part of my dissertation, has always been friendly and enthusiastic about my early not-so-clean data sets.

I thank Prof. Michael Stone, Prof. Smitha Vishveshwara and Prof. Lance Cooper for being my committee.

I would also like to thank the other members of Nigel's group. Kalin Vetsigian, who was my officemate for the first two years, has set an extraordinary example of what a successful graduate student should be like early in my graduate studies. John Veysey's collaboration in the Yellowstone project has been invaluable. His commitment to the project forced me to try my best on my part. Nicholas Guttenberg's exceptionally fluent modeling and programming skills have always be inspiring and amazing, to the extent that I think his Linux box is an extended part of his brain (only that it is replaceable and upgradable!). I thank Thomas Butler for bearing with my Cantonese in our shared office for two years, as well as various interesting discussions inside and outside physics, including climbing, traveling and religion. I also thank Nicholas Lee-Ping Chia, who is always a friendly guy to hang around, for introducing me to various concepts about gene alignment. I thank David Reynolds' discussion on the

statistical mechanical and elastic properties of the phase field crystal (PFC) model. His broad exposure in condensed matter has helped me a lot.

I would like to thank other collaborators, in no particular order: Michael Kandianis for teaching me water chemistry and carbonate precipitation; Badrinarayan Athreya for introducing the phase field crystal model and its complex amplitude representation; Georgios Tsekenis for his systematic notes and presentation on plastic flows, which did me a great favor in comprehending the material; and Zhi Huang for working with me on adaptive mesh refinement and walking me through tedious C++ code.

I would like to thank Prof. Ming Chung Chu in the Chinese University of Hong Kong, without whose passion and effort in promoting the Summer Undergraduate Research Exchange (SURE) program, I would not have been able to come to the States and pursue my studies.

I would not be able to finish this program without friendship. To this end, I would like to thank Stefanos and Minsu for their friendships. Thanks to all members of ChaTown—Stephen, Man Hong, Edwin, Nicole and Florrie; you guys have given me some of the most memorable moments in Champaign-Urbana. Thanks to Keith, Tommy, Thomas and Wai, whose presence made me feel like I was still in CUHK. Thanks to Louis and Bubble, who are my dearest friends in Hong Kong.

Champaign-Urbana is my spiritual home. I thank God for bringing me to Him. I am indebted to Rev. Michael McQueen, whose teaching and guidance, through our weekly meetings in the last two years, have shown me what a Christian should be like. I especially thank him for his teaching, patience, transparency and friendship (as well as his coffee and cakes!). I thank all members of the Illini Chinese Christian Fellowship (ICCF), especially Jacky, Edwin, Shirley, Maria, Chung Wong, David, George, Christine, Chuen, Isaac, Victor, Elizabeth, Alex, Jessica, Charis, Helen, Miceala, Matthew, Mandy and Chung Ko. You guys are just awesome! Thanks for

your discussion, sharing, support and fun. I could not imagine my life here without you. Thanks also to Champaign Chinese Christian Church (CCCC).

I thank my parents for bringing me into existence and taking care of me. Besides countless wonderful things they did and prepared for me, I especially thank them for their love, support, encouragement, understanding and granting me freedom to do whatever I am interested in.

Last, but not least, I thank my wife-to-be, Florrie, for her 24/7 love and encouragement. I could hardly survive this process without her.

This material is based upon work supported by the National Science Foundation through Grant No. NSF-DMR-01-21695 and NSF-EAR-0221743. Any opinions, findings, and conclusions or recommendations expressed in this publication are those of the author(s) and do not necessarily reflect the views of the National Science Foundation.

Table of Contents

List of Figures

Chapter 1

Introduction

In this dissertation, we discuss research problems ranging from the scaling properties of disordered ferromagnets, to geophysical precipitation pattern formation, to multiple scale, non-equilibrium phenomena in materials. The overarching theme that unifies these topics is that they all exhibit scaling behavior[1] in certain regimes. The first project concerns the scaling behavior of a disordered system, while the other two concern the scaling behavior in non-equilibrium systems.

When a system exhibits scaling behavior, the physical observable, or the function that defines the system, such as the free energy of a thermodynamic system, becomes a generalized homogeneous function[2], *i.e.,* if we change the overall scale of the function, the effect is the same as scaling all the variables in a specific way. Mathematically, for a function of two variables $f(x, y)$, we have

$$bf(x, y) = f(b^{\alpha}x, b^{\beta}y), \tag{1.1}$$

where b is an arbitrary positive number, α and β are constants called the critical exponents. There are at least four implications to this relation. First, because $f(x, y)$ scales, all its derivatives satisfy similar scaling relations. For example, for the derivative $f_x(x, y) \equiv \partial_x f(x, y)$, we have

$$bf_x(x, y) = b^{\alpha}f_x(b^{\alpha}x, b^{\beta}y), \tag{1.2}$$

which can be written as

$$\bar{b} f_x(x, y) = f_x(\bar{b}^{\bar{\alpha}} x, \bar{b}^{\bar{\beta}} y), \tag{1.3}$$

where we defined $\bar{b} \equiv b^{1-\alpha}$, $\bar{\alpha} \equiv \alpha/(1-\alpha)$ and $\bar{\beta} \equiv \beta/(1-\alpha)$. Second, the critical exponents that characterize those derivatives are not independent, because they are all derived from $f(x, y)$. The relations between these derived critical exponents are called the scaling laws. In our example, we note that all the critical exponents for the derivatives, such as $\bar{\alpha}$ and $\bar{\beta}$, are functions of α and β. Third, if all but one variable are set to zero, then the function becomes a power law in the remaining variable. If $x = 0$, for example, then the function $f(x, y)$ becomes a power law in y. This is because we can make the choice $b = y^{-1/\beta}$, and Eq. (1.1) becomes

$$f(0, y) = y^{1/\beta} f(0, 1). \tag{1.4}$$

Fourth, if we do not set any of the variables to zero and make the choice $b = y^{-1/\beta}$ again, then Eq. (1.1) becomes

$$\frac{f(x, y)}{y^{1/\beta}} = f\left(\frac{x}{y^{\alpha/\beta}}, 1\right) \equiv F\left(\frac{x}{y^{\alpha/\beta}}\right), \tag{1.5}$$

which is essentially a function of one variable, instead of two. This striking phenomenon of the reduction of the number of independent variables is called data collapse, because by plotting $y^{-1/\beta} f(x, y)$ against $x/y^{\alpha/\beta}$, the originally two dimensional data will collapse onto a single one-dimensional curve $y = F(x)$. These four properties of generalized homogeneous functions are the fingerprint of scaling behavior, and this is why scaling behavior is always associated with scaling laws, power law functions and data collapse.

The Ising model is among the first systems where scaling behavior was discovered. The free energy of the system, F, in general depends on both the temperature, T, and the external magnetic field, H, *i.e.,* $F = F(H, T)$. When the system is sufficiently close to the critical point, $T = T_c$ and $H = 0$, however, the system exhibits a scaling

behavior and the free energy is, instead of a function of two variables, a function of a single variable,

$$\frac{F}{t^{\beta+\beta\delta}} = F^{\pm}\left(\frac{H}{t^{\beta\delta}}\right), \tag{1.6}$$

where $t \equiv (T - T_c)/T_c$ is a reduced temperature, which measures how far the system is from the critical point, β and δ are two critical exponents and $F^{\pm}(x)$ are two scaling functions for $t > 0$ and $t < 0$ respectively. All the thermodynamic observables, such as the magnetization, the specific heat capacity and the susceptibility, then follow similar relations with their critical exponents related by various scaling laws.

Scaling behavior is very important. In fact, it is reasonable to say that the discovery of such phenomena and the development of the associated theory was one of the most significant advancements in theoretical condensed matter physics in the last 50 years. It took physicists about 30 years of research to discover the beautiful structures behind such phenomenology as power laws, scaling laws and data collapse. It triggered the development of the Renormalization Group[1], which forms the basis of many important concepts, such as universality, universality classes, relevant and irrelevant variables and minimal modeling. Beside providing a theoretical explanation for the existence of scaling behavior and universality, these ideas have penetrated many different domains of science, including high energy physics[3], condensed matter physics[1; 4], cosmology[5–8], fluid mechanics[9–11], solid mechanics[12; 13], non-equilibrium statistical mechanics[14–18], asymptotic methods in applied mathematics[1; 19; 20] and even quantitative finance[21; 22]. They have changed the way we do physics, or modeling in general, as we will see in the follow sections.

1.1 Universality

Why is scaling behavior important? There are two answers to this question. Historically, scaling behavior was important because even in principle, we did not know why

it arose, or how we could calculate the scaling functions and critical exponents. It posed a serious problem to theoretical physics. In retrospect, however, we know that scaling behavior is important because it is a manifestation of universal features of the system in question.

Scaling behavior is universal in three ways. First, unlike, say, the critical temperature of a ferromagnet, which depends on all sorts of microscopic details of the sample, such as crystal defects and the amount of impurities[1], scaling behavior is universal and does not depend on those microscopic details. A multi-crystalline ferromagnet with point defects, dislocations and irregular surfaces, for example, exhibits exactly the same scaling behavior as a perfectly periodic, defect free ferromagnet. Second, it does not depend on the kind of material. Properties of ferromagnets, such as the magnetic susceptibility, electric conductivity and thermal conductivity, are different for different materials, but the scaling behavior they exhibit are exactly the same, *i.e.,* they are characterized by the same critical exponents and scaling functions.[2] It is similar to the fact that a single ideal gas law can describe a variety of gases, and a single Navier-Stokes equation can describe all fluids. Third, scaling behavior is universal across physical systems. It is known that scaling behavior depends only on the dimensionality, symmetry and phenomenology of the system, but does not depend on how these are represented physically. Here, by using the term phenomenology, we are not referring to all the properties or behaviors of the system, but the essential ones. It is difficult to define which properties are essential independent of the context. In the context of statistical mechanical systems, however, phenomenology refers to the range of interaction of the spins or atoms, and any conservation laws. We will see other types of essential properties that we will also call phenomenology later, when we discuss turbulent fluid flow.

[1] If the amount of disorder and impurity is too large, they do play a role in determining the scaling behavior of ferromagnets. This is, in fact, the subject of the first project (see Chapter 2).

[2] For simplicity, we are here ignoring other classes of ferromagnets, such as the Heisenberg class.

A prime example of the last meaning of universality is the equivalence of the ferromagnetic-paramagnetic transition and the solid-liquid transition[1]. Although these two physical systems seem completely different, they have the same symmetry and phenomenology; they can both be described by a lattice model, with a local two-state order parameter at each site dictating the state of the atom, either spin up or down for the former system, or solid or liquid for the latter. And the ranges of interaction are the same in the two systems: the spins, or atoms, only interact with close neighbors. As a result, the two transitions have exactly the same set of critical exponents and scaling functions. These two systems are said to be in the same universality class.

In other words, scaling behavior depends only on the dimensionality, symmetry and phenomenology of the system; scaling is a robust and universal characteristic of a physical system.

1.2 Spherical Cows

Universality saves our life as physicists. Imagine if nature were detail-sensitive: we would have to include all the details into our model in order to describe any phenomenon. Any realistic model would then become incomprehensibly complicated, and we could hardly make any progress. But now, by the grace of universality, we can predict important and universal features of real systems using such simple models as the Ising model, which only captures the essential features in the system.

There is a saying, 'If physicists were to study a cow, they would first approximate it as a spherical cow.' This effectively captures how physicists study nature; we study idealized systems and ignore non-essential details. Now, universality allows physicists to do an even better, and yet simpler, job. In order to understand a cow, we could study a spherical chicken! (as long as the latter is easier to understand, of course.)

This is justified if the cow and the chicken share the same dimensionality, symmetry and phenomenology, *i.e.,* they are in the same universality class, and if we are only interested in universal features of the cow. It is vital to note that this is *not* an approximation of reality due to our limited computational ability, but an abstraction of the essence of reality because those features are the only determining factors for universal behavior. By doing this correctly, we are not making approximations and we can still obtain exact results, such as the scaling functions and the critical exponents. The use of the lattice model to predict the scaling functions and critical exponents of solid-liquid transition is one example, the use of simple cellular algorithms to study the critical dynamics in binary alloys[23; 24] and liquid crystals[25; 26] are others.

This is remarkable. Instead of writing down a faithful and detailed representation of a physical system, which is what scientists often try to do, we can now choose to study a simple model that shares the same essential features as the physical system. This is very powerful when we study systems that are complex, and results in the technique we call *minimal modeling*. Minimal models are models that only capture the essential features of the system. They are not faithful representations of the system, and in many cases, they may seem too simple to describe complicated phenomena. An example is when we study turbulent fluid flow, we can always proceed by solving the Navier-Stokes equation faithfully. But if we are not interested in the detailed velocity profile but in the overall pattern of the flow, we can model the water transport by a simple cellular model, which only captures the basic fact that water spreads in all direction, and that the flow is proportional to the square root of the local slope[27; 28].

It is important to notice that this approach does not work in every system. It only works in systems that exhibit universal features. If the system, or the quantity we are interested in, is sensitive to microscopic details, there is no way we can make a minimal model for it. If one is interested in the detailed velocity profile of a turbulent fluid, the only way to get that is to solve the Navier-Stokes equation faithfully.

The idea that we can model complex systems with minimal models is completely different from the traditional approach of reductionism. In a reductionist point of view, it is essential to take into account every interaction between every element of a complex system, in order to understand the system as a whole. This approach analyzes the system by first studying its components, and by understanding the components, hopefully the behavior of the whole can be understood. This is called the bottom-up approach. By doing minimal modeling, however, we are following the top-down approach. We analyze the system as a whole. Essential features are extracted and put into the models. In this method, the detailed interactions of the elements of the system are not captured, but the hope is to capture the universal features of the system.[29]

It is fair to say that both approaches are valuable, and that they are good for different problems. However, it is interesting to point out that while the reductionistic approach is traditional, intuitive and systematic, minimal modeling is new and exciting. There are, in some cases, artistic flavors in choosing what essential features to put in and how they should be implemented in the minimal models. Its development even attracts the attention of philosophers of science[30]. One of the open questions, and one which Nigel Goldenfeld's group is intensively studying, is the extent to which minimal modeling can be appropriate and useful in biology[31–33].

To conclude, we are interested in studying the scaling behavior in various systems because they are universal. This universality allows us to make simple, minimal models to describe complicated systems.

1.3 Backgrounds, Goals and Main Findings

As stated in the beginning of this chapter, three projects are presented in this dissertation and the overarching theme is the scaling behavior observed in each of the

systems. The goal of all the projects is to extract universal features of some complicated systems, by building minimal models, as necessary. The first project concerns the scaling behavior of disordered ferromagnets. The second project concerns pattern formation far from equilibrium in carbonate precipitating systems, where scaling behavior is also observed. The third project involves developing a minimal model that describes polycrystalline materials, both pure and alloyed. We also applied the model to study the scaling behavior of dislocation avalanches in the plastic regime.

1.3.1 Griffiths Ferromagnets

In previous sections, we mentioned that weak disorder and impurities do not change the universal features of a Ising ferromagnet, in the renormalization-group sense, *i.e.,* small amount of disorder and impurities are irrelevant to the ferromagnetic-paramagnetic transition. When the disorder is strong, however, the Harris criterion tells us that disorder and impurities are relevant. The aim of this project is to study the effect of such relevant disorder on the scaling behavior of ferromagnets.

The effect of disorder on ferromagnetic systems is highly non-trivial and poorly understood. In pure ferromagnetic systems, it is well known that the behavior is described by a single critical point $T = T_c$, separating the paramagnetic and ferromagnetic phases. One would suspect, then, that the only effect of disorder is a decreased value of T_c, because disorder reduces the probability of finding a percolating pathway throughout the entire system, and this interferes with the collective ferromagnetic behavior. Griffiths, however, showed that this is not the case. In the thermodynamic limit, and for $T_c < T < T_G$ (T_c and T_G are the critical temperatures for the disordered and the pure ferromagnets respectively), although the system is not a ferromagnet in the conventional sense, there can exist arbitrarily large volumes in the system that are devoid of disorder, with the probability being exponentially sensitive to the volume. As a result, the free energy is non-analytic in the external

field h across this temperature range; this is called the Griffiths phase[34].

The scaling behavior of Griffiths ferromagnets is still controversial, despite much theoretical and experimental effort. A scaling theory near the Griffiths-paramagnetic transition is lacking. Using the usual scaling form of ferromagnets, unrealistically large exponents are fitted[35]. However, we discovered the first clear experimental signature of a Griffiths phase in $La_{0.7}Ca_{0.3}MnO_3$[36]. We derived the thermodynamics of such systems from the distribution of grand partition function zeros: the so called Yang-Lee approach[37]. Using an argument due to Bray[38], we showed that the density of such zeros exhibits an essential singularity in the complex magnetic field plan, and derived the scaling function, the associated critical exponent and the asymptotic behaviors for $T \to T_c$; we also derived the non-analyticity of magnetization in h in the Griffiths phase. Our calculations gave an excellent account of the experimental data.

1.3.2 Geophysical Pattern Formation

Fig. 1.1 and Fig. 1.2 show respectively terraced landscapes and a circularly symmetric dome observed in Angel Terrace, Mammoth Hot Springs, WY. Hot carbonate-charged spring water comes out of the vent, flows over the pre-existing terrain, releases CO_2 and precipitates $CaCO_3$ in the form of travertine. The surface, as a result, grows and changes the flow path of the spring water, which in turn changes how $CaCO_3$ is precipitated. This dynamic interplay between spring water flow, precipitation and surface growth gives rise to the beautiful patterns showed in the figures.

Both the complexity of the terraces and the regularity of the domes draw us to model the precipitation process and to understand how these structures can be formed in a highly fluctuating environment. We used two approaches to model this process. First, we modeled this process by solving the Navier-Stokes equation, the surface growth kinematics and an empirical formula describing the precipitation rate. In the

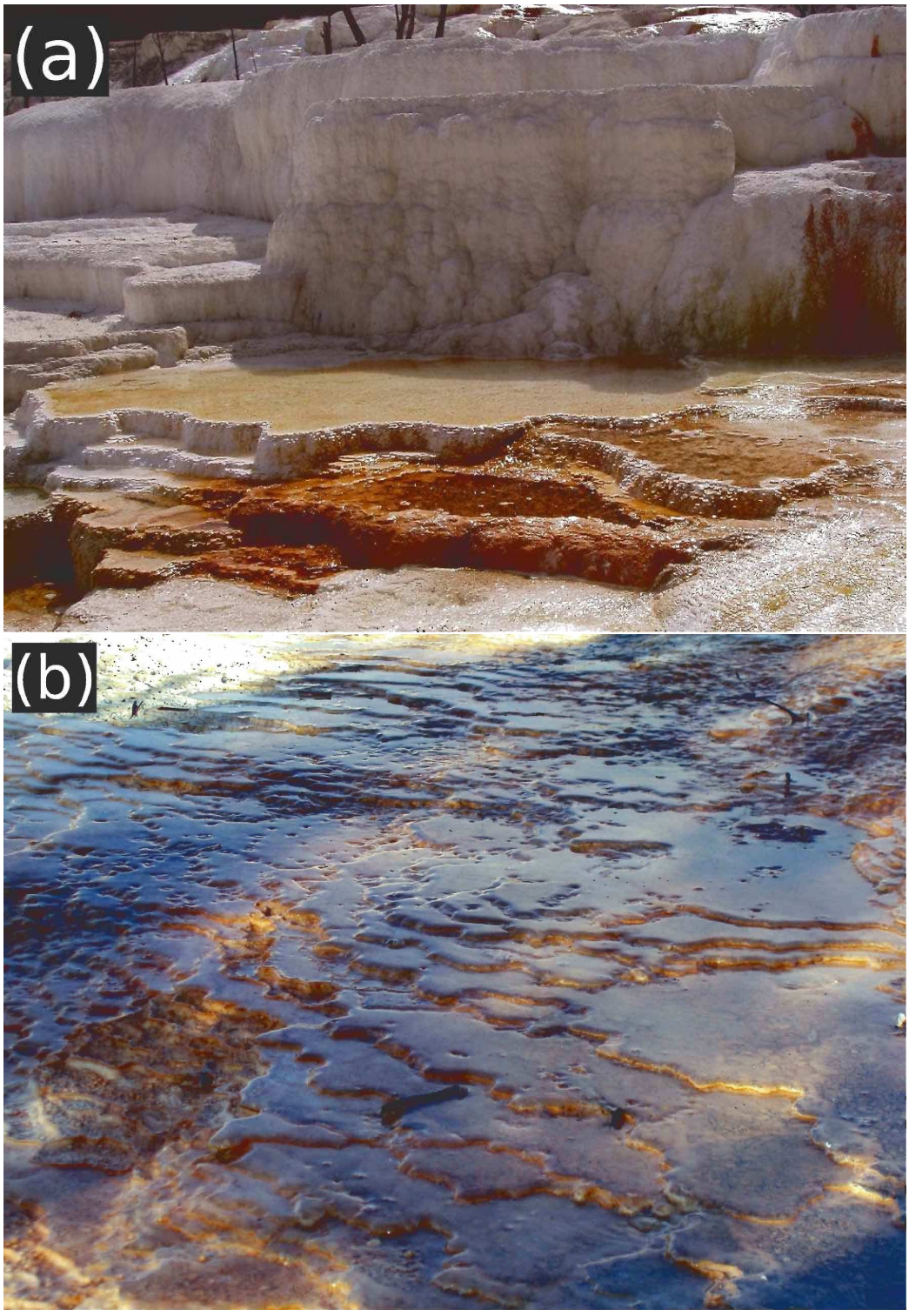

Figure 1.1: (Color online) Travertine formation at Angel Terrace, Mammoth Hot Springs, WY. (a) a large pond, of order 1 meter in diameter, and smaller features. (b) a portion of the flow system about 25 meters from the vent, on the scale of centimeters.

Figure 1.2: A spherically symmetric dome observed in Angel Terrace, Mammoth Hot Springs, WY.

language of the previous sections, this is the reductionist or bottom-up approach to the problem, where details of the fluid flow and precipitation dynamics are described by partial differential equations. In fact, there are three coupled nonlinear partial differential equations, which are in general difficult to analyze. We showed that, however, in cases of spherically symmetric domes, where the geometry is simple, analytical solutions that describe the dome shapes can be obtained. We obtained such a solution and compared it with field observations. The solution fits well to the observation except near the bottom of the dome, where a fluting pattern is observed. We showed that this departure from the theory is due to the absence of surface tension in our model, which has a more and more important influence as the fluid flows down the dome and thins out. Ultimately contact lines form, and the water trickles down as rivulets. Although our theory does not take surface tension into account, it predicts the onset of contact line formation and we were able to make a scaling theory about this departure point. This behavior was verified by John Veysey and Nigel Goldenfeld[28] using a cell dynamical system (CDS) model, which is our second modeling approach.

The CDS model is a minimal model for fluid flow and precipitation dynamics. It complements the first method in two ways. First, the CDS model verifies that the departure from the analytical theory in the fluting region is indeed due to the lack of surface tension in the description. By switching the surface tension on and off, the CDS model reproduces the field observations and the theoretical prediction respectively. This, by the way, verifies that the minimal model is modeling the same physics as the partial differential equations. Second, the CDS model provides a platform to study the fully nonlinear, non-equilibrium aspects of the problem. It is shown that this CDS model is capable of predicting the statistical properties of the striking terraced landscapes observed in the field.[28]

We also calculated the stability of various solutions. We found that the dome so-

lution is not stable; in fact, there are infinitely many unstable modes. We argued that this instability is, again, due to the absence of surface tension in our analysis. We also calculated the stability of stalactites, which are formed by a very similar geophysical process. We found that, on the contrary, stalactites are stable to perturbations of all scales. We proposed that the difference of stability between the two structures is due to the way fluid is transported along the growth forms.

Although our analytical theory cannot describe the terraced landscape, by calculating the stability spectrum of a turbulent flow over a constant slope and showing that such a flow is unstable for perturbation of all scales, we showed that a seemingly scale-free structure is consistent with our theory. Our field data and the work of John Veysey and Nigel Goldenfeld[28] document this scale invariance and other statistical aspects of hot spring landscapes.

1.3.3 Multiscale Modeling of Materials using the Phase Field Crystal Model

Elasticity, plasticity and fracture are common features of real materials. Although of fundamental and tremendous industrial significance, a complete understanding of these phenomena is still elusive, even after more than a century of intensive research by scientists and engineers. The main obstacle is that a full solution requires understanding of the dynamics on both mesoscopic and microscopic scales rather than merely on macroscopic scales. Plasticity, for example, is caused by interactions between different crystal defects under external forces. These defects, such as grain boundaries and dislocations, are mesoscopic objects. As a result, understanding and manipulating the plastic properties of materials require modeling the system across many scales, *i.e.,* from nanometers up to millimeters. What makes the situation worse is that most of these phenomena occur on diffusive, rather than atomic vibrational, time scales. This poses a challenge, because none of the traditional tools of

material science, including continuum models, Monte Carlo methods[39; 40], molecular dynamics simulations[41; 42] and density functional methods[43–46], can address such a broad spectrum of scales. As a result, there has been substantial interest in developing multiscale computational methods recently[47–49].

A number of multiscale modeling techniques, including quasi-continuum methods[50–53], the heterogeneous multiscale method[54; 55] and multiscale molecular dynamics[56–59], have been proposed. Although they serve as unified descriptions of phenomena on multiple scales, some of them involve non-systematic ways of bridging descriptions of different scales, potentially introducing artificial excitations and interactions into the systems.

We attempted to tackle this multiscale problem by using the recently proposed phase field crystal (PFC) model[60; 61]. The PFC model is a minimal density functional theory that respects rotational and translational symmetries of the crystal and captures elasticity and crystallography of the materials. Depending on the reduced temperature and the mean density, liquid, stripe or crystalline phases can be obtained. With diffusive and conservative relaxation dynamics, the model describes the evolution of atomic density on diffusive time scales. The model is shown to be capable of describing processes such as polycrystalline solidification, crack formation, dislocation glide and climb, grain boundary dynamics and epitaxial growth. Recent applications of renormalization group techniques and adaptive mesh refinement[12; 13; 62], moreover, allow a grid size much larger than the atomic spacing, which reduces the computational time by orders of magnitude. Using these methods, the dynamics of a two dimensional sample of millimeter scales over diffusive time scales (sec), with spatial atomic resolution, can be computed within several days on a single processor desktop machine.

We further developed and applied the PFC model to study several multiscale phenomena in materials. We showed that the free energy in the PFC model can be

rewritten merely in terms of complex amplitudes—the spatially varying envelope of the order parameter. The Renormalization Group equations, or the complex amplitude equations, can then be written down as conservative and relaxational dynamics of the free energy, similar to the original dynamical equation in the model. From this complex amplitude representation, we analytically derived a theory of nonlinear elasticity. This shows that the PFC model contains the correct form of nonlinear elasticity. We also studied the plastic properties of the PFC model. By shearing a PFC crystal, we observed creation, annihilation and interactions of dislocations. Depending on the shearing rate, these dislocations interact with each other and form avalanches of all sizes, manifested in a noise spectrum, which resembles the crackling noise in driven ferromagnetic systems[17; 63–65]. The statistics of such avalanches follows a power law and is quantitatively similar to the dislocation avalanches in other systems[66; 67]. These results show that while the PFC model describes solidification and individual dislocation interactions on microscopic scales, it also captures the correct nonlinear elastic and even plastic properties of real materials. The PFC model puts different scales on equal footing and serves as an excellent framework for studying multiscale phenomena in materials.

Although the PFC model contains the crystallographic, elastic and plastic properties of a crystal, one of its shortcomings is that it actually does not convey information about the actual atomic configurations. The notion of 'atoms' is ill-defined in the PFC framework because the order parameter can form many peaks ('atoms') as long as that helps reducing the total energy of the system. Moreover, the order parameter is a continuous field that can extend to negative—it is not a physical density. Vacancies, as a result, are not stable in the PFC model. Any vacancies created would soon be filled up by the surrounding field. This makes the model inappropriate for studying phenomena that involve vacancy diffusion. In Chapter 7, however, we show that we can modify the PFC model to accommodate the actual atomic configurations by for-

bidding the order parameter to take on negative values. By doing so, we promote the order parameter from an abstract continuous field to a physical density that directly dictates the atomic configuration. In this modified PFC model, we can control the number of atoms, the interaction between the atoms and the temperature. By lowering the mean density, we succeeded in simulating a liquid using the PFC model and reproducing the standard two-point correlation function of a liquid. This modified PFC model, in essence, is a molecular dynamics simulation. The only difference is that we are solving a partial differential equation instead.

Finally, by putting together two PFC models and adding an interaction term between the two order parameters, we extended the PFC model to binary systems. We showed that the resulting model of binary alloy describes diffusion on multiple scales. On atomic scales, we observed individual atomic hopping events; on macroscopic scales, the model reproduced diffusion profiles that agree with the standard diffusion equation. By varying the temperature in the system, we also recovered the activated Arrhenius form of the diffusion coefficient, $D(T) = D(0)e^{-E_{act}/k_BT}$.

To conclude, we modified the PFC model to accommodate vacancy structures and extended the model to binary systems. We also applied the PFC model to study multiscale phenomena in materials, ranging from nonlinear elasticity and plasticity in pure systems, to atomic hopping and diffusion in binary alloys.

1.4 Dissertation Outline

This dissertation is organized as follows. In chapter 2, we discuss the novel scaling behavior of Griffiths ferromagnets and compare our theory with experimental data. We then discuss the mathematical formulation we used to describe geophysical precipitation pattern formation in chapter 3. This formulation is applied to the formation and stability of domes and stalactites, as well as the damming instability that gives

rise to scale-free terraced landscapes. Chapter 4 is an introduction to the phase field crystal (PFC) model, in which detailed discussions of the rationale behind the model and some recent developments can be found. We derive the nonlinear elastic property of the complex amplitude representation of the PFC model in chapter 5. Numerical studies of the model's plastic properties and analysis of the avalanches statistics are presented in chapter 6. In chapter 7, we modify the PFC model to accommodate the actual atomic configurations and vacancies. We also derive the condition under which vacancies are present. The PFC model is extended to binary systems in chapter 8, in which we also show that the model describes both microscopic atomic hopping and macroscopic diffusion. We conclude in Chapter 9.

1.5 My Role in Interdisciplinary Collaborations

Most of the projects I worked on involved close collaborations with researchers from multiple disciplines. In the Yellowstone project, I worked closely with Prof. Bruce Fouke and Dr. Michael Kandianis from the Department of Geology, as well as Dr. John Veysey from the Department of Physics. I have contributed to field trip preparation work (Pitot tube building and calibration, as well as sample preparation) and post-trip data processing—most notably the extraction of terraces shapes from graphical data sets. I have also helped in comparing and benchmarking the minimal model on precipitation developed by Dr. Veysey with the analytical framework. More importantly, I have built the mathematical framework that describes geophysical precipitation pattern formation and derived the shapes and stabilities of domes and stalactites, as well as the damming instability. I have also compared the theoretical predictions with field observations.

On the multiscale modeling project, I have been working closely with Prof. Jonathan Dantzig, Dr. Badrinarayan Athreya and Mr. Zhi Huang from the Department of Me-

chanical Engineering, as well as Prof. Karin Dahmen and Mr. Georgios Tsekenis from the Department of Physics. I was responsible for developing the nonlinear elasticity theory from the PFC model, simulating the dislocation avalanches under plastic deformation and analyzing the resulting statistics. I also modified the PFC model to accommodate vacancies, extended the model to binary systems and simulated the diffusion process in binary systems.

I worked with Dr. Myron Salamon, who was Professor of Physics and associate Dean of the College of Engineering in the University of Illinois at Urbana-Champaign then and now is the Dean of natural sciences and mathematics at the University of Texas at Dallas. I contributed to relating the scaling behavior of magnetization and that of the Yang-Lee zero density, as well as deriving the asymptotic behaviors of the magnetization, heat capacity and zero-field susceptibility of Griffiths ferromagnets from Bray's ansatz for the Yang-Lee zero density. I was also responsible for comparing the theory with experimental data provided by Dr. Salamon and extracting from it the universal scaling functions and critical exponents.

1.6 Publications

Parts of this dissertation have already been published. Chapter 2 and part of chapter 3 have appeared in *Physical Review Letters* as two separate articles[36; 68]. The rest of chapter 3 is submitted to *Physical Review E* and has been accepted for publication[69]. Chapters 5 and 7 will soon be submitted to *Physical Review Letters* separately. We also anticipate submitting chapters 6 and 8 to *Physical Review E*.

Chapter 2

Griffiths Singularity

2.1 Introduction

The influence of disorder on ferromagnets remains, after more than 30 years of effort, a complex and poorly-understood phenomenon. In its simplest form, disorder can be represented as a random spatial variation of the exchange interaction J in the bonds between neighbouring sites on a regular lattice. If a great enough fraction $p > p_c$ of the bonds have $J = 0$, then one would expect that there is a vanishingly small probability of finding a percolating pathway of bonds throughout the system, and the cooperative ferromagnetic phase would cease to exist. For smaller values of p, we would expect that the ferromagnetic phase will exist in a form weakened by the shortage of percolating paths; hence thermal fluctuations will destroy the ferromagnetic phase at a temperature T_c which is *lower* than the critical temperature T_G of the pure ferromagnet. However, as Griffiths showed[34] it is not the case that the phase for $T_c < T < T_G$ is purely paramagnetic, because in the thermodynamic limit, there can exist arbitrarily large volumes of the system that are devoid of disorder, with a probability exponentially sensitive to the volume. As a result, the free energy is non-analytic in external field, h, throughout the whole Griffiths phase. The effect of disorder is to partition the pure system into small ferromagnetic clusters. Depending

on the size, each cluster has a different value of T_c, so that the system as a whole exhibits a spectrum of T_c, spanning from the critical temperature of the pure system, T_G, due to arbitrarily large clusters, to some value of T_c, contributed by smaller clusters.

Here we are concerned with the phase transition between the ferromagnetic and Griffith's phases. Just as in the case of a pure ferromagnet, one would like to predict the critical phenomena, but the non-analytic nature of the Griffith's phase makes it difficult to apply off-the-shelf renormalization group techniques[70–72] or to posit simple scaling laws, despite recent theoretical progress[38; 73–77]. Indeed, it is currently controversial whether or not there is clear experimental evidence[78–81] supporting the existence of the Griffiths phase. From the practical perspective, perhaps the most unsatisfactory aspect of efforts to relate theory to experiment is that critical exponents derived from conventional scaling laws are unrealistically large: for example, the critical isotherm exponent was recently[35] estimated as $\delta = 17$. The breakdown of conventional scaling strongly suggests that the functional form of the scaling relations actually reflects the essential singularities intrinsic to the Griffiths phase, and that some form of exponential scaling, rather than algebraic scaling, is appropriate.

The purpose of this chapter is to address these problems by exploring the expected form of scaling relations that would follow from a leading essential singularity contribution to the statistical mechanics in the Griffiths phase. Such a contribution can be conveniently represented using the Yang-Lee theory of phase transitions[37] to derive the scaling behavior in the Griffiths phase from a simple, physically-motivated ansatz for the distribution of partition function zeros, following arguments originally due to Bray and Huifang[38] for the case of long-ranged ferromagnets. We demonstrate that the leading singularities in the thermodynamics can be deduced, and that our predictions consistently describe high quality magnetic and thermodynamic data[35; 78] on the disordered Heisenberg ferromagnet $La_{0.7}Ca_{0.3}MnO_3$. We emphasize that our

purpose is only to identify the leading essential singularities, and that it is beyond the scope of our work to provide a full description valid outside of the asymptotic critical regime. Nevertheless, the experimental data have sufficient resolution that we have strong support for our scaling predictions in this asymptotic regime.

Magnetic properties are well-accounted for by our approach, but heat capacity data are not expected to follow a simple scaling form–and indeed do not–due to the complex form of the theoretical predictions which arise from even the simplest Yang-Lee zero distribution function that we use. The non-analyticity of magnetization in external field - a signature of the Griffiths phase - is also explicitly demonstrated. Our results provide strong evidence for a Griffiths singularity, and highlight the need for a more systematic renormalization group approach to understanding the singularities in such disordered systems.

2.2 Yang-Lee Zeroes and Critical Phenomena

In 1952, Lee and Yang[37] developed a theory of phase transitions based upon the density g of zeroes of the grand partition function as a function of the complex fugacity and showed that the zeroes lie on a unit circle in the complex plane, parameterized below in terms of the angle θ. The distribution $g(\theta)$ varies with temperature T and dictates the functional form of thermodynamics. Near a critical point, it is expected that $g(\theta, T)$ exhibits behavior which reflects the non-analyticity of the thermodynamics[82; 83], and we provide this connection explicitly here, for both the case of conventional ferromagnetic critical point scaling, and then for the scaling near the Griffiths point.

We begin with the scaling of the magnetization per spin, $M(H, t)$, where H is the external magnetic field and $t \equiv (T - Tc)/Tc$ is the reduced temperature, for a regular Ising ferromagnet. The exact relationship between $M(H, t)$ and $g(\theta, t)$ can be written

as[37]

$$M(H,t) = 2\mu \int_0^\pi d\theta \, \frac{g(\theta,t)\tanh(\mu H/k_BT)[1+\cot^2(\theta/2)]}{1+(\tanh(\mu H/k_BT)\cot(\theta/2))^2}, \tag{2.1}$$

where μ is the magnetic moment of individual spins. To extract the scaling behavior, we proceed by expanding around the critical point $H = 0$ and $t = 0$. Because the singular behavior arises from the limit $\theta \to 0$, we also expand the integrand about $\theta = 0$, resulting in

$$M(H,t) = 2\mu \frac{\mu H}{k_BT} \int_0^\pi d\theta \frac{g(\theta,t)}{(\mu H/k_BT)^2 + \theta^2/4}, \tag{2.2}$$

which is valid near the critical point, up to corrections reflecting a smooth background. A change of variables, $\theta = \mu H\phi/k_BT$, gives

$$M(H,t) = 4\mu \int_0^{\pi k_BT/2\mu H} d\phi \frac{g(2\mu H\phi/k_BT,t)}{1+\phi^2} \tag{2.3}$$

where the upper limit is replaced by ∞ as $H \to 0$. This is the primary relation between $M(H,t)$ and $g(\theta,t)$ near the critical point. The scaling form of the magnetization,

$$M(H,t) = |t|^\beta f_M(H/|t|^{\beta\delta}), \tag{2.4}$$

where $f_M(x)$ is an unknown scaling function, and β and δ are two critical exponents, implies a scaling form for $g(\theta,t)$. Substituting Eqn. (2.4) into Eqn. (2.3), Mellin transforming the expression and using the corresponding convolution relation, we arrive at the scaling form of $g(\theta,t)$ as $\theta \to 0$

$$g(\theta,t) = |t|^\beta G(\theta/|t|^{\beta\delta}), \tag{2.5}$$

where $G(x)$ is a scaling function for $g(\theta,t)$.

Apart from exhibiting the scaling form of $g(\theta,t)$ for normal ferromagnets, this exercise also shows that knowledge of $g(\theta,t)$ can be gained by studying the scaling form of $M(H,t)$, and vice versa. In the following section, we study the scaling behavior of $M(H,t)$ in the Griffiths phase using a heuristically-derived form for $g(\theta)$. We will see that the result is different from that of the pure case, reflecting the intrinsic essential singularity that characterizes Griffiths phases.

2.3 Density of Zeros for a Disordered Ferromagnet

We start with the scaling form of $g(\theta, t)$ derived on the basis of heuristic arguments by Bray and Huifang[38] for disordered ferromagnets with short-ranged interactions:

$$g(\theta, t) = \frac{1}{\pi} \Re \sum_{r=1}^{\infty} \exp(-A(t)r) \tanh\left[r(i\theta + \epsilon)\right] \tag{2.6}$$

where $\epsilon \to 0^+$ and $A(T) \sim (T - T_c)^{2-\beta_r}$ as $T \to T_c$ and $A(T) \to \infty$ as $T \to T_G$. The exponent β_r is the order parameter exponent for the random case, and its value will reflect the universality class of the magnet, be it Ising, Heisenberg, O(n) etc. In the limit that $\theta \to 0$ and $A \to 0$, the summand is dominated by peaks at values of $r = (2n+1)\pi/2\theta$ for all non-negative values of n, whose height is given by $(2\theta/\epsilon(2n+1)\pi) \exp(-(2n+1)\pi A/2\theta)$. The width of these peaks therefore scales in the same way as their separation, both being proportional to $1/\theta$. Thus, the expression takes the form:

$$g(\theta, t) = g_0 \exp(-A(t)/|\theta|), \tag{2.7}$$

where g_0 is a constant. The essential singularity in Eqn. (2.7) reflects the Griffiths phase of disordered ferromagnets, not present in the pure case. Disordered magnets with long-range interactions have a power-law prefactor to the essential singularity [38], but this is not present in the short-range case. A disordered ferromagnet can be thought of as an ensemble of weakly interacting, finite-sized ferromagnetic clusters. When $T \sim T_G^-$, only large clusters contribute to the overall magnetization. For each large cluster of linear size L, the smallest Yang-Lee zero is of the order of $\theta \sim 1/mL^d$, where $m \sim (T_G - T)^\beta$ is the magnetization per spin of the cluster and d is the spatial dimension of the system. The probability of a spin belonging to a cluster of size L follows the Poisson distribution, *i.e.,* prob $\sim \exp(-cL^d)$. As a result, large clusters contribute to $g(\theta, t)$ in the form of Eqn. (2.7), where $A(t) \sim (T_G - T)^{-\beta}$ and β is the usual exponent for pure ferromagnets.

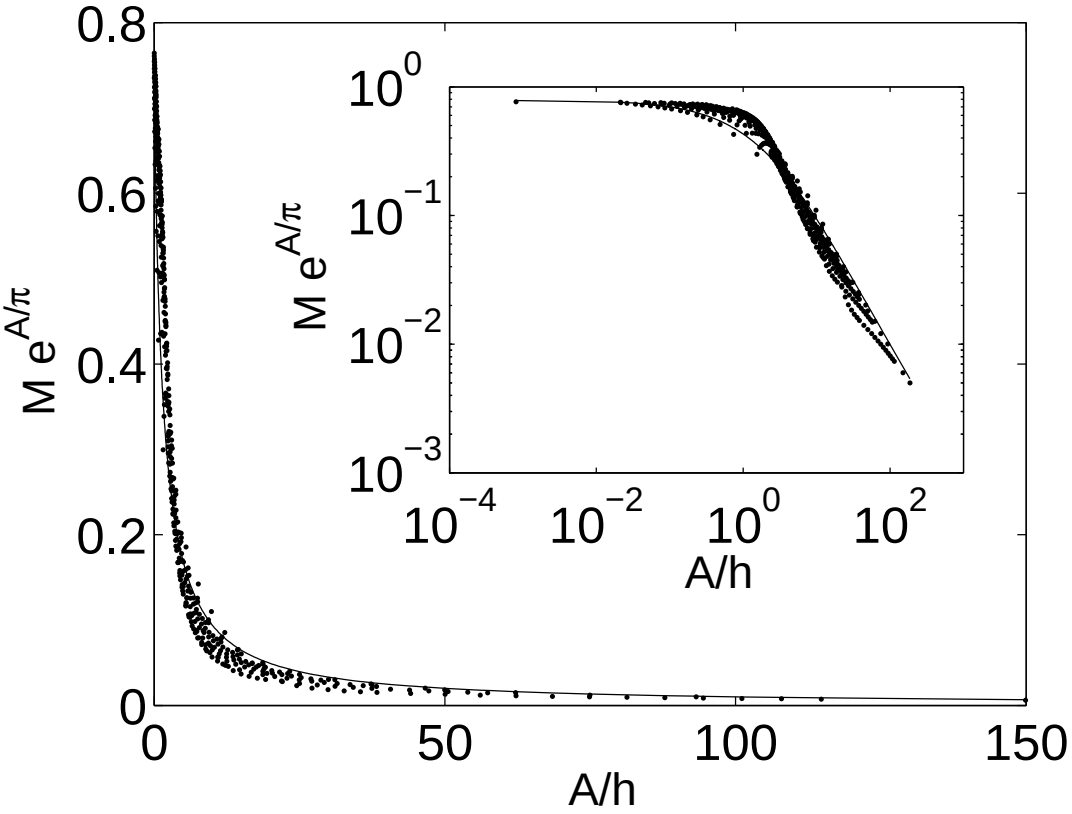

Figure 2.1: Data collapse of magnetization, $M(h,t)$. Dots are experimental data and the line is the theoretical prediction for the universal scaling function, with $g_0 = 0.5$, $A_0 = 0.5$ and $\beta_r = 0.8$. Data shown are in the range of $t < 0.35$ and $h \equiv \mu H/k_B T_c < 0.39$. The insert shows the data on logarithmic scales.

For $T < T_c$, the system is in its ferromagnetic phase with nonzero magnetization, implying a nonzero value of $g(\theta = 0, t)$[37]. This requires $A(t) = 0$ at $T = T_c$ to counteract the essential singularity at $\theta = 0$. For $T \sim T_c^+$, we can expand $A(t)$ and approximate it by $A(t) \sim t^{2-\beta_r}$. This accounts for the asymptotic behavior of $A(t)$.

With this form of $g(\theta, t)$, the scaling behavior of $M(h, t)$ can be obtained by substituting Eqn. (2.7) into Eqn. (2.2) and making a change of variables, $y = A(t)/\theta$, yielding

$$\frac{M(h,t)}{\mu} = \frac{g_0 A(t)}{2h} \int_{A(t)/\pi}^{\infty} dy \frac{\exp(-y)}{y^2 + (A(t)/2h)^2}, \tag{2.8}$$

where we defined $h \equiv \mu H / k_B T_c$. Eqn. (2.8) can be written in terms of the exponential integral, $E_1(x) \equiv \int_x^\infty e^{-t}/t \, dt$, as

$$\frac{M(h,t)}{\mu} = -g_0 \Im[\exp(iA(t)/2h) E_1(A(t)/\pi + iA(t)/2h)]. \tag{2.9}$$

We expand Eqn. (2.9) about $A = 0$, because $A(t) = A_0 t^{2-\beta_r}$ is asymptotically small in the critical region, resulting in

$$\frac{M(h,t)}{\mu} = -g_0 e^{-A(t)/\pi} \times \Im[e^{iA(t)/2h} E_1(iA(t)/2h)]. \tag{2.10}$$

This implies an approximate scaling form

$$\frac{M(h,t)}{\mu} = \exp(-A(t)/\pi) \left[f_M(A(t)/h) + O(h) \right], \tag{2.11}$$

where

$$f_M(x) = -g_0 \Im[\exp(ix/2) E_1(ix/2)], \tag{2.12}$$

and the corrections of $O(h)$ involve exponential integrals of A/h. This scaling prediction is valid in the limits $A \to 0$, $h \to 0$, but the ratio A/h has not been fixed by the analysis so far.

2.4 Analysis of Magnetization Data

We now analyze the experimental data on $La_{0.7}Ca_{0.3}MnO_3$ [35; 78], using the above results, to see if the data are consistent with the presence of a Griffiths phase. Fig.

(2.1) shows the predicted data collapse of the magnetization with fitted values $T_c = 218K$, $g_0 = 0.5 \pm 0.05$, $A_0 = 0.5 \pm 0.05$ and $\beta_r = 0.8 \pm 0.05$. The error bars were obtained by estimating the best fit visually. The figure also shows the agreement between the theoretically-predicted universal scaling function and the collapsed data. Overall, the data scale quite well, and the scaling function of the collapsed data are close to that of the theory, except near the turning point of the curve, where corrections to the leading order ansatz we have used for Eqn. (2.11) become important, and the data are no longer in the asymptotic limits $A \to 0$ and $h \to 0$. In order to show this clearly, we calculate the asymptotics of the scaling function, in the limits $A/h \to 0$ and $A/h \to \infty$, where the leading terms in the magnetization can be calculated systematically.

2.5 Asymptotic Behavior

From Eqn. (2.9), the asymptotic behavior of $M(h,t)$, in the limit $A/h \to \infty$, is given by

$$\frac{M(h,t)}{\mu g_0} \to \frac{2h}{A} e^{-A/\pi} \left[1 - \frac{4h^2}{\pi^2} - \frac{8h^2}{\pi A} + O\left(\frac{h^2}{A^2}\right) \right]. \tag{2.13}$$

showing that the small field susceptibility, M/h, in the limit $A/h \to \infty$, depends linearly on $\exp(-A/\pi)/A$. This prediction recovers Curie-Weiss-like behavior, as verified by the experimental data shown in Fig. (2.2). The experimental data shows a slope of 0.93, consistent with the fitted range of values for $0.9 < 2g_0 < 1.1$.

A profound difference between conventional and Griffiths ferromagnets is found in the limit $A/h \to 0$. It is well understood, for conventional ferromagnets, that $M(h,t) \sim h^{1/\delta} \to 0$ as $h \to 0$; this is, however, not true in Griffiths ferromagnets, as we can see by calculating the asymptotic behavior of $M(h,t)$:

$$\frac{M(h,t)}{\mu g_0} \sim \frac{\pi}{2} + \left(\ln\left(\frac{A}{2h}\right) + \gamma - 1 \right) \frac{A}{2h} - \frac{2h}{\pi} + \frac{Ah}{\pi^2} + O\left(\frac{A^2}{h^2}\right) \tag{2.14}$$

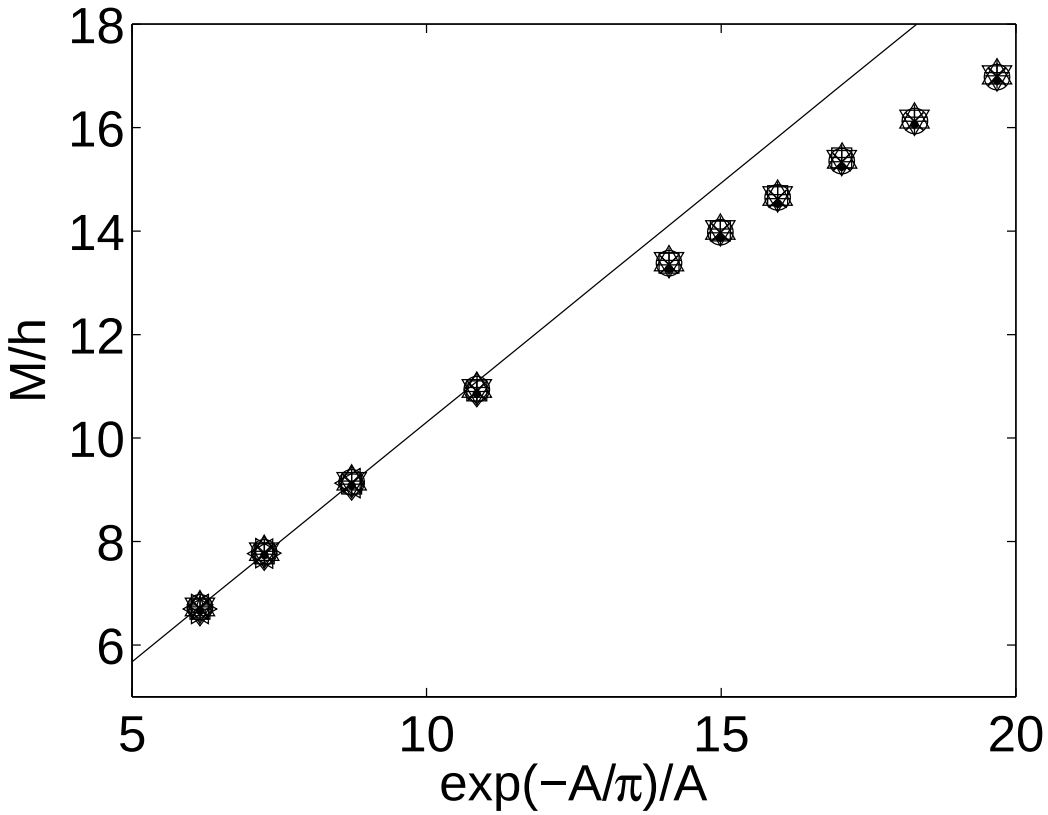

Figure 2.2: Experimental verification of the asymptotic behavior of the magnetization for $A/h \to \infty$. The data show a linear dependence of M/h on $\exp(-A/\pi)/A$ with slope 0.93 as predicted by Eqn. (2.13). The range of values of A plotted is $0.05 < A < 0.155$. Legend: $\cdot$ $h = 0.0006$, $\times$ $h = 0.0011$, $\circ$ $h = 0.0017$, $\triangle$ $h = 0.0023$, $\bigtriangledown$ $h = 0.0028$, $+$ $h = 0.0034$, $*$ $h = 0.0045$, $\square$ $h = 0.0057$, $\diamond$ $h = 0.0072$, $\triangleleft$ $h = 0.0090$, $\triangleright$ $h = 0.0122$, $\star$ $h = 0.0141$ and the solid line shows the linear prediction of Eqn. (2.13).

as $A/h \to 0$, where $\gamma \sim 0.57722\ldots$ is the Euler-Mascheroni constant. This implies that $M(h,t) \to \mu g_0 \pi/2$ as h, $A/h \to 0$, *i.e.*, a discontinuity of $M(h,t)$ at $h = 0$ on the critical isotherm. Experimental support for this surprising result is present in Fig. 3 of Ref. ([35]), which documents the increase of the exponent δ fitted to data assuming the conventional scaling applies. As the transition temperature is lowered by increasing disorder, the inferred value of δ rises to as much as 16.9, inconsistent with any known universality class, but indicative of a very rapid and dramatic rise in magnetization. In order to test the precise predictions made here, we show in Fig. (2.3) the experimental verification of Eqn. (2.14), where the function $M/\mu g_0 + 2h/\pi - Ah/\pi^2$ is plotted against $A/2h$. The data points satisfying the criteria $h < 0.0072$ and $A/h < 0.3$ are shown in Fig. (2.3). All the parameters were determined previously according to the data collapse in Fig. (2.1), so that we have not made any additional fitting. The experimental data approach the theoretical curve as $A/h \to 0$, and moreover tend to the universal number $\pi/2$ as dictated by Eqn. (2.14). We conclude that the data are consistent with the prediction that $M(h,t)$ is discontinuous at $h = 0$ in the limit $A/h \ll 1$, a prediction which follows from the essential singularity characterizing the Griffiths transition[34].

2.6 Heat Capacity

We conclude with a brief discussion of the heat capacity, $C(h,t)$. We can integrate Eqn. (2.11) to obtain the free energy, $F(h,t)$ and thence an expression for $C(h,t)$. There is no prediction of data collapse, due to the interference from the exponential terms, in agreement with our failure to obtain data collapse from the data. This form contains singular terms of the form

$$\int d\theta\, e^{-A/\theta} \ln(4h^2 + \theta^2) \sim \exp(-A/h) \tag{2.15}$$

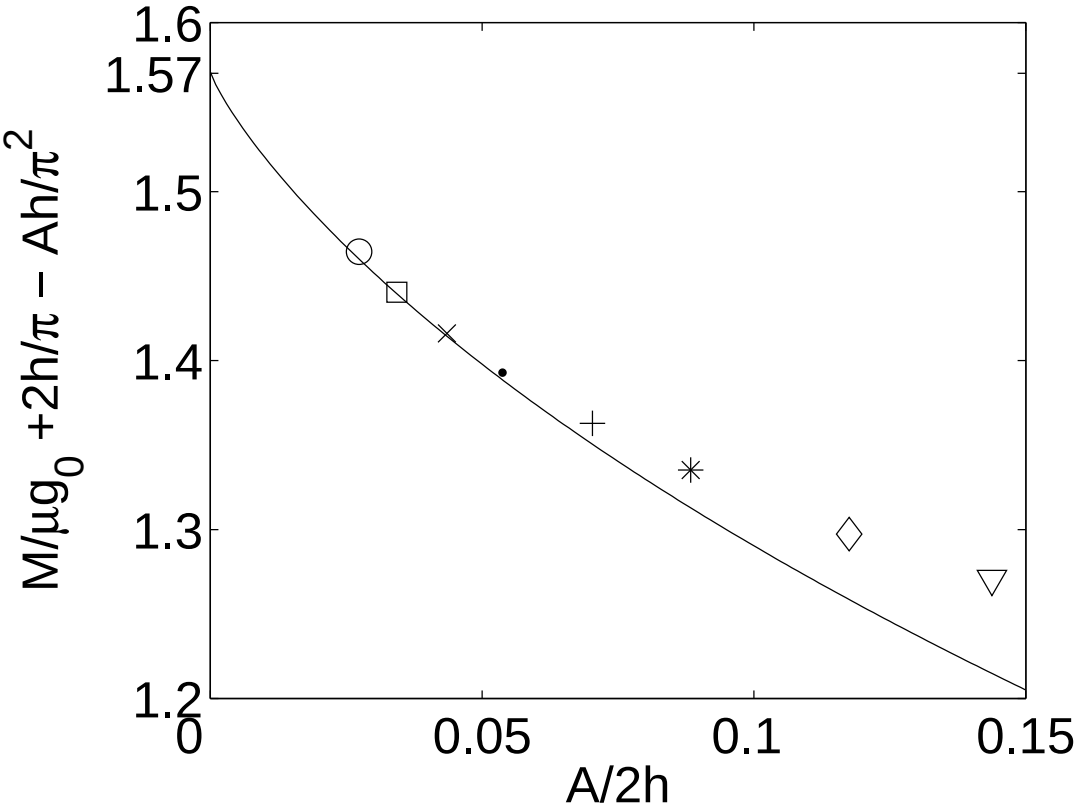

Figure 2.3: Asymptotic behavior of the magnetization for $A/h \to 0$, showing that the data follow Eq. (2.14), and exhibit a discontinuity $M \to \mu g_0 \pi/2$ in the limit $h \to 0$. The data shown here are within the limit $A/h < 0.3$ and $h < 0.0072$. Legend: $\bigtriangledown$ $h = 0.0028$, $\diamond$ $h = 0.0034$, $*$ $h = 0.0045$, $+$ $h = 0.0057$, $\cdot$ $h = 0.0072$, $\times$ $h = 0.0090$, $\square$ $h = 0.0112$, $\circ$ $h = 0.0141$. Solid line: theoretical prediction of Eq. (2.14).

where the integral is restricted to the neighborhood of the origin where Eqn. (2.7) is valid and the upper limit is assumed to scale with h, leading to the estimate of the essential singularity. Similar terms have also been predicted in Ref. ([77]), but more than the leading term must be retained in order to consistently compute the magnetization.

In conclusion, we have argued that the essential singularity of the Griffiths phase leads to novel features in the critical behavior, including a discontinuity of magnetization in external field. These features are reproduced to the accuracy expected from our lowest order theoretical predictions by high quality experimental data from $La_{0.7}Ca_{0.3}MnO_3$, and lead to a consistent description of its critical behavior, supporting the identification of this material as a Griffiths ferromagnet.

2.7 Conclusion

By using Bray's ansatz for the Yang-Lee zero density for short-ranged disordered ferromagnets, we derived the scaling behavior of Griffiths ferromagnets near the Griffiths-paramagnetic transition point. We also derived the asymptotic behavior of the magnetization and found excellent agreement between our theory and high quailty experimental data on disordered Heisenberg ferromagnet $La_{0.7}Ca_{0.3}MnO_3$, from which we also extracted the critical exponent. This is the first clear direct experimental evidence supporting the existence of the Griffiths phase.

Although we succeeded in deriving the scaling behavior of Griffiths ferromagnets, a systematic Renormalization Group approach to the scaling problem is still lacking, due to the essential singularity in the external magnetic field. We anticipate such an approach, together with a more rigorous derivation of the Bray's ansatz, in the future.

Chapter 3

Geophysical Precipitation Pattern Formation

3.1 Introduction

Geophysical pattern formation concerns how geological patterns and landscapes are formed as a result of the underlying physical and chemical dynamics. The aim is to predict the static, dynamical and statistical properties of the variety of geological structures formed. Recently studied examples include travertine motifs, namely dams[84], domes[68] and terraces[68; 85–87], stalactites[88; 89], as well as that of other patterns such as sand dunes[90; 91], black smoker chimneys at hydrothermal vents[92], columnar joints[93] and braided river networks[94].

This chapter focuses on the formation of travertine structures near geothermal hot springs. In such systems, hot spring water emerges from a vent, and deposits calcium carbonate as a mineral generally termed travertine as it degasses carbon dioxide[68; 84–86]. The formation of stalactites in limestone caves, which are also caused by carbonate precipitation, will also be briefly discussed.

The majority of the work done on the subject has focused on the microscopic aspects of the problem, such as the role of biomineralization due to thermophilic

Figure 3.1: (Color online) Travertine formation at Angel Terrace, Mammoth Hot Springs, WY, showing a large pond, of order 1 meter in diameter, and smaller features.

microbes[85; 86], the CO_2 degassing mechanisms[95; 96], mineral compositions[97; 98] and crystal structure[99; 100]. Here we are interested in the formation of macroscopic structures and motifs, such as domes, stalactites, and terraces[68], which are universal, *i.e.*, independent of microscopic details. In addition, we are interested in the resulting patterns and their correlations, rather than absolute rates of growth; accordingly, microscopic mechanisms that contribute to kinetics, including nucleation processes and potential biomineralization effects, are present in our work through the choice of time scale. There are no extra terms in the equations of motion whose presence can be attributed specially to any one of these microscopic processes.

There are two principal mathematical difficulties encountered in studying these macroscopic structures. First, the problem is highly nonlinear. As the carbonate is precipitated onto the surface, the surface evolves, which then changes the flow path of the fluid, thus affecting how precipitation takes place. This interplay between fluid flow and surface growth leads to a moving-boundary problem, which is mathematically difficult to solve. Second, the problem involves a variety of depositional processes, including solute advection, a complex sequence of chemical reactions, CO_2 degassing, as well as mass transfer between a solid and a liquid. Given that each of these processes is complicated and non-trivial to model on its own, a holistic approach capturing all of them would not be mathematically tractable.

The purpose of this chapter is to explore a simplified mathematical formulation of this problem that captures the essential large-scale dynamics. Because of the complexity of the problem, the resulting equations are very complicated, making it difficult, if not impossible, to understand the whole flow system using this approach. It turns out, however, that the equations can be solved analytically under some simple situations, where symmetry can be exploited and simplifications can be made. The formations of domes[68] and stalactites[88; 89] are examples of such situations, as is the pioneering work of Wooding on travertine dams[84]. In these systems, there is a

thin film of fluid flowing over the motif in a laminar fashion (in the case of domes and stalactites, for example). We will see that these simple motifs are straightforward to calculate in the case that capillary forces can be neglected. If the fluid film becomes too thin, due to its spreading over the surface, contact lines can be formed, resulting in rivulets and the breaking of pure rotational symmetry. In the case of domes, this is manifested in a fluting pattern near the base of the dome[68]. Such effects are difficult to include analytically, although we have previously shown that they can be captured correctly using a cell dynamical system model[68], and this is discussed in more detail below.

Although we cannot use this analytical theory to study the detailed shapes of the complex landscape of ponds and terraces, we are able to expose the dynamical linear instabilities, whose evolution into the nonlinear regime give rise to the landscape. We will see that the linear stability spectrum, in the absence of capillarity effects, always predicts a positive growth rate. The absence of a length scale arising in this calculation suggests that the actual landscapes might be scale invariant, a conclusion that is reinforced by our studies of the statistical properties of these landscapes using our cell dynamical system model and photographic evidence[68; 101]

The study reported here is a complement to our simulation work[28; 68; 101] implemented as a cell dynamical system. This model has been shown to be capable of describing the actual dynamics[68], not only in the simple cases where the analytical approach is successful, but also in the fully nonlinear regime. For example, it has been shown that this cellular model generically gives rise to a complex, terraced landscape, which is similar to the one observed in the field. The cellular model also makes detailed predictions for the landscape statistics, including the pond area distribution and the distribution of pond anisotropy. In addition, the model successfully predicts that the main mode of pond or terrace growth is uphill pond inundation, a result confirmed by time-lapse photographic studies.

Although seemingly different, both the analytical approach and the cell dynamical system approach incorporate the same physics, and so should be expected to yield identical predictions. In [68] this was tested, by using the cellular model to solve the problem of dome formation. The analytical theory in the absence of surface tension cannot account for the fluting seen away from the vent of domes, because the fluting arises from contact line formation. The analytical theory for domes, as we will discuss in detail below, contains one parameter that sets the scale for the patterns: this scale factor r_0 is a combination of the upward growth velocity, the mass transfer coefficient describing how material is incorporated into the growing substrate, the flux of water emerging from the vent, the gravitational acceleration and the fluid viscosity. When surface tension effects are included, the capillary length d_0 must also be included. Thus, our theory is a two parameter theory for the entire range of travertine depositional phenomena. The analytical theory can be used to predict the position on the dome at which capillary effects become important: this must occur at a location that is independent of the ratio r_0/d_0, and hence this critical angle has a prescribed dependence on the underlying parameters which enter into the formula for r_0. This prediction, arising from the analytical theory, was verified to occur also in the computer simulations of the cellular model[68]. As a result, we conclude that the two formulations are indeed equivalent, and may be used interchangeably depending on which is more suited to the problem at hand.

This chapter is organized as follows. In Section 3.2, we derive the equations governing the dynamics of fluid flow coupled to the moving boundary problem describing travertine precipitation. Section 3.3 describes the circularly symmetric solutions of these equations, and presents the linear stability analysis of the steady state uniformly translating solutions. We compare our analysis to a similar one[88; 89] that describes the shapes of stalactites in Section 3.4 and compute the linear stability spectrum of these structures too. We turn in Section 3.6 to a study of turbulent flow down an

inclined plane, and calculate the linear stability spectrum for the coupled flow and moving boundary problem, exposing the linear instability that is at the heart of the terraced landscape architecture. We conclude in Section 3.7.

3.2 Model for Precipitation Pattern Formation

We consider a stream of water flowing over a terrain, from which calcium carbonate is then, due to geochemical processes to be discussed below, precipitated onto the landscape. The landscape is thus constantly changing in response to the fluid flow. This change of landscape, in turn, affects the flow path of the fluid, which then influences how subsequent precipitation takes place. We derive the governing equations describing both fluid flow and surface growth. We first focus on the surface growth, and related precipitation dynamics, and then move onto the fluid flow. These two aspects will be combined to provide the complete description of the system.

3.2.1 Surface Growth

A surface can generally be characterized by the local curvature, κ. In one dimension, or in cases where symmetry reduces the system to be effectively one dimensional, κ is defined by

$$\kappa = \frac{\partial \theta}{\partial s}, \tag{3.1}$$

where θ is an angle between the local tangent of the curve and a fixed axis, and s is the arc length measured from some fixed point on the curve, as shown in Fig. (3.2). If the normal velocity v_n of the surface is prescribed everywhere, then the evolution of the curvature follows the kinematic equation[102–104]:

$$\left.\frac{\partial \kappa}{\partial t}\right|_{\theta} = -\kappa^2 \left(1 + \frac{\partial^2}{\partial \theta^2}\right) v_n, \tag{3.2}$$

The time derivative in the equation is defined with respect to fixed θ. The first term in Eq. (3.2) describes the change in κ due to the change in the overall scale of the

object, whereas the second term describes the change in κ at a point due to the difference in growth rates in the neighborhood of that point.

Eq. (3.2) is purely geometrical; for any given function v_n, the evolution of κ is determined. So, physics enters in constructing a realistic and mathematically tractable model for v_n, which, in the case considered here, depends on water chemistry, surface kinematics, chemical advection and fluid flow state. In carbonate systems, in additional to the $CaCO_3$ concentration, precipitation is mainly controlled by the CO_2 concentration (partially reflected in the measured pH), which is also influenced by its temperature-dependent solubility in the fluid. As the pH increases or the temperature decreases, the solvability of $CaCO_3$ decreases and supersaturated $CaCO_3$ will be precipitated onto the surface. While the decrease in temperature is mainly due to heat loss to the environment, the increase in pH is due to the loss of CO_2 by a variety of outgassing mechanisms[95; 96]. Although the detailed water chemistry and depositional processes are quite complicated, for the purposes of the present work, it suffices to use a simplification of the governing chemical reactions: $Ca^{2+} + 2HCO_3^- \rightleftharpoons CaCO_3(s) + H_2O + CO_2(g)$. In summary, the system tends to produce more $CaCO_3$ as CO_2 concentration decreases through outgassing.

Mass transfer between a fluid and a solid is a complicated problem[84; 105; 106]; these nontrivial chemical processes only make it harder. A complete description of the precipitation dynamics, which will give us the normal growth velocity v_n, involves writing down, in addition to the fluid dynamics equations, advection-reaction-diffusion equations for each chemical and appropriate boundary conditions. Short *et al.*[88; 89] followed this approach in the study of stalactite formation. What they found, after solving all these equations and taking limits appropriate for the timescales of interest to them, is that v_n is proportional to the local fluid thickness, h, with all the chemistry entering only into the proportionality constant.

A simple interpretation of this result can be obtained by studying the scales of

processes involved in stalactite formation, using parameter values from Ref. [89]. The fluid flow is a laminar flow, with Reynold's number about $0.01 - 1$. The thickness of the flow, h, is typically on the order of 10μm. The time scale for the concentration of $CaCO_3$ to equilibrate across the layer is thus $h^2/D \sim 0.1$s, where D is the diffusion constant. Next, the traversal time, the time for a parcel of fluid to flow along the stalactites, is about 100s. Because only 1 percent of the total $CaCO_3$ mass is precipitated throughout the flow, we can assume that the $CaCO_3$ concentration, and thus the pH, are uniform both across the fluid layer and along the stalactite. The temperature can also be assumed to be constant since the fluid is so thin. The precipitation rate is then controlled only by the $CaCO_3$ available, which is proportional to the thickness of the fluid.

In other carbonate systems, such as at travertine-forming hot springs, this relation between v_n and h does not hold simply due to the fact that the fluid thickness is larger, and the velocity is larger; as a result a turbulent boundary layer is formed near the precipitation front. What happens outside the boundary layer is too distant to affect precipitation near the boundary. In a turbulent flow, instead of depending on h, the precipitation front velocity v_n depends on the fluid velocity[105; 106]. Wooding[84], in the study of steady-state dam formation, took this into consideration and arrived at the conclusion that v_n is directly proportional to the depth-averaged tangential fluid velocity, U, *i.e.*

$$v_n = GU, \tag{3.3}$$

where G is a mass transfer coefficient depending on water chemistry and spectral features of the turbulent flow[105; 106]. For present purposes, the functional form of G is not of interest: we shall treat it as a phenomenological parameter, and as we shall see, its role in the theory developed here is to contribute to the characteristic length scale r_0 of patterns.

To summarize: all the details of water chemistry, including supersaturation, out-

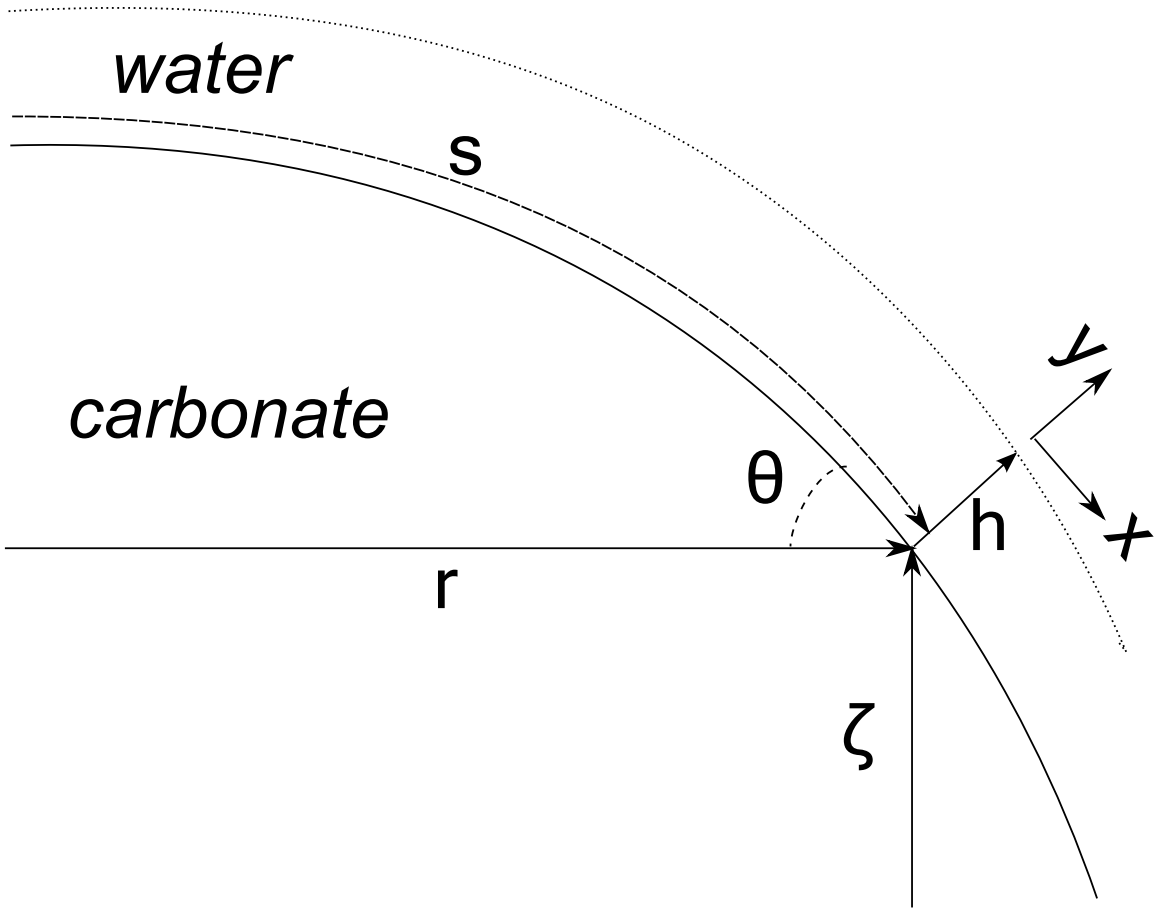

Figure 3.2: The coordinate system for the model of fluid flow coupled to precipitation moving boundary dynamics.

gassing, solute diffusion, fluid turbulence, temperature and pH, which on their own are complicated processes and are nontrivial to model, enter into the picture only through a mass transfer coefficient, G. In principle, G may exhibit spatial fluctuations; however, we shall assume that these are on a scale small compared to the features we are describing, and thus we will consider G to be a constant locally along the flow path. Over the entire geothermal spring system, it is possible that there will be a small spatial variation in the mean value of G, but the weak dependence of G on governing parameters[84; 105; 106] strongly suggests that this can reasonably be neglected.

3.2.2 Fluid Dynamics

A complete description of incompressible fluid dynamics is given by the Navier-Stokes equation

$$\frac{\partial \vec{u}}{\partial t} + \vec{u} \cdot \nabla \vec{u} = \frac{-1}{\rho} \nabla P + \nu \nabla^2 \vec{u} + \vec{g}, \tag{3.4}$$

with $\vec{\nabla} \cdot \vec{u} = 0$ for incompressibility, no-slip and stress-free boundary conditions at the solid-liquid and liquid-gas interfaces, respectively, where $\vec{u}$, ρ, P, ν and g are the fluid velocity, density, pressure, viscosity and gravitational acceleration. We will use the Poiseuille solutions of the Navier-Stokes equations for domes, where the flow is laminar, but for turbulent flows, such as those which form the travertine terraces, we will employ a depth-averaging approximation, in conjunction with the Chézy approximation[107] for hydraulic friction.

Since the spatial scale over which the landscape changes is usually much larger than the fluid thickness, *i.e.* $h\kappa \ll 1$, we can make use of the shallow water approximation and expand Eq. (3.4) in powers of $h\kappa$. If we take κ to be zero, we arrive at the de Saint-Venant equation[108]

$$\frac{\partial (Uh)}{\partial t} + \frac{\partial (U^2 h)}{\partial s} = -gh \frac{\partial h}{\partial s} + gh \sin\theta - \frac{C_f U^2}{h} \tag{3.5}$$

with equation of continuity

$$\frac{\partial h}{\partial t} + \frac{\partial (Uh)}{\partial s} = 0 \tag{3.6}$$

where C_f is the Chézy coefficient[107], which empirically describes the energy lost due to turbulence, in a manner consistent with Kolmogorov's 1941 scaling theory of turbulence (K41)[109; 110], and s is the arc length measure from a reference point at the top, as shown in Fig. (3.2).

The de Saint-Venant equation only holds on flat surfaces. When the surface grows, flow instabilities trigger various patterns to form; and the de Saint-Venant equation is no longer valid. For a general curved surface, the Dressler equation[111; 112] has

to be used:

$$\frac{1}{g}\frac{\partial u_0}{\partial t} + \frac{\partial E}{\partial s} = \frac{-C_f u^2}{gh(1-\kappa h/2)} \tag{3.7}$$

$$(1-\kappa h)\frac{\partial h}{\partial t} + \frac{\partial q}{\partial s} = 0 \tag{3.8}$$

where

$$u(s,n,t) = \frac{u_0(s,t)}{1-\kappa n}, \tag{3.9}$$

$$E(s,t) = \zeta + h\cos\theta + \frac{p_h}{\rho g} + \frac{u_0^2}{2g(1-\kappa h)^2}, \tag{3.10}$$

$$q(s,t) = -\frac{u_0}{\kappa}\log(1-\kappa h). \tag{3.11}$$

where ζ is the height of the underlying surface measured from a fixed horizontal axis, as shown in Fig. (3.2), p_h is the pressure head at the fluid surface, ρ is the fluid density, E is the energy density and q is the local flux. When κ is set to zero and θ is small, the Dressler equations reduce to those of de Saint-Venant.

As we have seen, the way fluid flows depends on the landscape it is flowing over, which itself is evolving over time. Now, Eq. (3.7)-(3.11) (or Eq. (3.4)) and Eq. (3.3) describe these two dynamics, respectively. However, we do not have to consider both dynamics on the same footing because there is a separation of time scales; the rate of fluid flow is on the order of cm/sec, but the rate of precipitation is on much slower geological scales. The latter is on the order of 1 mm/day and 1 cm/century in the cases of Yellowstone travertines[85; 113; 114] and stalactites[89], respectively. Accordingly the fluid flow responds quickly to the landscape, but the landscape responds extremely slowly to the fluid flow. We can then assume that the fluid flow is in its steady state when we discuss the landscape evolution; *i.e.*, we can drop all the time derivatives in the fluid flow equations. This quasi-stationary model will now be used to study the steady states of a variety of geological motifs and their stabilities.

3.3 Travertine Domes

3.3.1 Steady State

Our first example is the circularly symmetrical domes found in Yellowstone National Park, as shown in Fig. (3.3.1a). A number of approximations and simplifications can be made before we proceed. First, the growth rate of these domes is on the order of $1-5$mm/day and the fluid flow rate is on the order of 1mm/s, so we have a separation of time scales. Second, our field observations indicate that the thickness of the fluid film flowing over the domes is very small compared to the curvature of the surface; thus, we make the approximation that the fluid is flowing down a (locally) constant slope. Third, as suggested by the field observations, the domes have a high degree of circular symmetry, so we can assume the solution to be circularly symmetrical and focus only on the radial part of the solution, which is effectively one dimensional. Fourth, the flow is apparently laminar, so we can use the Poiseuille-Hagen profile for the velocity in thin film:

$$u(y) = \frac{gh^2 \sin\theta}{2\nu}\left[2\frac{y}{h} - \left(\frac{y}{h}\right)^2\right], \tag{3.12}$$

where θ is the slope of the surface and y is the transverse coordinate, as shown in Fig. (3.2). By assuming circular symmetry, h can be related to the axial distance from the vent, r, by the conservation of fluid volume:

$$Q = 2\pi r \int_0^h u(y)dy = \frac{2\pi g r h^3 \sin\theta}{3\nu}, \tag{3.13}$$

where Q is the total volumetric flux coming out of the vent. Eq. (3.12) and (3.13) can be combined to give

$$U \equiv \frac{1}{h}\int_0^h u(y)dy = \left(\frac{\alpha \sin\theta}{r^2}\right)^{1/3}, \tag{3.14}$$

where $\alpha \equiv gQ^2/12\pi\nu$. We will see later that the assumption of laminar flow is self-consistently verified. Putting Eq. (3.14) into Eq. (3.2) and using Eq. (3.3), gives

$$\left.\frac{\partial\kappa}{\partial t}\right|_\theta = -\kappa^2\left[1+\frac{\partial^2}{\partial\theta^2}\right]G\left(\frac{\alpha\sin\theta}{r^2}\right)^{1/3}. \tag{3.15}$$

This is the governing equation for the dome profile. Suggested by the shape of the dome, we seek a solution which steadily translates upwards without a change of shape, *i.e.*, $\partial_t\kappa|_\theta = 0$, with velocity v_t. Eq. (3.15) gives

$$G\left(\frac{\alpha\sin\theta}{r^2}\right)^{1/3} = v_t\cos\theta, \tag{3.16}$$

Rearranging terms gives the shape of the dome as a one-parameter family of curves

$$\frac{r(\theta)}{r_0} = \sqrt{\frac{\sin\theta}{\cos^3\theta}}, \tag{3.17}$$

where the scale factor $r_0 \equiv \sqrt{G^3\alpha/v_t^3}$. Eq. (3.17) is plotted in Fig. (3.3.1b). Good agreement is obtained between our theory and the observations below a critical angle θ_c. From the fit, and the typical parameter values $G \sim 10^{-8}$, $v_t \sim 1$mm/day and $Q \sim 1\text{cm}^3/\text{sec}$, we obtain $U \sim 25$mm/sec and $h \sim 1-10$mm, and a Reynolds number, $\text{Re} \equiv Uh/\nu \sim 10-100$. The assumption of laminar flow is self-consistently verified.

The agreement between this analysis and observation shows that the growth of the dome is mainly determined by the geometry, because the only r dependence enters through the mass conservation, which is determined by geometry. To see this, suppose that the dome was a one dimensional object. Then, the mass conservation equation, Eq. (3.13), would become $Uh = q_0$, for some constant flux q_0, without any r dependence. Under the same approximation of local flatness, the final equation for U, Eq. (3.14), would thus be independent of r. We would then not be able to solve for r by substituting U into Eq. (3.2). In this case, we would have to solve the equations without using the locally-flat approximation. In other words, the fact that we can ignore the details of the flow, by assuming local flatness, to obtain the shape

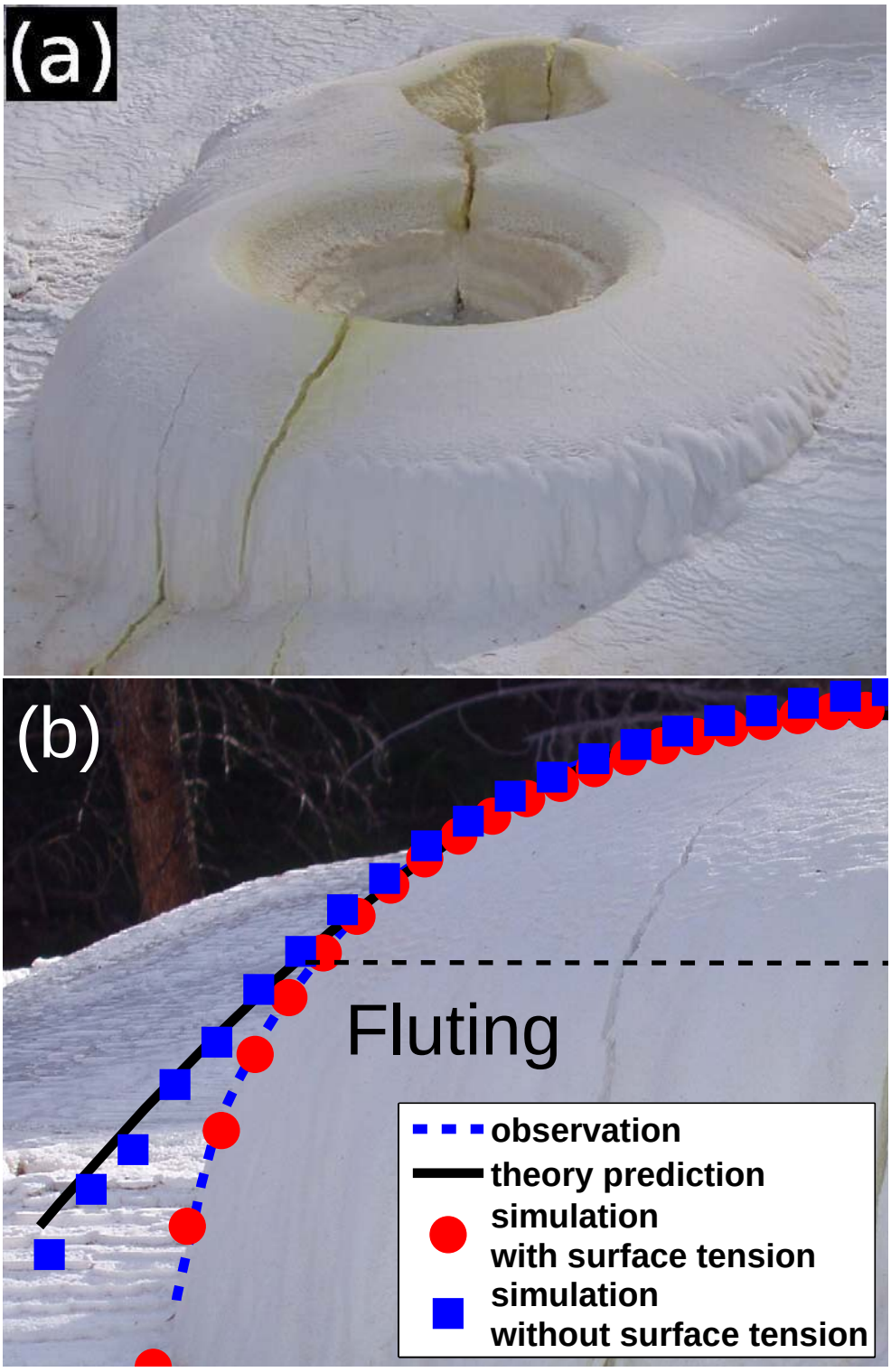

Figure 3.3: (Color online) Travertine dome at Mammoth Hot Springs, WY. (a) Dome whose central pond is 50.3cm in diameter. (b) Dome profile compared with theory and simulation of Ref. [68]. The black curve is the analytical prediction from Eq. (3.17), using the value $r_0 = 43cm$. The red filled circles show the profile of a simulated dome, including the effects of surface tension. The blue dashed line is a consensus dome profile generated by averaging the dome shown with one other field observation. The blue filled squares show the profile of a simulated dome without surface tension[68].

of the domes implies that geometry plays a more important role than fluid flow in the formation of domes.

For angles $\theta > \theta_c$, the analytical profile deviates from our field photograph. The point of deviation is associated with an apparent change in the dome morphology, with a fluting pattern superimposed on the dome profile. This is due to the effects of surface tension at the air-water-travertine interface[68]. Instead of covering the whole surface uniformly, the fluid separates and covers only a fraction of the surface. Along the wetted surface, the regular growth law still applies and thus the surface grows, until a point at which the difference in heights between the wetted and dry surfaces is so large that the flow changes its path to flow along the dry surface. This process repeats itself and, on average, results in a slower growth when compared with a uniformly-wetted dome, so the theoretical prediction should be higher than the observation for $\theta > \theta_c$, as seen in Fig. (3.3.1b). The analytical solution for the dome profile neglects surface tension, but leads to a prediction for the scaling dependence of the critical angle on the model parameters[68].

It is not trivial to include surface tension in our analytical model, but its effect can be examined by using the cellular model, in which one can switch on and off surface tension. Fig. (3.3.1b), reproduced from Ref. [68] shows the prediction of dome shapes from the cellular model with and without surface tension. It is clear that by appropriate choice of d_0 the simulation result coincides with the observation when surface tension is present, and agrees with the analytical prediction otherwise. This is direct evidence for the effect of surface tension near fluting.

For completeness, we mention that this is not an artifact of having "enough fitting parameters to fit an elephant". In Ref. [68] was presented a scaling argument for the critical angle at which capillary effects become important. The inclusion of surface tension introduces an additional length scale, namely, the capillary length, d_c, into the problem. Now, the only other length scale in the problem is $r_0 = \sqrt{gG^3Q^2/\nu v_t^3}$.

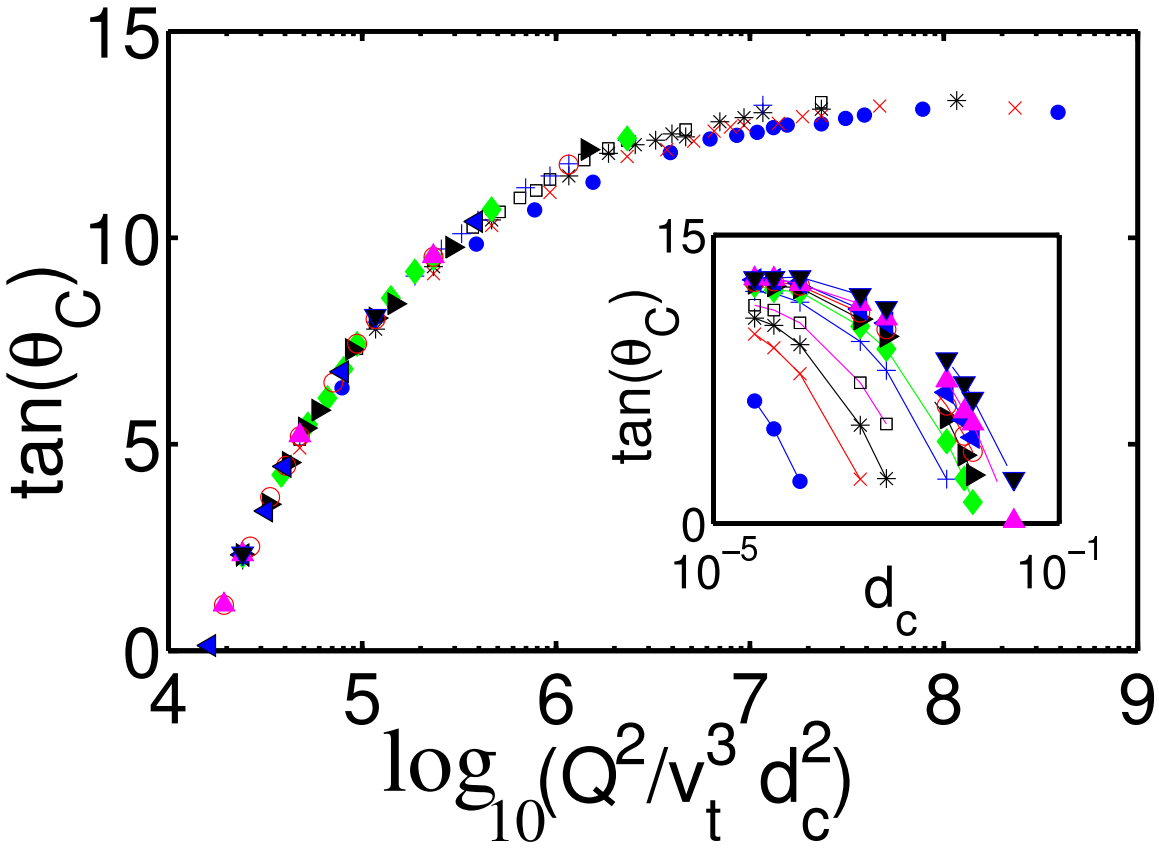

Figure 3.4: (Color online) Critical angle for the contact line formation on a travertine dome, plotted according to Eq. (3.18), showing data collapse, as predicted by theory. Inset: raw data.

Since θ_c is dimensionless, it can only depend on the ratio r_0/d_c and G. For a given chemical environment, G is fixed and we are left with the prediction, derived from our analytical solution, that

$$\theta_c = \hat{f}\left(\frac{\sqrt{gQ^2/\nu v_t^3}}{d_c}\right), \tag{3.18}$$

where $\hat{f}(x)$ is a scaling function. This data collapse, which predicts θ depends not on the parameters separately, but only on the combination $\sqrt{(gQ^2/\nu v_t^3)}/d_c$, was verified using our discrete cellular model[68], wherein the form of $\hat{f}(x)$ was calculated. It is shown in fig. 3.4.

3.3.2 Linear Stability Analysis

To complete the analysis, we study the stability of the solution, Eq. (3.17). By following the approach Liu and Goldenfeld used in studying the linear stability of dendritic solidification[115], we consider a perturbed solution, $r(\theta) = \bar{r}(\theta) + \delta r(\theta) e^{\lambda t}$, where $\bar{r}(\theta)$ is the solution in Eq. (3.17) and δr is a perturbation. Substituting this into the governing equation, Eq. (3.15), and expanding in δr, we obtain

$$\lambda \frac{d\delta r}{d\theta} + \frac{2G\alpha^{1/3}\cos\theta}{3}\left[1 + \frac{d^2}{d\theta^2}\right]\frac{\delta r \sin^{1/3}\theta}{\bar{r}^{5/3}} = 0, \tag{3.19}$$

where the boundary conditions are

$$\delta r(0) = 0, \qquad \delta r\left(\frac{\pi}{2}\right) = 0, \tag{3.20}$$

for symmetric modes and,

$$\frac{d(\delta r(0))}{d\theta} = 0, \qquad \delta r\left(\frac{\pi}{2}\right) = 0, \tag{3.21}$$

for antisymmetric modes. This is an eigenvalue problem and the spectrum tells us the stability of the solution. It is sufficient to examine the asymptotic behaviors of δr for different values of λ to extract sufficient information about the stability. Expanding Eq. (3.19) in small θ gives

$$\frac{d^2\delta r}{d\theta^2} - \frac{1}{\theta}\frac{d\delta r}{d\theta} + \frac{3}{4\theta^2}\delta r = 0, \tag{3.22}$$

which is independent of λ and which possesses power-law solutions of the form $\delta r \sim \theta^{1/2}, \theta^{3/2}$. These correspond to the symmetric and antisymmetric modes respectively.

The asymptotic behavior in the opposite limit can be studied by making the transformations $g(\theta) = \delta r(\theta)\sqrt{\cot\theta}$ and $x = \tan\theta$, which results in

$$\frac{d^2 g(x)}{dx^2} + p(x)\frac{dg(x)}{dx} + q(x)g(x) = 0, \tag{3.23}$$

where

$$p(x) = \lambda'\sqrt{x(1+x^2)} - \frac{2x}{1+x^2}, \tag{3.24}$$

$$q(x) = \frac{\lambda'\sqrt{1+x^2}}{2\sqrt{x}} + \frac{2x^2-1}{(1+x^2)^2}, \tag{3.25}$$

and,

$$\lambda' \equiv \frac{3\alpha^{1/6}G^{3/2}\lambda}{2v_t^{5/2}}. \tag{3.26}$$

The asymptotic behaviors of these functions, as $x \to +\infty$, are

$$p(x) \sim \lambda' x^{3/2} + \frac{\lambda'}{2x^{1/2}} - \frac{2}{x} + O\left(\frac{1}{x^{5/2}}\right), \tag{3.27}$$

and,

$$q(x) \sim \frac{\lambda' x^{1/2}}{2} + \frac{\lambda'}{4x^{3/2}} + \frac{2}{x^2} + O\left(\frac{1}{x^{7/2}}\right). \tag{3.28}$$

The asymptotic behavior of $g(x)$ as $x \to +\infty$, for positive values of λ', can be computed by defining $g(x) \equiv \exp(S(x))$, where $S(x)$ satisfies

$$\frac{d^2S}{dx^2} + \left(\frac{dS}{dx}\right)^2 + p(x)\frac{dS}{dx} + q(x) = 0. \tag{3.29}$$

Using the eikonal approximation that $S''(x) \ll (S'(x))^2$, which is valid for $x \to +\infty$, Eq. (3.29) can be solved asymptotically to give the two linearly independent solutions

$$S_1(x) \sim \frac{-2\lambda'}{5}x^{5/2} - \lambda' x^{1/2} + \ln(x), \tag{3.30}$$

and,

$$S_2(x) \sim \frac{-1}{2}\ln(x), \tag{3.31}$$

which are equivalent to,

$$g_1(x) \sim \frac{1}{x}\exp\left(\frac{-2\lambda'}{5}x^{5/2} - \lambda' x^{1/2}\right), \tag{3.32}$$

and,

$$g_2(x) \sim \frac{1}{\sqrt{x}} + \frac{3}{2\lambda x^3} - \frac{7}{4\lambda x^5} + O\left(\frac{1}{x^{11/2}}\right), \tag{3.33}$$

where a series expansion in the form of,

$$g_2(x) = \frac{1}{\sqrt{x}}\sum_{n=0}^{\infty}\frac{a_n}{x^{n/2}}, \tag{3.34}$$

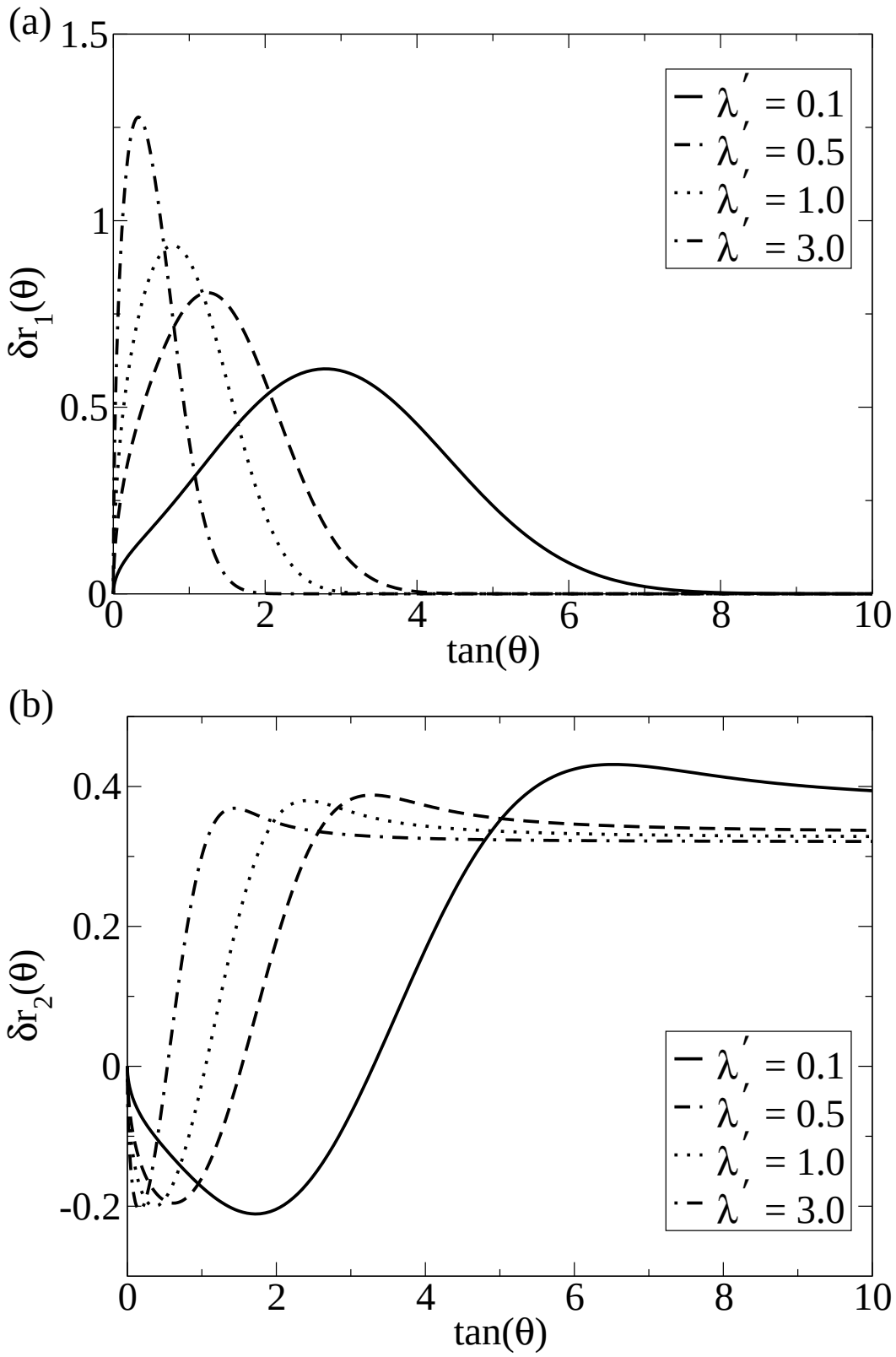

Figure 3.5: The eigenfunctions of Eq. (3.19) for $\lambda' = 0.1$, 0.5, 1.0 and 3.0. (a) The first eigenfunction satisfies the boundary conditions for symmetric modes, implying the instability of the dome solution. (b) The second eigenfunction does not satisfy the boundary condition at infinity.

is performed to arrive at Eq. (3.33).

We see from the asymptotic formula, Eq. (3.33), that,

$$\delta r_2(x) \equiv \sqrt{x} g_2(x) \sim 1 + O\left(\frac{1}{x^{5/2}}\right), \tag{3.35}$$

as $x \to \infty$ or $\theta \to \pi/2$. This means that $\delta r_2(\theta)$ does not satisfy the boundary condition, $\delta r(\theta = \pi/2) = 0$. The solution, $\delta r_1(\theta)$, is the only solution that satisfies the boundary conditions, Eq. (3.20).

To obtain the full eigenfunctions, we use the asymptotic formula, Eq. (3.32) and (3.33), as initial conditions and integrate numerically from a large value of $x = c$ ($c = 10$ in this case) back to $x = 0$. The Gram-Schmidt orthonormalization procedure is employed to ensure the linear independence of the two eigenfunctions. The eigenfunctions are normalized such that

$$\int_0^c \delta r_i(x) \delta r_j(x) dx = \delta_{ij}. \tag{3.36}$$

Fig. 3.5 shows $\delta r_1(\theta)$ and $\delta r_2(\theta)$ for $\lambda' = 0.1$, 0.5, 1.0 and 3.0. From the graph, we confirm that $\delta r_1(\theta)$ satisfies the boundary conditions, Eq.(3.20), while $\delta r_2(\theta)$ does not.

Note that $\delta r_1(\theta)$ satisfies only the boundary conditions for the symmetric modes, but not the anti-symmetric modes. We need a linear combination of $\delta r_1(\theta)$ and $\delta r_2(\theta)$ to form a solution that satisfies the latter. But since $\delta r_2(\theta)$ does not satisfy the boundary condition at $\theta = \pi/2$, such a linear combination would not satisfy it either.

To conclude, there are always solutions to Eq. (3.19) satisfying the boundary conditions for the symmetric modes for every positive value of λ, *i.e.*, the domes are unconditionally linearly unstable. This seems to be a contradiction with the field observation of domes, which are presumably stable. We will postpone the discussion of this issue to the end of the next section, after we have discussed stalactite formation.

3.4 Stalactites

In studying the formations of travertine domes near geothermal hot springs, it helps to study a similar geophysical process, namely, the formation of stalactites, which are cylindrical structures formed by precipitation of calcium carbonate in limestone caves. Here, we will summarize the results Short *et al.*[88; 89] obtained and apply our formulation to study the stability of stalactites.

3.4.1 Steady State

As discussed earlier, the growth rate of stalactites is directly proportional to the local fluid thickness, h. From the field observation, stalactite formation shares the following features with dome formation: They both are circularly symmetrical, formed under a shallow water laminar flow, and can be assumed to be locally flat. So, by using the analysis of dome formation, in particular, from Eq. (3.13), we have

$$h = \left(\frac{\beta}{r\sin\theta}\right)^{1/3}, \tag{3.37}$$

where $\beta \equiv 3\nu Q/2\pi g$ is a constant. The dynamical equation, Eq. (3.2), then becomes

$$\left.\frac{\partial\kappa}{\partial t}\right|_{\theta} = -\kappa^2\left(1+\frac{\partial^2}{\partial\theta^2}\right)\left[G\left(\frac{\beta}{r\sin\theta}\right)^{1/3}\right], \tag{3.38}$$

where G depends on water chemistry and the input flux[88; 89]. Following the same strategy employed in the case of travertine domes, we obtain a uniformly translating solution,

$$r(\theta) = \frac{r_0}{\sin\theta\cos^3\theta}, \tag{3.39}$$

where the tip velocity v_t comes in as an integration constant, and the scale $r_0 \equiv \beta(G/v_t)^3$. By defining $\rho \equiv r/r_0$, $z \equiv \zeta/r_0$ and using the trigonometric relation $\tan\theta = -dz/d\rho$, we obtain

$$\frac{z'}{(1+z')^2} + \frac{1}{\rho} = 0, \tag{3.40}$$

which is the result derived in Refs. [88; 89].

3.4.2 Linear Stability Analysis

We study the stability of solution Eq. (3.39) by introducing a perturbation:

$$r(\theta) = \bar{r}(\theta) + \delta r(\theta) e^{\lambda t}, \tag{3.41}$$

where $\bar{r}$ is the unperturbed solution given by Eq. (3.39) and δr is the perturbation. Substituting Eq. (3.41) into Eq. (3.38) and expanding the resulting equation in δr gives

$$\lambda' \frac{d\delta r}{d\theta} + \cos\theta \left[1 + \frac{d^2}{d\theta^2}\right] \left(\delta r \sin\theta \cos^4\theta\right) = 0, \tag{3.42}$$

where $\lambda' \equiv 3G^3\lambda/v_t^4$. We follow the same approach as in the case of the dome and study the asymptotic behaviors of the solutions of Eq. (3.42). For $\theta \to 0$, we expand Eq. (3.42) in θ and obtain

$$\lambda' \frac{d\delta r}{d\theta} + \left[1 + \frac{d^2}{d\theta^2}\right] \theta \delta r = 0, \tag{3.43}$$

whose solution is given by $r \sim \theta^\sigma$, where $\sigma = -1 - \lambda$. Because $\sigma < 0$ for all $\lambda > 0$, the solution diverges as $\theta \to 0$. This shows that there are no eigenmodes for $\lambda > 0$. As a result, we conclude that the steady-state solution Eq. (3.39) is linearly stable against the class of perturbations considered here.

Let us also look at the asymptotics as $x \to \infty$ for completeness. Following the strategy employed in the study of dome stability, we make the transformation $g(\theta) = \tan\theta \delta r(\theta)$ and $x = \tan\theta$. Eq. (3.42) then becomes

$$\frac{d^2 g}{dx^2} + u(x)\frac{dg}{dx} + v(x)g(x) = 0, \tag{3.44}$$

where

$$u(x) = \frac{-8x}{1+x^2} + \frac{\lambda'(1+x^2)^{3/2}}{x}, \tag{3.45}$$

and,

$$v(x) = \frac{\lambda'(1+x^2)^{3/2}}{x^2} + \frac{20x^2 - 5}{(1+x^2)^2} + \frac{1}{(1+x^2)^{5/2}}. \tag{3.46}$$

As $x \to \infty$,

$$u(x) \sim \lambda' x^2 + \frac{3\lambda'}{2} - \frac{8}{x} + \frac{3\lambda'}{8x^2} + \frac{8}{x^3} + O\left(\frac{1}{x^4}\right), \tag{3.47}$$

and,

$$v(x) \sim \lambda' x + \frac{3\lambda'}{2x} + \frac{20}{x^2} + + \frac{3\lambda'}{8x^3} + O\left(\frac{1}{x^4}\right). \tag{3.48}$$

By following the same asymptotic analysis as we did in the last section, we get,

$$g_1(x) \sim \exp\left(\frac{-\lambda' x^3}{3} - \frac{3\lambda' x}{2}\right), \tag{3.49}$$

and

$$g_2(x) \sim \frac{1}{x} + \frac{10}{\lambda' x^4} - \frac{98}{5\lambda' x^6} + O\left(\frac{1}{x^7}\right). \tag{3.50}$$

These can be used as the initial conditions to integrate numerically from a large value of x, giving the full eigenfunctions. Again, the Gram-Schmidt orthonormalization procedure is employed. The two branches of solutions, $\delta r_{1,2}(\theta)$, are plotted in Fig. 3.6. They do not satisfy the boundary conditions as they both diverge at $\theta = 0$. So the stalactite solution is stable.

3.5 Comparison Between Domes and Stalactites

We have shown that there is a continuous spectrum of unstable modes for travertine domes, but stalactites, which are formed by an apparently similar process, are predicted to be linearly stable. We need to (a) explain why it is that domes can be observed in the field, and (b) interpret the source of the difference in stability between the two seemingly-related growth motifs. We initially found it surprising that there is a qualitative difference in stability, even though the dynamics of domes and stalactites seem to differ in only relatively minor ways: the growth of domes depends on the depth-averaged fluid velocity whereas the growth of stalactites depends on the fluid thickness. In both cases, the approximation of local flatness is used, so this is unlikely to be the source of the difference.

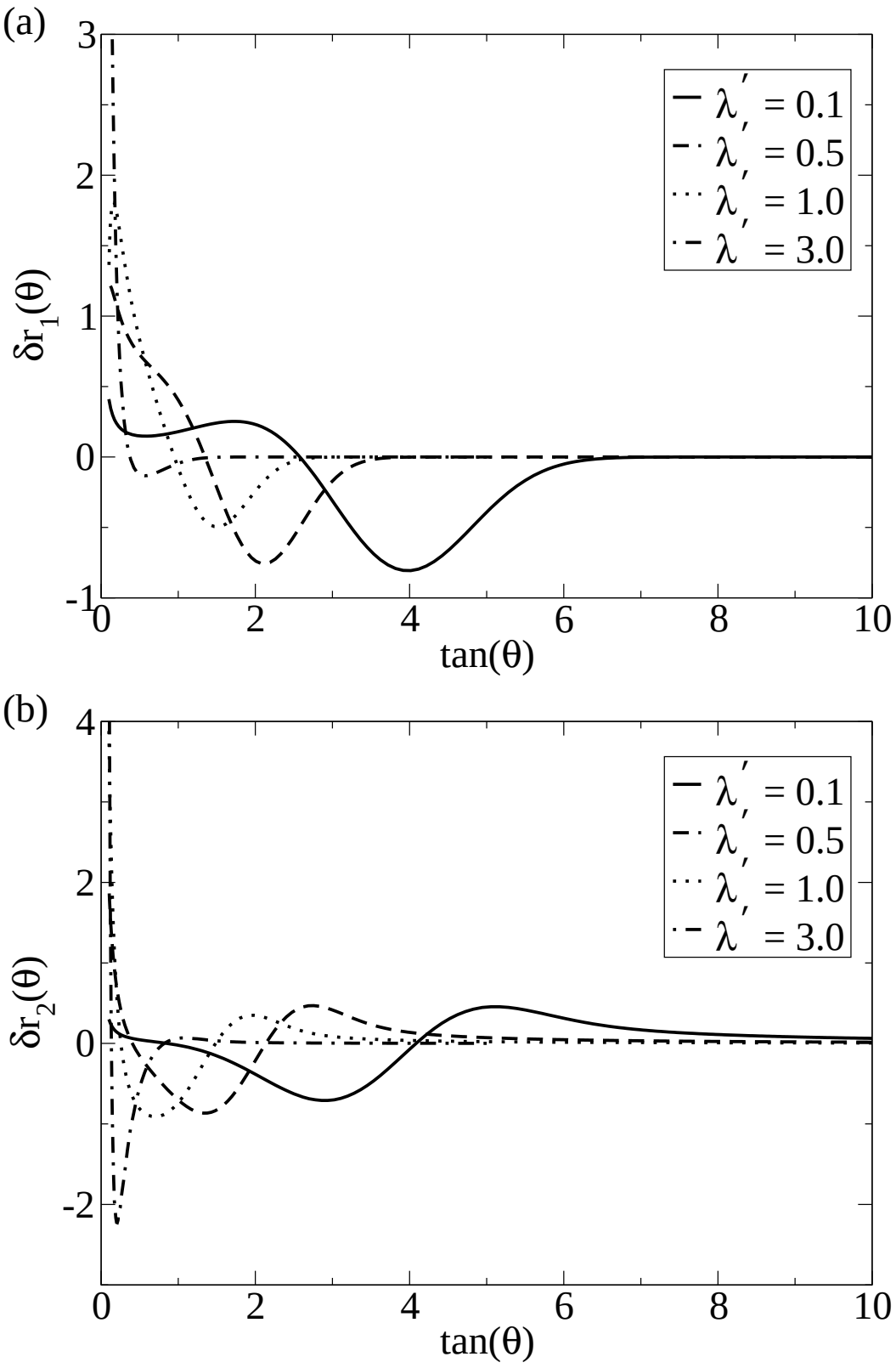

Figure 3.6: The eigenfunctions of Eq. (3.42) for $\lambda' = 0.1$, 0.5, 1.0 and 3.0. These solutions do not satisfy the boundary conditions, as they all diverges at $\theta = 0$.

Our interpretation is that the difference in stability arises from the direction of growth, and as a result, the manner in which surface tension effects correct the zeroth order solutions we have discussed. The direction of growth is important, because it dictates the way in which shape perturbations propagate. For domes growing with sufficiently large v_t, shape perturbations are advected away from the vent down the body of the dome, in a manner reminiscent of the way in which shape perturbations are advected down the body of a growing dendrite[116]. These perturbations may also grow during this process, but the development of this instability is in practice regularized by any non-zero surface tension, leading to contact line formation, film break-up and the formation of rivulets. This heuristic argument is supported by the shape of the linear stability eigenfunctions shown in Fig. 3.5. For stalactites, on the other hand, the fluid becomes increasingly thick as it flows down towards the tip, and perturbations only increase the growth velocity of the tip, rather than cause growing instabilities away from the tip. Thus, the only place where surface tension is significant is at the tip of the stalactite, where the surface tension holds a water droplet until the droplet becomes too heavy and drops. This dynamics, we believe, mainly contributes to the precipitation rate at the tip, which affects only the growth rate of the whole stalactite. In other words, it only renormalizes the value of v_t, which, in any case, is a fitting parameter. Surface tension is, therefore, not important in the dynamics of stalactite formation and it should not affect its stability.

Returning now to the case of travertine domes, we conclude that the unstable modes are small near the vent and grow in amplitude near the tail of the dome. This, however, is precisely the region where the film becomes thin and contact line formation can occur, leading to the fluting pattern observed in the real systems. The precipitation rate in this region is also lower, due to the depleted Ca^{2+} concentration, and this helps stabilizing the domes too. It is possible that the growth of the instabilities predicted here triggers the formation of contact lines and film break-up. Thus, we

conclude that the dome is in some sense similar to the problem of dendritic growth, where a smooth tip is followed by a train of sidebranches, widely interpreted to be due to a noise-induced instability[117; 118]. It is possible that the full inclusion of surface tension in the model would have as important a role in selection and stability as it does in dendritic growth[119; 120].

3.6 Damming Instability

Having studied the formation of domes and stalactites, we now try to understand some aspects of the large scale morphology of hot spring landscapes. We see in Fig. 3.1b that the pattern formed is complicated, with ponds of similar shapes but different sizes. Empirical data shows that the distribution of pond sizes indeed follows a power law[28]. This scale-invariant pattern hints at an underlying scale-invariant precipitation dynamics, *i.e.*, a dynamics without a characteristic length scale.

It is difficult to predict analytically the statistical properties of the landscape, such as the pond size distribution, due to the mathematical complexity of the equations involved. We can, nevertheless, study a simple case of precipitation over a planar slope. By studying the linear stability of this dynamics, we should be able to expose the essential physics of the formation of these scale-invariant patterns. The nonlinear regime of the modeling can be studied using the cellular model we introduced earlier. In this section, we consider a one-dimensional flow down an inclined plane, and evaluate the linear stability spectrum.

The fluid flow in travertine systems is, unlike in the cases of dome and stalactite formations, generally turbulent. It is therefore necessary to use the formulation of Eq. (3.7)-(3.11). The turbulent drag leads to a steady flow regime, about which we linearize. Since the angle θ is the same along a constant slope, it is more convenient to use the arc length, s, as the independent variable in the growth equation, so the

dynamics of local curvature, κ, is given by

$$\left.\frac{\partial \kappa}{\partial t}\right|_n = -\left(\kappa^2 + \frac{\partial^2}{\partial s^2}\right) G u_0, \tag{3.51}$$

where the subscript n denotes a derivative taken at a point moving along the outward normal of the curve. This, together with the Dressler equation, Eq. (3.7)-(3.11), gives the complete description of the system.

We scale the independent variables to their natural units,

$$t' = \frac{U}{R} t, \quad s' = \frac{s}{R}, \quad \zeta' = \frac{\zeta}{R}, \tag{3.52}$$

and define the following dimensionless variables,

$$u_0' = \frac{u_0}{U}, \quad h' = \frac{h}{H}, \quad \kappa' = R\kappa, \quad \sigma \equiv \frac{H}{R}, \tag{3.53}$$

where U, H and R are the characteristic scales of the fluid velocity, fluid thickness and the landscape respectively, and σ is the ratio between the H and R, which is small in the regime of shallow water flow. The governing equations then become (we drop all the primes on the variables for simplicity),

$$\left.\frac{\partial \kappa}{\partial t}\right|_n = -\left(\kappa^2 + \frac{\partial^2}{\partial s^2}\right) G u_0, \tag{3.54}$$

$$\sigma F_m \frac{\partial u_0}{\partial t} + \frac{\partial E}{\partial s} = \frac{-C_f F_m u_0^2}{h\left(1 - \frac{\sigma \kappa h}{2}\right)}, \tag{3.55}$$

$$(1 - \sigma\kappa h)\sigma \frac{\partial h}{\partial t} + \frac{\partial q}{\partial s} = 0, \tag{3.56}$$

with

$$E = \zeta + \sigma h \cos\theta + \frac{p_h}{\rho g} + \frac{\sigma F_m u_0^2}{2(1 - \sigma\kappa h)^2}, \tag{3.57}$$

$$q = \frac{-u_0}{\kappa} \ln(1 - \sigma\kappa h), \tag{3.58}$$

where we defined the Froude number, $F_m \equiv U^2/gR$.

The uniform solution of this set of equations is given by

$$\bar{u}_0 = \sqrt{\frac{\sin\theta}{C_f F_m}}, \tag{3.59}$$

$$\bar{h} = 1, \tag{3.60}$$

$$\bar{\theta} = \theta_0 \tag{3.61}$$

$$\bar{\kappa} = 0, \tag{3.62}$$

where θ_0 is the initial inclination of the slope. The linear stability analysis is performed by adding harmonic perturbations to the solution,

$$u_0 = \bar{u}_0 + \delta u_0 e^{ips+\lambda t}, \tag{3.63}$$

$$h = 1 + \delta h e^{ips+\lambda t}, \tag{3.64}$$

$$\theta = \bar{\theta} + \delta\theta e^{ips+\lambda t}, \tag{3.65}$$

$$\kappa \equiv \frac{\partial\theta}{\partial s} = ip\delta\theta e^{ips+\lambda t}, \tag{3.66}$$

and linearizing the resultant equations to the first order in the perturbations, resulting in three equations for δu_0, δh and $\delta\theta$,

$$ip\lambda\delta\theta = p^2 G\delta u_0 \tag{3.67}$$

$$(\lambda + ip\bar{u_0})\delta h + ip\delta u_0 - \frac{\sigma u_0 p^2}{2}\delta\theta = 0, \tag{3.68}$$

$$\begin{aligned}\sigma F_m\lambda\delta u_0 \;=\; & \delta\theta(\cos\bar{\theta} + ip\sigma\sin\bar{\theta} + p^2\sigma^2\bar{u}_0^2 F_m) \\ & -\delta\theta\frac{C_f F_m\bar{u}_0^2\sigma ip}{2} \\ & +\delta h(-ip\sigma\cos\bar{\theta} + C_f F_m\bar{u}_0^2) \\ & +\delta u_0(-ip\sigma F_m u_0 - 2C_f F_m\bar{u}_0)\end{aligned} \tag{3.69}$$

A single dispersion relation can be obtained by combining all three equations and eliminating δu_0, δh and $\delta\theta$. The result is a cubic equation in λ,

$$\lambda^3 + a_2(p)\lambda^2 + a_1(p)\lambda + a_0(p) = 0, \tag{3.70}$$

where

$$a_2(p) = 2i\bar{u}_0 p + \frac{2C_f\bar{u}_0}{\sigma}, \tag{3.71}$$

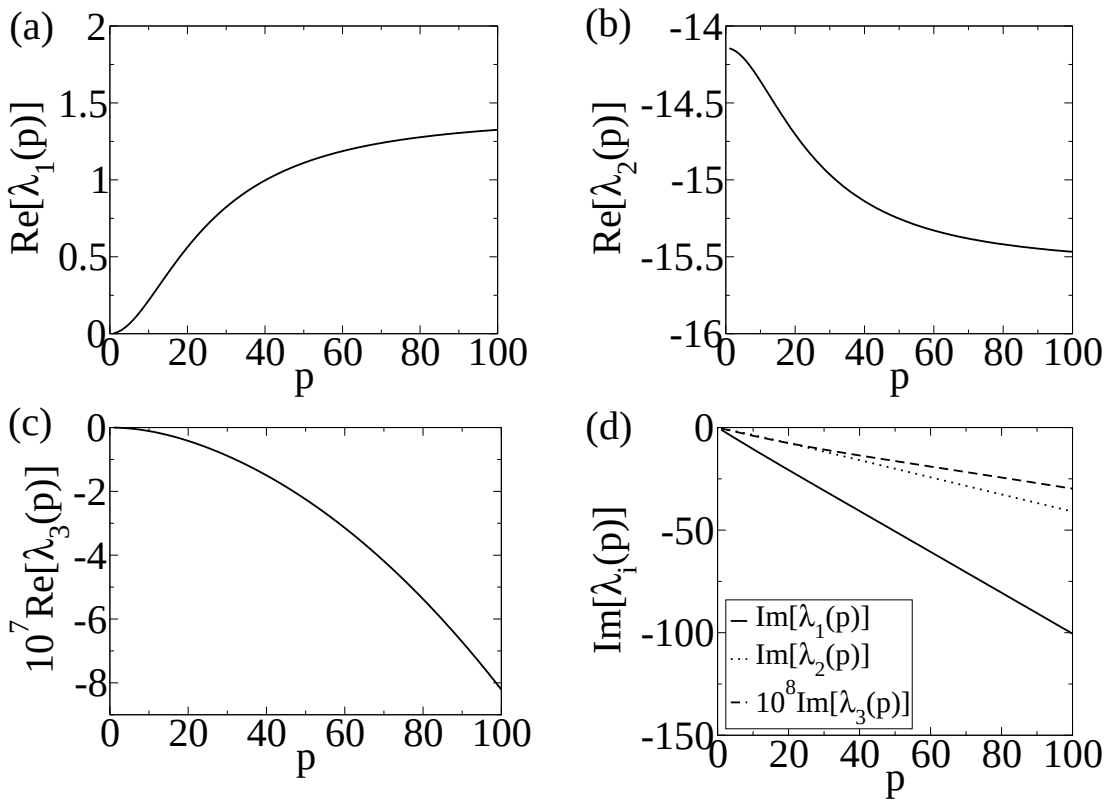

Figure 3.7: The damming instability spectrum with parameters $(\theta_0, G, F_m, C_f, \sigma) = (\pi/6, 10^{-8}, 10, 0.1, 0.01)$. (a)-(c) The real parts of the three branches of solutions. The first branch, λ_1, is positive for all p, implying that the solution is unconditionally linearly unstable. (d) The imaginary parts of the solutions.

$$
\begin{aligned}
a_1(p) &= p^3 i\sigma \bar{u}_0^2 G \\
&\quad + p^2 \left(\frac{G \sin\theta}{F_m} + \frac{C_f \bar{u}_0^2 G}{2} + \frac{\cos\bar{\theta}}{F_m} - \bar{u}_0^2 \right) \\
&\quad + p \left(\frac{iG\cos\bar{\theta}}{\sigma F_m} + \frac{3iC_f \bar{u}_0^2}{\sigma} \right), \qquad (3.72)
\end{aligned}
$$

$$
\begin{aligned}
a_0(p) &= p^4 \left(-\sigma \bar{u}_0^3 G + \frac{\sigma \bar{u}_0 G \cos\bar{\theta}}{2F_m} \right) \\
&\quad + p^3 \left(\frac{-iG\bar{u}_0}{\sin} \bar{\theta} F_m + iGC_f \bar{u}_0^3 \right) \\
&\quad + p^2 \left(\frac{-G\bar{u}_0 \cos\bar{\theta}}{\sigma F_m} \right). \qquad (3.73)
\end{aligned}
$$

For the parameter set $(\theta_0, G, F_m, C_f, \sigma) = (\pi/6, 10^{-8}, 10, 0.1, 0.01)$, the three roots of the Eq. (3.70), λ_i, are computed numerically and are plotted in Fig. 3.7. From the graph, we see the first branch of the solutions is always unstable, while the remaining two branches are always stable, implying that the solution is unconditionally linearly unstable. This is the damming instability.

To conclude, we found that the trivial flow down a constant inclined plane is unstable towards all length scales, suggesting that when fully developed into the nonlinear regime, the landscape would have no selected length scale - a surmise in accord with field observations and our cell dynamical system simulations.

3.7 Conclusion

By combining fluid dynamics and surface growth kinematics, we formulated a mathematical framework to study geological pattern formation due to carbonate precipitation and applied it to study the formation and stability of a variety of motifs. The theory successfully predicted the shape of observed spherically symmetric domes for angle θ less than a critical angle θ_c. By comparing with results from a cellular model, we showed that the departure of our theoretical prediction from observation for $\theta > \theta_c$ is due to the neglect of surface tension. We also showed that domes are linearly un-

stable towards axisymmetric perturbations, but the instability is manifested in the tail of the dome away from the vent. The instability is masked by the thinning of the fluid film and ultimately the formation of contact lines due to surface tension. This contrasted with the case of stalactites, whose growth forms are linearly stable to axisymmetric perturbations. The difference between the stabilities of the dome and stalactite solutions is attributed to the different geometries and the different role surface tension plays in these two systems.

This formulation cannot predict the complex landscape formed in the fully non-linear regime, but a linear stability analysis for a one-dimensional flow showed that the apparent scale-invariant landscape is consistent with our equations. In future work, we hope to examine the full two-dimensional instability problem, in order to investigate the dynamics of pond formation, possibly as a transverse morphological instability, akin to meandering in step-flow processes on vicinal surfaces[121].

Chapter 4

The Phase Field Crystal Model

4.1 Introduction

On macroscopic scales, material structures and properties are homogeneous and smooth; they are often characterized by such macroscopic averaged measures as density, Young modulus, shear modulus, heat and electric conductivity and magnetic permeability. On microscopic scales, however, materials are not smooth and continuous, but are composed of many different inhomogeneous domains. There may be domains with different grain orientations, domains with different electric and magnetic polarizations, precipitates with different compositions or crystal structures, as well as a variety of defects, including vacancies, dislocations, disclinations, grain boundaries and disorder. The response of these microstructures to external disturbances and the interactions between them give rise to emergent macroscopic properties. As a result, microstructures are crucial in understanding the physical properties of materials. An efficient way to simulate these structures in macroscopic samples, then, is vital to understand, predict and control material processing[49].

The goal of the work in this and succeeding chapters is to present a theory that describes both the microscopic and macroscopic scales of materials. This, at first glance, is difficult to achieve due to the presence of the inhomogeneous domains.

Fortunately, the following insight leads a way out: Because the structure within each domain is homogeneous (*e.g.*, the grain orientation is the same within any particular grain), there is almost no dynamics within each domain. As a result, one way of describing the system is to focus not on the dynamics within domains, but only on that of the interfaces that separate different domains.

There are at least two methods to accomplish this task. The first method is to write down the dynamics of the interface, by providing the normal growth velocity, v_n. This is the approach we followed in the study of dome and stalactite formations in the last chapter and relies on the concept of there being a sharp interface. It is intuitive, but as we have discussed in the previous chapter, it is only useful when the geometry is simply. For more complicated situations, this approach often results in a system of coupled nonlinear partial differential equations with moving boundary conditions at the interfaces, which are difficult to analyze both analytically and numerically. It is thus of limited use and our discussion will only focus on the second approach.

The second approach is called phase field modeling[122]. In phase field modeling, different material phases are represented by different values of one or more continuous field(s); the interfaces that separate the phases are then represented by smooth transition regions of the fields. The interfaces, thus, are diffuse and are much simpler to analyze than the moving boundaries in the sharp interface models. Moreover because there is no sharp interface, there are no boundary conditions to impose: instead the dynamics of the phase fields is specially constructed to reproduce the sharp interface behavior in the limit that the width of the transition region becomes vanishingly small. Phase field modeling has proven to be a broadly applicable, an accurate and efficient description of many non-equilibrium systems. These include spinodal decomposition[123; 124], order-disorder transition kinetics[125–127], solidification of both pure and binary systems[128–133], crack propagation[134; 135], precipitate microstructures[136] and grain growth[137–140]. A detailed review of phase

field modeling and its recent applications can be found in Ref. [122].

Although the sharp interface and the phase field approaches are very different, they essentially model the same physics. It can be shown that by taking the limit properly, the phase field model can be reduced to the sharp interface model, and the parameters of the two models can be identified[135; 141–143]. This is analogous to the fact that the analytical and the CDS approaches to the geophysical precipitation pattern formation problem presented in the last chapter are the same. This echoes the idea of universality we discussed in Ch. 1—these models are in the same universality class and they describe the same dynamics.

Although the phase field model has been successfully used to study interface dynamics, there is a major drawback: it preserves no information about the bulk, *i.e.,* all the bulk properties are ignored. In the context of modeling material microstructures, the phase field model only captures the motion of the grain boundaries, and thus the associated coarsening behavior, but not the elastic and crystallographic properties of the material in question. This renders the phase field model inappropriate to describe many phenomena, including dislocation interaction, grain rotation and polycrystalline solidification.

To overcome this limitation, several extensions and modifications to the phase field model has been proposed. Warren *et al.* [144–147], for example, proposed a phase field model with two phase fields, one describes the phase of the material (solid or liquid) and the other describes the grain orientation to account for the different grain orientations. This model incorporates crystallography and is capable of describing phenomena such as grain boundary formation and coarsening.[1] Onuki coupled an elastic free energy to the phase field model.[148] By doing so, the model is able to describe the elastic effect on various phase transition dynamics.

While many of these extensions of the phase field model are successful, the coupling

[1]Readers are referred to Ref. [62] for a more detailed discussion on this model.

of the elastic field and the phase field, in most of the cases, is unnatural. After all, elasticity, crystallography and interface structures are all emergent properties of the underlying lattice. A natural, and desirable, way to describe the system would be to associate elasticity and crystallography directly with the phase field. This is one of the reasons why the phase field crystal (PFC) model was developed.

In 2002, Elder *et al.*[60] went beyond the phase field model and proposed the phase field crystal (PFC) model, in which elasticity and crystallography are naturally incorporated. In essence, the PFC model is a density functional model. The order parameter, which is uniform except near defects and interfaces in the phase field model, is, in equilibrium, spatially periodic; the ground state of the PFC model is a perfectly triangular lattice or any other desired structure. Crystallography is then naturally captured by the orientation of the lattice, and as we will see, elasticity is also captured by this periodic ground state.

In this chapter, the PFC model is introduced. The basic properties and some of the recent developments of the model are also discussed.

4.2 From Phase Fields to Phase Field Crystals

We begin our discussion by briefly reviewing some basics of phase field modeling. Phase field modeling was originally developed to model systems with multiple states or phases separated by some interfaces. Examples are the liquid-solid interface in dendritic growth, as well as phase interfaces in spinodal decomposition and eutectic growth[122]. Phase field models take advantage of the fact that the phases (solid or liquid) are almost homogeneous within each domain, so that the dynamics of the bulk can be well captured by the dynamics of interfaces. Mathematically, a phase field, $\phi(\vec{x})$, is introduced. The value of the $\phi(\vec{x})$ is constant within each domain and varies only near interfaces and defects. A free energy of $\phi(\vec{x})$ is then posited, based on the

symmetry, dimensionality and phenomenology of the system. The dynamics of the system is given by the relaxation to the equilibrium state. The phase field model, thus, is essentially a minimal model for describing interface dynamics.

Let us take spinodal decomposition in A-B alloys as an example. If a high temperature homogeneous mixture of A-B alloy is quenched below the critical temperature and above the spinodal line, the system is unstable towards forming small zones of A-rich and B-rich phases. These small zones coarsen in time. To describe this transition, it is sufficient to capture the fact that there are two ground states and that any interface between the two phases costs energy. This intuition is captured by the free energy

$$F = \int d^d x \left(\frac{1}{2} |\nabla \phi(x)|^2 + f(\phi(x)) \right), \tag{4.1}$$

where $\phi(x)$ is the difference in concentrations of the two phases. The first term in this free energy models the interface energy between different domains of phases; the second term, on which the only requirement is to exhibit a double-well potential, forces the field to choose between two ground states (two phases). The dynamics is assumed to be dissipative and conservative: it drives the system to a lower energy state by imposing the dynamical equation

$$\frac{\partial \phi}{\partial t} = \Gamma \nabla^2 \frac{\delta F}{\delta \phi} + \zeta, \tag{4.2}$$

where the Laplacian operator on the right imposes the conservation law and ζ is a conservative thermal noise satisfying the fluctuation-dissipation theorems

$$\langle \zeta(\vec{x}, t) \zeta(\vec{x}', t') \rangle = -\Gamma k_B T \nabla^2 \delta(\vec{x} - \vec{x}') \delta(t - t'). \tag{4.3}$$

This model is capable of describing the coarsening dynamics of spinodal decomposition; it predicts, for example, the correct dynamical scaling exponent and the spatial correlation function of the transition. A variety of non-equilibrium phenomena, as listed in the beginning of this section, can be modeled by this approach. Readers are referred to [149] for a more in-depth discussion.

In retrospect, the essence of phase field modeling is to model by ignoring the small scale, irrelevant details of the system and to focus only on the dynamics of the interfaces. It homogenizes, both spatially and temporally, all the atomic-scale details (local compositions of the alloy phases, crystallographic structures, atomic vibrations, ...) while retaining the mesoscopic interface structures. This is successful because the interface dynamics controls how patterns in these systems evolve.

In many phenomena, however, the spatial atomic structures are important and cannot be neglected. It is essential, for example, to include crystallography when studying dislocation dynamics, or when studying how grains respond under external stress. An extension of the phase field model to include the atomic spatial structure is needed. In fact, the motivation behind the PFC model is to incorporate elasticity and crystallography into the model.

The PFC model can be motivated as follows. A natural way to incorporate crystallography into the model is to have a periodic ground state, instead of a uniform one, because the crystallographic information will then be given by the spatial orientation of the state. Thus, instead of penalizing any spatial variation, as the gradient term in Eq. (4.1) does, we would like to encourage spatial periodicity in the ground state. This can be done by penalizing density configurations that do not satisfy

$$(\nabla^2 + q_0^2)\rho(\vec{x}) = 0. \tag{4.4}$$

Thus, the lowest order analytic form for the coarse-grained free energy is

$$F[\rho(x)] = \int d^d x \left[\frac{\lambda}{2}\rho(x)(\nabla^2 + q_0^2)^2\rho(x) + \frac{r}{2}\rho(x)^2 + \frac{u}{4}\rho(x)^4\right], \tag{4.5}$$

where we have used a double well potential in $f(\rho)$, *i.e.,* $f(\rho) = (r+\lambda q_0^4)\rho^2/2 + u\rho^4/4$. By assuming dissipative and conservative dynamics, as in Eq. (4.2), the dynamical equation for ρ can be written as

$$\frac{\partial \rho}{\partial t} = \Gamma\nabla^2\left[(r + \lambda(\nabla^2 + q_0^2)^2)\rho + u\rho^3\right] + \zeta. \tag{4.6}$$

Eq. (4.6) is the phase field crystal (PFC) equation, and its solution describes the evolution of materials microstructure, as we shall see below.

If we rescale all variables to their natural units by defining new variables,

$$x' = xq_0, \tag{4.7}$$

$$\rho' = \rho\sqrt{\frac{u}{\lambda q_0^4}}, \tag{4.8}$$

$$r' = \frac{r}{\lambda q_0^4}, \tag{4.9}$$

$$t' = \Gamma\lambda q_0^6 t, \tag{4.10}$$

and neglect the primes on the new variables for brevity, we arrive at the dimensionless free energy

$$F[\rho(x)] = \int d^d x \left[\frac{\rho(x)}{2}(r + (1+\nabla^2)^2)\rho(x) + \frac{\rho(x)^4}{4}\right], \tag{4.11}$$

with the dynamical equation

$$\frac{\partial\rho}{\partial t} = \nabla^2\left[(r + (\nabla^2+1)^2)\rho + \rho^3\right] + \zeta, \tag{4.12}$$

where ζ is a conserved noise defined by

$$\langle\zeta(\vec{x},t)\rangle = 0, \tag{4.13}$$

and,

$$\langle\zeta(\vec{x},t),\zeta(\vec{x}',t')\rangle = \left(\frac{-uk_BTq_0^{d-4}}{\lambda^2}\right)\nabla^2\delta(\vec{x}-\vec{x}')\delta(t-t'). \tag{4.14}$$

Note that there is no restriction on the value of $\rho(x)$, it can be positive or negative. This forbids us from naively interpreting $\rho(x)$ as a physical density. We will come back to this point in later chapters, when we introduce vacancies into the model in Chapter 7.

Eq. (4.12) is the phase field crystal (PFC) model proposed by Elder *et al.* [60; 61]. In their original paper, they followed a related approach. To describe solidification of crystals, they proposed the free energy functional

$$F[\rho(x)] = \int d^d x \left[f(\rho) + \frac{\rho}{2}G(\nabla^2)\rho\right], \tag{4.15}$$

where $f(\rho)$ is the double well potential and $G(\nabla^2)$ is an unknown function. By calculating the structure factor of the liquid phase of this free energy, they found that

$$\hat{G}(\vec{q}) = \frac{k_B T}{S_{liq}^{eq}(\vec{q})} - \left.\frac{d^2 f}{d\rho^2}\right|_{\rho=0}, \tag{4.16}$$

where $\hat{G}(\vec{q})$ is the Fourier transform of $G(\nabla^2)$ and $S_{liq}^{eq}(\vec{q})$ is the equilibrium liquid-state structure factor. Eq. (4.16) implies that we can simulate any kind of pure material using the phase field crystal model. The only input is $S_{liq}^{eq}(\vec{q})$, which can be obtained experimentally. Thus the PFC model is connected to the physical world and the physical meanings of the model parameters can be readily extracted.

For most of materials, the dominant feature of $S_{liq}^{eq}(\vec{q})$ is its first peak at $q = q_0$, where q_0 is the magnitude of the reciprocal lattice vectors. The inverse of $S_{liq}^{eq}(\vec{q})$ can then be modeled by a single well. By fitting the experimental structure factor of ^{36}Ar, Elder *et al.* used the Ornstein-Zernicke form

$$G(\nabla^2) = \lambda(q_0^2 + \nabla^2)^2. \tag{4.17}$$

which when substituted into Eq. (4.15), yields the free energy, Eq. (4.11).

4.3 Basic Properties of the PFC Model

Many basic properties of the phase field crystal model have already been reported. The phase diagram of the model has been calculated. The model has been shown to be able to describe polycrystalline solidification, vacancy diffusion, grain growth(Fig. 4.1), grain boundary energetics(Fig. 4.2 - 4.3), epitaxial growth(Fig. 4.4), fracture[61](Fig. 4.5), grain coarsening[150], elasticity[151], dislocation annihilation, glides and climb[152]. The model has been applied to the commensurate-incommensurate transition[153]. The model has also been recently related the density functional theory and extended to the case of binary alloys[154]. We discuss some of these developments in the following subsections.

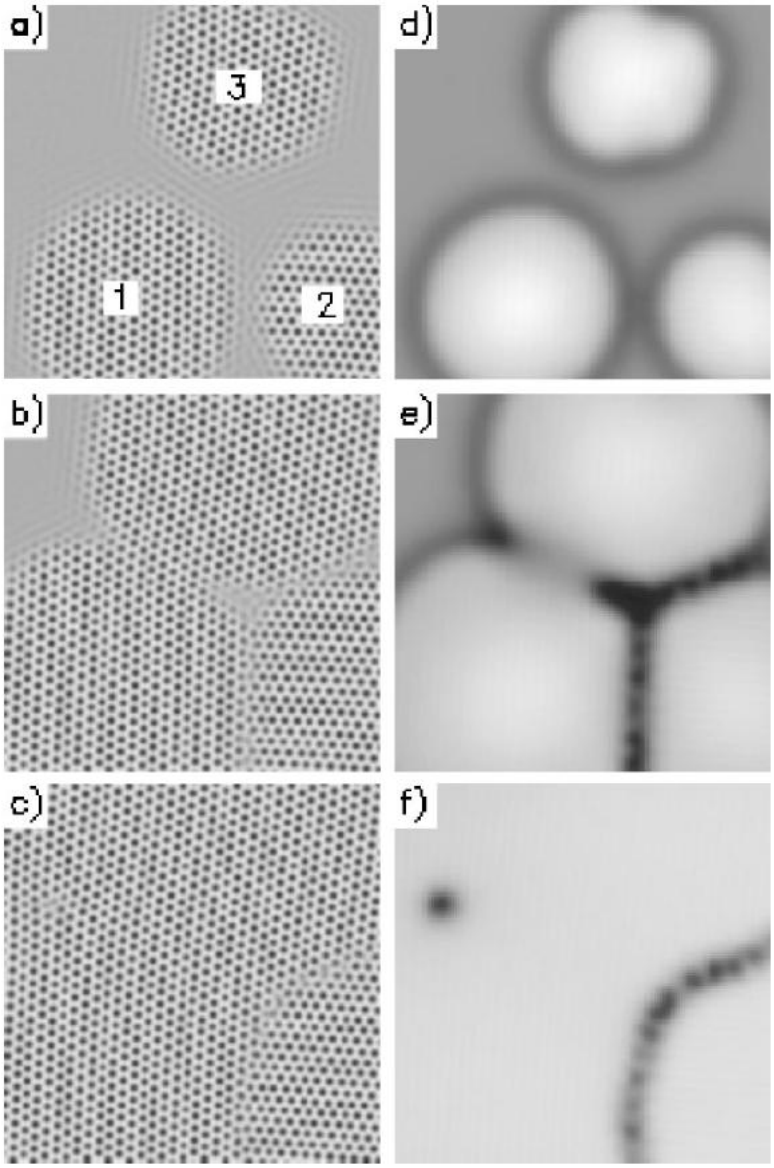

Figure 4.1: The free energy density during grain growth using the PFC model. (a), (b), (c), (d), (e), and (f) correspond to times 50, 200, 1000, 3000, 15000, and 50000, respectively. After Ref. [61].

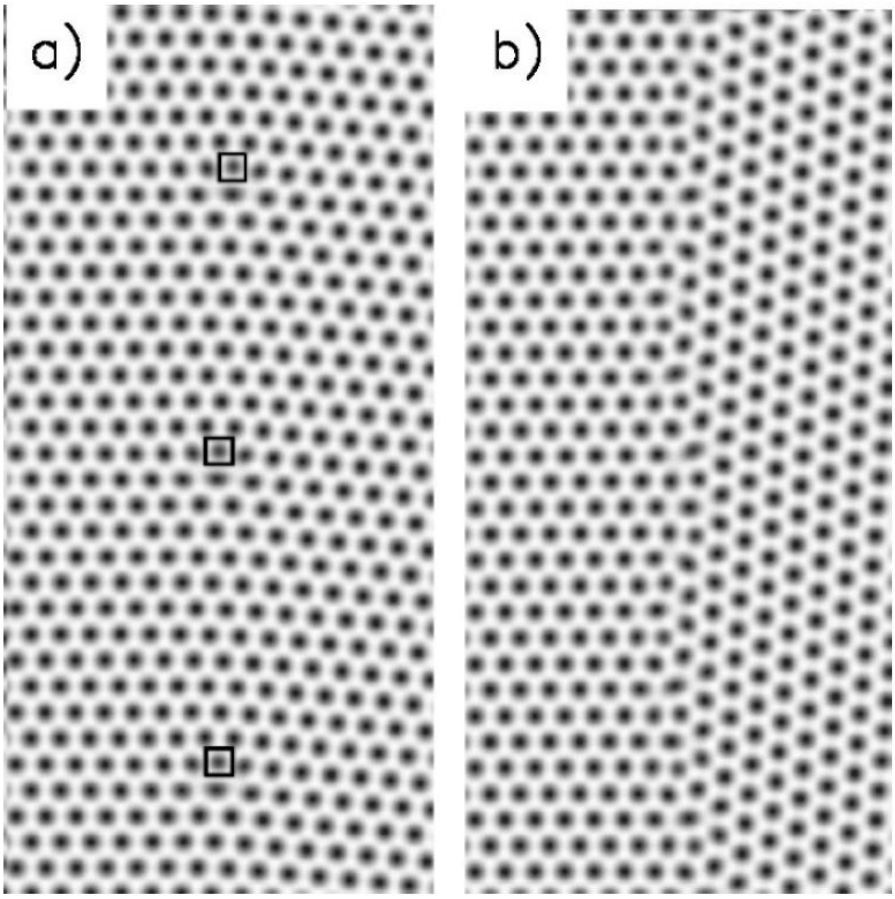

Figure 4.2: Grain boundaries with the PFC model. The density of grain boundaries with mismatch angle $\theta = 5.8$ and 34.2 are showed in (a) and (b) respectively. In (a) squares have been placed at defect sites. After Ref. [61].

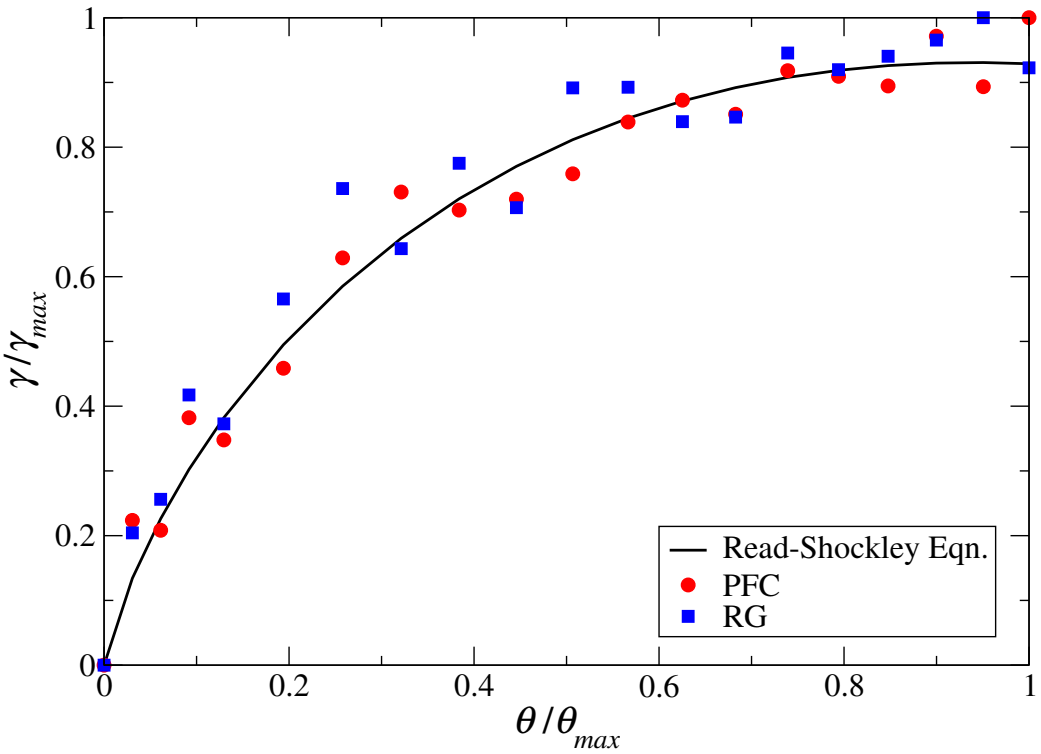

Figure 4.3: (Color online) The PFC model describe the energetics of grain boundary. This graph shows that the grain boundary energy predicted by the PFC model, the amplitude equations and the Read-Shockley theory agree with each other. After Ref. [62].

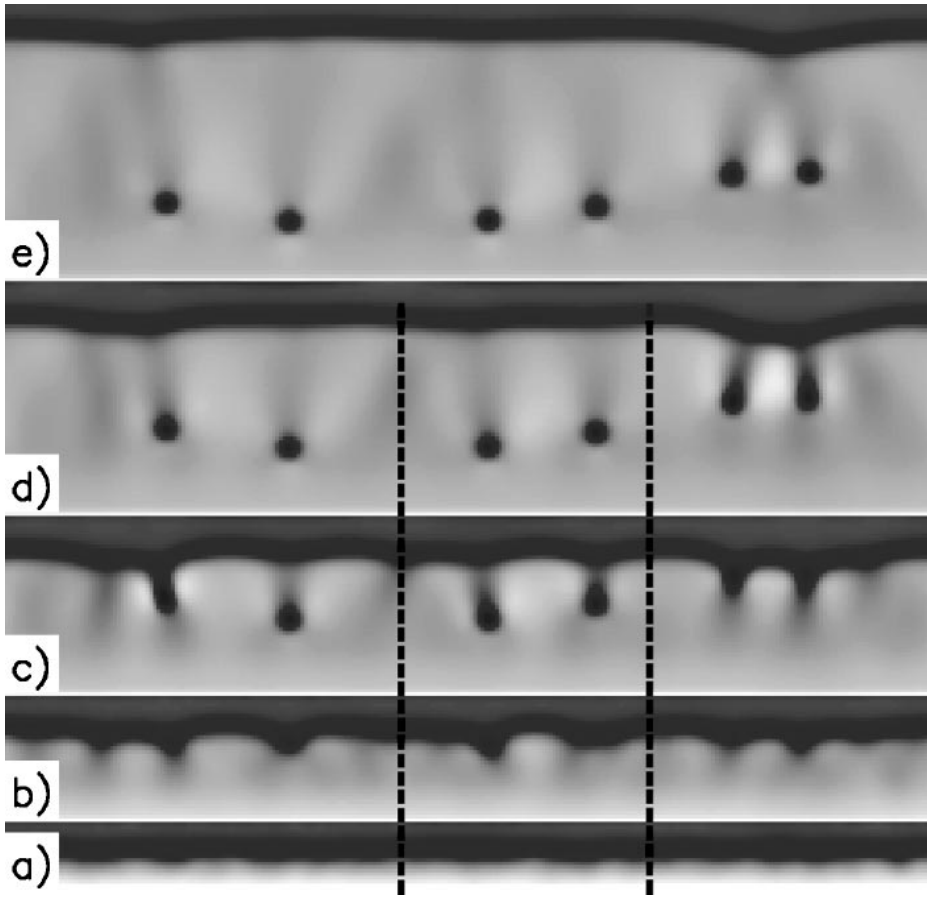

Figure 4.4: Epitaxial growth with the PFC model. The field plotted is the local free energy of the system. The black dots are misfit dislocations. (a), (b), (c), (d), and (e) correspond to times $t = 150$, 300, 450, 600, and 750, respectively. After Ref. [61].

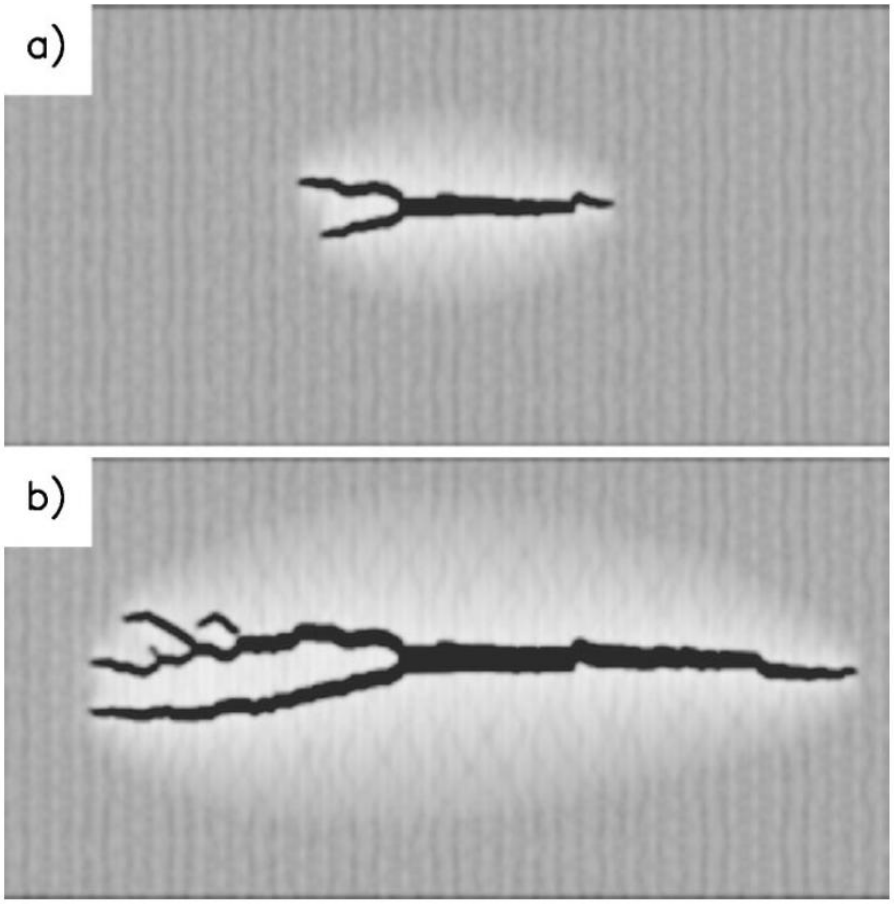

Figure 4.5: Fracture growth with the PFC model. The field plotted is the local free energy of the system. (a) and (b) are at times $t = 25000$ and 65000, respectively. After Ref. [61].

4.3.1 Phase Diagram

Let us first discuss the phase diagram of the PFC model. There are two parameters in the model, namely r and the mean density, ρ_0. The parameter r controls the symmetry breaking of the system; there is only one minimum in the potential energy for $r > 0$, but there are two for $r < 0$. In fact, r is the parameter $t \equiv (T - Tc)/Tc$ in the theory of critical phenomena. For $r > 0$, which corresponds to a high temperature, we expect that there is only the liquid phase; for $r < 0$, however, we expect the translational symmetry to be broken and periodic structures, which make use of the energy benefit from the $1 + \nabla^2$ operator, to emerge. We can quantitatively calculate the phase diagram by using the one-mode approximation[61]. There are three possible ground states for a two dimensional crystal:

1. the uniform (liquid) phase, which can be described by

$$\rho_{liq} = \rho_0, \tag{4.18}$$

2. the stripe phase, which can be described approximately by

$$\rho_{str} = Ae^{i\vec{k}\cdot\vec{x}} + c.c. + \rho_0, \tag{4.19}$$

   where A is the amplitude of the phase and $\vec{k}$ is the reciprocal lattice vector associated with it, and,

3. the triangular phase, which can be described approximately by

$$\rho_{tri} = A\sum_{j=1}^{3} e^{i\vec{k_j}\cdot\vec{x}} + c.c. + \rho_0, \tag{4.20}$$

   where

$$k_1 = k_0\hat{y} \tag{4.21}$$

$$k_2 = \frac{\sqrt{3}}{2}k_0\hat{x} - \frac{1}{2}k_0\hat{y} \tag{4.22}$$

$$k_3 = -\frac{\sqrt{3}}{2}k_0\hat{x} - \frac{1}{2}k_0\hat{y} \tag{4.23}$$

are the three reciprocal lattice vectors and A is the amplitude associated with the mode.

The energy of these ground states can be calculated as follows. We first put the ansatz into the free energy functional, Eq. (4.11), and integrate it over space, then we minimize the resulting free energy with respect to both the amplitudes A and the magnitude of the reciprocal lattice vectors, k_0. The calculation can be found in [61] and it will not be reproduced here. After calculating the energies of various ground states, the phase diagram can be constructed using the Maxwell construction. The phase diagram is shown in Fig. 4.6.

From now on, we focus on the properties of the triangular phase, which serves as a model of a periodic crystal. Different crystal structures can be formed by putting a different nonlinear term in the free energy. It is proposed, for example, that a cubic lattice can be formed by including a term in the free energy proportional to $|\nabla\rho|^4$[61].

4.3.2 Linear Elasticity

We can show that the elastic property of the triangular ground state of the PFC model is consistent with Hooke's law by the following argument: Because there are two parameters in the ansatz of the ground state, namely, the amplitude, A, and the magnitude of the reciprocal lattice vectors, k_0, one can always solve for the A by minimizing the free energy with respect to it, which gives A as a function of k_0, *i.e.,* $A = A(k_0)$. The total free energy, as a result, depends only on k_0, or equivalently on the lattice spacing $a \equiv 2\pi/k_0$. By expanding the free energy in Taylor series about $a = a_0 \equiv 2\pi$, we get

$$F = F_0 + \frac{1}{2}\left.\frac{d^2F}{da^2}\right|_{a=a_0}(a-a_0)^2 + \cdots , \tag{4.24}$$

where F_0 is the ground state energy and the first derivative is zero because the free energy attains its minimum at $a = a_0$. This shows that due the periodicity of the

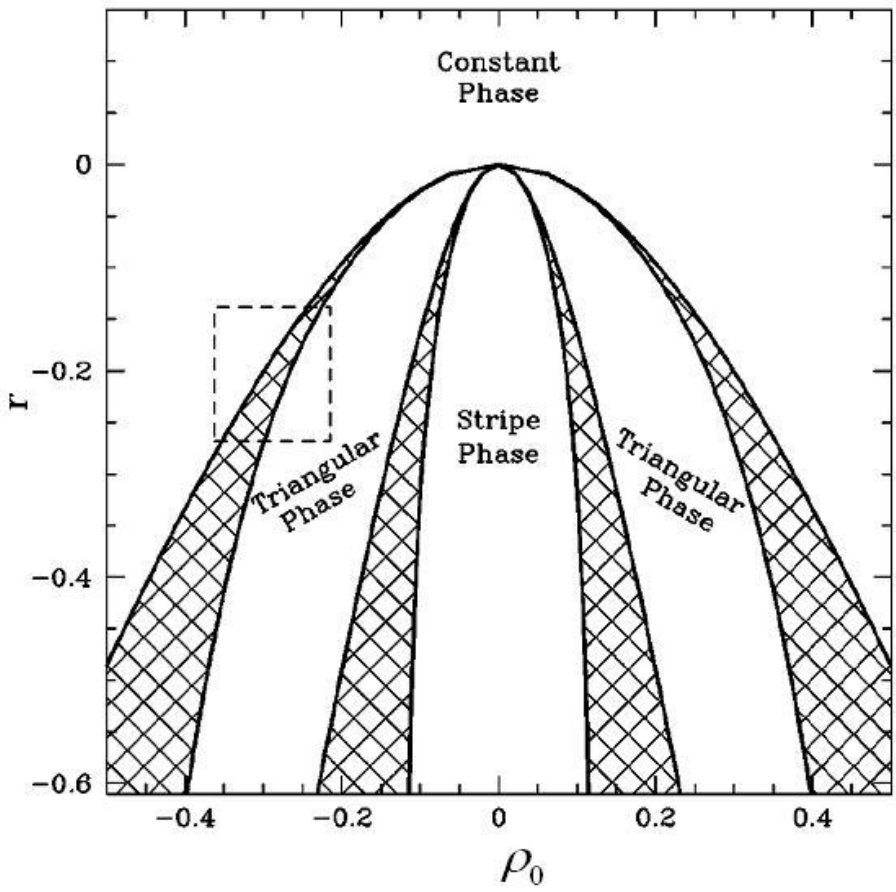

Figure 4.6: The phase diagram of the phase field crystal model, calculated by the one-mode approximation. The hatched sections are the coexistence regions. After Ref. [61].

ground state, Hooke's law is guaranteed. In addition, higher order terms are also captured in this formalism.

This discussion only deal with the elastic energy under bulk stress. Elder *et al.*[61], in addition to this, also calculated the elastic constants of a triangular ground state under shear and deviatoric stresses. They found that the elastic constants, C_{ij}, satisfy the relation $C_{11} = C_{12} + 2C_{44}$, which is consistent with the triangular symmetry of the lattice. This verifies that linear elasticity is correctly incorporated in the PFC model.

Another very important feature of the PFC model is that it captures not only linear elasticity, where a linearized strain tensor is used, but also nonlinear elasticity. We will describe this important point in the next chapter.

4.3.3 Elastic Interactions

The PFC model described by Eq. (4.12) describes only the dissipative dynamics; it captures the long time scale diffusive and solidifying processes. It does not, however, allow any collective atomic oscillations, which are on a much faster time scale. This omission of the elastic interactions in the model prevents us from studying many important aspects, such as the deformation dynamics of nanocrystalline solids[151]. To tackle this problem, Stefanovic *et al.* [151] introduced a modified phase field crystal (MPFC) model that includes both diffusive dynamics and elastic interactions. This is done by adding a second order time derivative to the equation:

$$\frac{\partial^2 \rho}{\partial t} + \beta \frac{\partial \rho}{\partial t} = \alpha^2 \nabla^2 \left(\frac{\delta F}{\delta \rho} \right), \tag{4.25}$$

where α and β are phenomenological constants related to the effective sound speed and vacancy diffusion coefficient. The physical meaning of the addition is straight forward. By writing down a second order partial differential equation, the PFC model is now a damped wave equation, and so it supports two density propagating

solutions. These solutions act as the phonon excitations in the solid, which transmit elastic interactions throughout the medium. As a result, the early time dynamics is governed by the propagative solutions, while the late time dynamics is mainly diffusive.

The relation between the parameters α and β to the effective sound speed and phonon lifetime is presented in Ref. [151].

4.3.4 Renormalization Group Reduction of PFC

The PFC model describes matter at the atomic level, but in order to get a description valid on larger scales, it is necessary to perform some homogenization or renormalization.

Renormalization group (RG) theory is well-known for extracting universal features of statistical mechanical systems near a critical point[1]. About 15 years ago, Goldenfeld and collaborators realized that one could also use RG techniques to extract universal behavior of spatially-extended dynamical systems[1; 155–159]. An early example is a system whose long-time behavior is dominated by a similarity solution (fixed point), $f(x,t) = t^{\alpha} g(xt^{\beta})$. Universality, in this case, corresponds to the fact that a wide class of initial conditions converge to solutions of the same form.

By 1996, the relation between RG, intermediate asymptotics and singular perturbation theory became clear[1; 19]. RG can be regarded as a unified and general way to approach asymptotic problems [19; 20]. It is superior in practice to conventional methods, including multiple scales analysis, boundary layer theory, matched asymptotic expansions and dynamical system reduction[160], in that it is systematic and requires no ad hoc assumption about the perturbation series or coefficient matching. Chen *et al.* showed that the RG equations are actually the amplitude equations in pattern forming systems[20]. This is where RG meets the PFC model.

The idea can be illustrated by considering a perfectly periodic field. There are two

ways to describe this field. We can describe the field by a continuous rapidly-varying function, *e.g.,* $\Phi(\vec{x}) = A\exp(i\vec{k}\cdot\vec{x} + i\phi)$, or, for a specific band of k, we can focus on the slowly-varying real amplitude A and its phase ϕ. Generally we consider A to be a complex number, and ϕ to be its phase. For a multicrystalline crystal, although the field is not periodic globally, it is almost perfectly periodic within each domain, so one can specify the system by slowly varying the complex amplitude $A(\vec{x}, t)$. The slow variation in $A(\vec{x}, t)$ reflects the imperfection of periodicity in the configuration. RG then allows one to write down differential equations for the slowly varying field A rather than one rapidly varying field Φ. The partial differential equations governing A are sometimes called the renormalization group equations[20] or the amplitude equations[161].

For example, for the two-dimensional PFC model, the triangular phase solution is represented by,

$$\rho(\vec{x}) = \sum_{j=1}^{3}\left(A_j(\vec{x}, t)e^{i\vec{k}_j\cdot\vec{x}} + c.c.\right) + \bar{\rho} \tag{4.26}$$

where A_j are the complex amplitude functions. This is a generalization of the triangular ground state given by Eq. (4.20), where the constant amplitude A is promoted to 3 slowly varying amplitudes $A_j(\vec{x}, t)$. After doing the RG calculation from Eq. (4.12), the amplitude equations are[12; 13; 62]

$$\frac{dA_1}{dt} = (1 - L_1)(\Gamma - L_1^2) - 3A_1(|A_1|^2 + 2|A_2|^2 + 2|A_3|^2) - 6\rho_0 A_2^* A_3^* + \cdots \tag{4.27}$$

$$\frac{dA_2}{dt} = (1 - L_2)(\Gamma - L_2^2) - 3A_2(2|A_1|^2 + |A_2|^2 + 2|A_3|^2) - 6\rho_0 A_1^* A_3^* + \cdots \tag{4.28}$$

$$\frac{dA_3}{dt} = (1 - L_3)(\Gamma - L_3^2) - 3A_3(2|A_1|^2 + 2|A_2|^2 + |A_3|^2) - 6\rho_0 A_2^* A_1^* + \cdots \tag{4.29}$$

where $\Gamma \equiv -r - 3\rho_0^2$ and $L_j \equiv \nabla^2 + 2i\vec{k_j}\cdot\nabla$ is a manifestly rotationally covariant operator. Nonlinear gradient terms are not shown in the above equations. Eq. (4.27)-(4.29) are the amplitude equations for the PFC model. By solving the amplitude equations, one obtains the same dynamics as solving the original PFC equation (4.12), as verified in Ref. [12].

This provides us with a theory purely in terms of the amplitudes. There are at least two applications of this picture. First, we can reformulate the theory merely in terms of the amplitudes. In the next chapter we will see that the correct form of the elasticity, both linear and nonlinear, is preserved in the amplitude picture, and we will find that the amplitudes is a natural bridge between the microscopic PFC theory and the macroscopic elasticity theory. Second, since the amplitude varies slowly over the atomic scales, a coarser mesh can be used when the equations are solved numerically. This allows the model to be solved numerically using computationally efficient approaches, to which we now turn.

4.3.5 Adaptive Mesh Refinement

Despite the long (diffusive) time scale offered by the PFC model, including a realistically large number of atoms in a simulation to predict behavior of macroscopic samples will necessarily require huge simulation times. How can we resolve every PFC atom, and at the same time simulate a large system? The RG equations, Eq. (4.27) - (4.29), provide a solution to this problem.

Given that the amplitude A_j only changes rapidly near defects, and is slowly varying in most part of the system, it is most efficient to solve Eq. (4.27) - (4.29) using an adaptive mesh that is coarser when A is slowly varying and finer when A changes rapidly. This saves computational resources by focusing the computation only near defects (Fig. 4.7- 4.8). This technique of adaptive meshing has been shown to be successful in the problem of dendritic growth using phase field model[162–164]. Instead of scaling as the volume(L^d) of the system, the computational time needed for the adaptive mesh algorithm scales as the arc length of the dendrite, which scales as L^{d-1}. Athreya *et al.*[62] applied this method to solve the RG equations for the PFC model and found that this method is 1000 times faster than solving the PFC equation on a uniform mesh (Fig. 4.9). The details of the derivation and the implementation

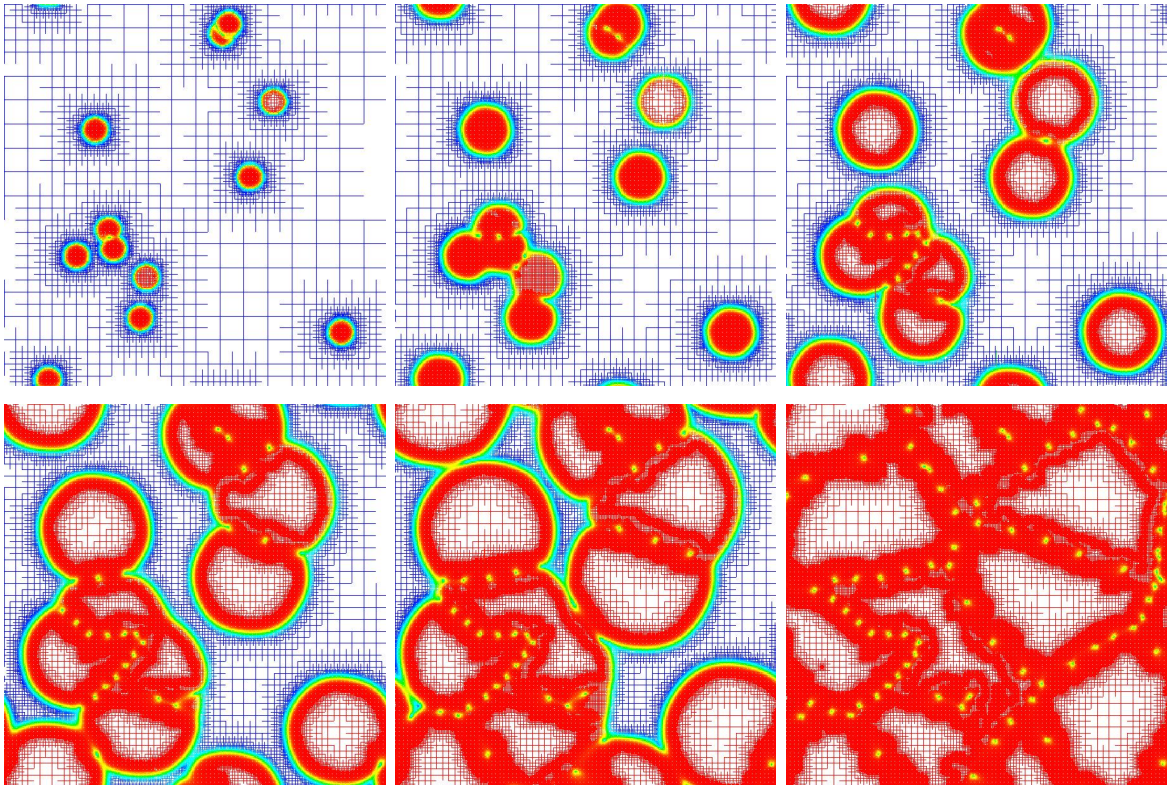

Figure 4.7: Time evolution of the complex amplitudes, A_j, solved by the technique of adaptive mesh refinement. Coarser meshes is used within each domain, and finer meshes is used near defects and grain boundaries. The mesh is updated dynamically, depending on the local gradient of A_j.

of the adaptive mesh refinement can be found in Ref. [62].

4.4 Conclusion

The use of phase field modeling allows us to understand systems with multiple material phases, but it does not contain information about the elasticity and crystallography of the material. A natural way to improve this is to put those features directly into the phase field. This leads to the development of the phase field crystal (PFC) model.

The PFC model represents the desired elastic and crystallographic properties of materials. The model is capable of describing polycrystalline solidification, dislocation interactions, grain coarsening, epitaxial growth, diffusion, fracture and many other

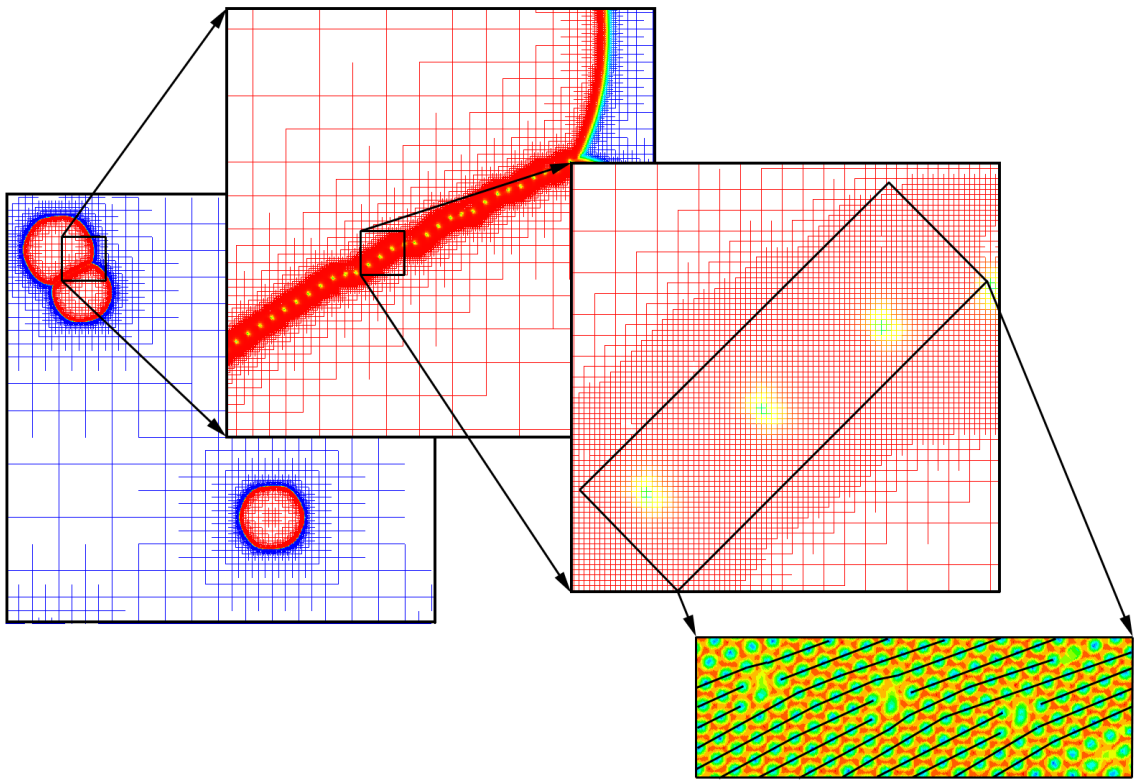

Figure 4.8: This figure shows explicitly that the mesh gets finer only near defects. This allows us to spend our computational power on the dynamics of the defects, but not on the almost static interiors of the domains.

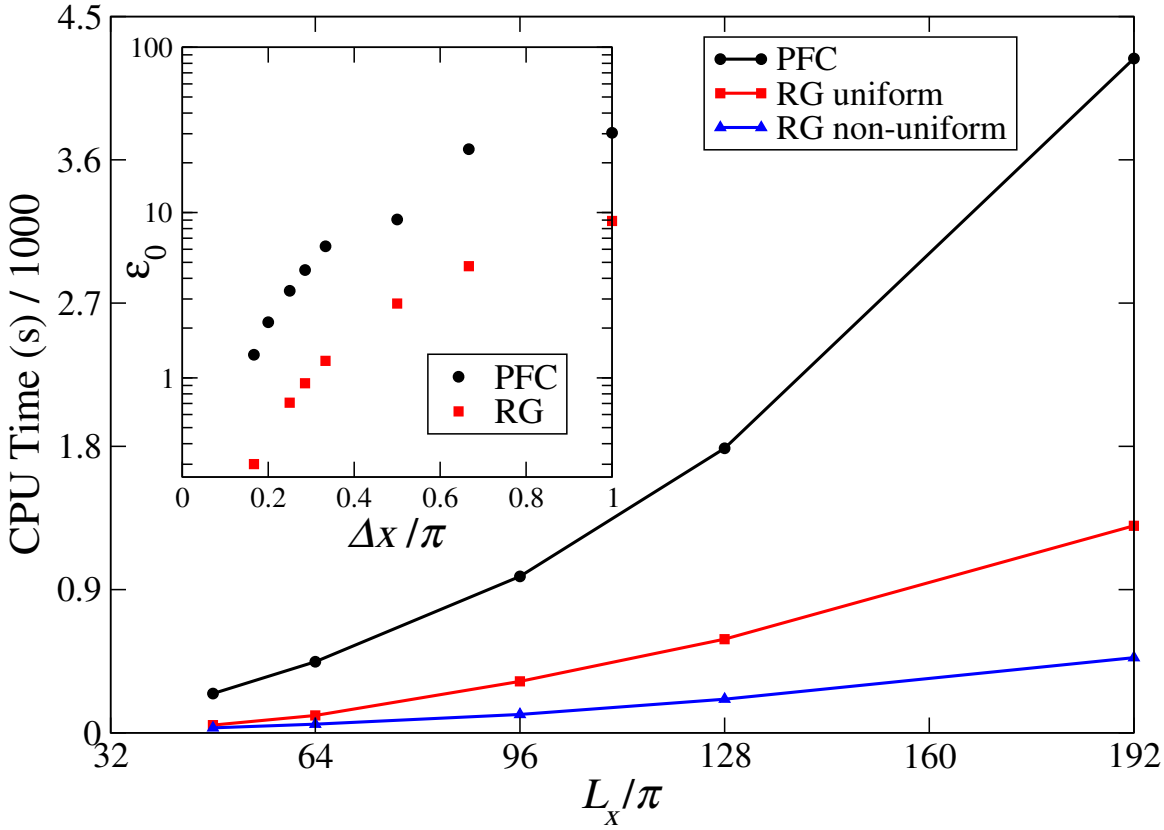

Figure 4.9: Comparison of computational times by 1. solving the PFC equation on a uniform mesh, 2. solving the RG equation on a uniform mesh, and 3. solving the RG equation on a non-uniform mesh.

fundamental phenomena. The application of the Renormalization Group technique and adaptive mesh refinement to the model opens up the possibility of numerically simulating macroscopically large systems on atomic length scales and diffusive time scales.

In the following chapters, we are going to show that the PFC model contains the correct form of nonlinear elasticity and also plasticity. We also modify the model to accommodate vacancies and extend the model to binary alloys.

Chapter 5

Nonlinear Elasticity

In the preceding chapter, we saw that the PFC model is a minimal model that coarsens the microscopic dynamics of a crystal but retains its crystallographic and elastic properties. We saw that the model can describe a variety of phenomena, including multicrystalline solidification[61], elasticity[60; 61; 151], defect dynamics[61; 150; 152], epitaxial growth, as well as crack and fracture dynamics[61]. Goldenfeld *et al.* then applied the technique of Renormalization Group to the model and derived the complex amplitude representation[12; 13], which is a coarsened version of the PFC model, in which all the atomic structures are smeared out and the only structures left are the crystal defects, such as dislocations and grain boundaries. By applying the technique of adaptive mesh refinement, this representation is about 1000 times faster computationally than molecular dynamics[62].

In this chapter, we show that an additional level of coarse-graining can be performed on the complex amplitude representation. The result is a theory of nonlinear elasticity valid at system-wide or macroscopic scales. We also derive the strain energy of the system—the free energy as a function of the strain tensor.

This result is significant. First, it shows that the PFC model and the complex amplitude representation describe not only linear, but also nonlinear elasticity; this extends the result of Elder *et al.*[61], where they derived the elastic property of the PFC

model. Second, instead of postulating a form for the strain energy based on symmetry and phenomenology, which is what is usually done in continuum mechanics[165; 166], we derive it from a more microscopic model—the PFC model. This provides a theoretical connection to microscopic structures and opens up the possibility of deriving other forms of strain energy by similar approaches. Third, by going from the PFC model to the complex amplitude representation to the strain energy formulation, we are going from microscopic, to mesoscopic, to macroscopic scales and we are capturing multicrystalline structures, defect dynamics, as well as nonlinear elastic effects. In other words, we have a multiple scale approach to materials properties, accessing the realm of continuum mechanics from a density functional theory at atomic scales.

In the following, we first introduce the PFC model and the complex amplitude representation, then we derive the free energy in that representation. The strain energy is then derived. In the process, we also explain a quick way to obtain the Renormalization Group, or amplitude, equations of motion.

5.1 The Model

The phase field crystal (PFC) model is defined by the free energy density[60; 61],

$$f = \frac{\rho}{2}(1+\nabla^2)^2\rho + \frac{r}{2}\rho^2 + \rho^4, \tag{5.1}$$

where $\rho(\vec{x},t)$ is the phase field, or the order parameter. The dynamics is conservative and dissipative, given by

$$\frac{\partial\rho}{\partial t} = \nabla^2\left(\frac{\delta F}{\delta\rho}\right) \tag{5.2}$$

where $F = \int d^2x f(x)$ is the total free energy of the system. Thermal noise is ignored in our discussion here, but could be included if desired. Generally, it will not be important at system scales. There are three phases in this model, namely uniform, stripe and triangular. The ground state in the triangular phase can be written in the

single-mode approximation by

$$\rho_{tri}(\vec{x}) = A\sum_{j=1}^{3}\left(e^{i\vec{k}_j\cdot\vec{x}} + e^{-i\vec{k}_j\cdot\vec{x}}\right) + \rho_0, \tag{5.3}$$

where ρ_0 is the average density, A is the constant amplitude and

$$\vec{k}_1 = \hat{y}, \quad \vec{k}_2 = \frac{\sqrt{3}}{2}\hat{x} - \frac{1}{2}\hat{y}, \quad \vec{k}_3 = \frac{-\sqrt{3}}{2}\hat{x} - \frac{1}{2}\hat{y} \tag{5.4}$$

are the three lattice vectors. Goldenfeld *et al.* showed[12; 13] that instead of using $\rho(\vec{x},t)$ as the dynamical variable, it is more efficient to generalize Eq. (5.3) and promote the constant amplitudes A to 3 slowly varying complex amplitudes $A_j(\vec{x},t)$ and treat the $A_j(\vec{x},t)$ as dynamical variables. By applying the technique of Renormalization Group, they showed that the dynamical equation for $A_1(x,t)$ is given by[12; 13]

$$\begin{aligned}\frac{\partial A_1}{\partial t} &= (1-L_1)(\Gamma - L_1^2)A_1 - 6\rho_0 A_2^* A_3^* \\ &\quad -3A_1(|A_1|^2 + 2|A_2|^2 + 2|A_3|^2) + \cdots,\end{aligned} \tag{5.5}$$

where $\Gamma \equiv -r - 3\rho_0^2$ and $L_1 \equiv \nabla^2 + 2i\vec{k}_1\cdot\nabla$ is a rotationally covariant operator. Nonlinear gradient terms[13] are not written out explicitly. Amplitude equations for $A_{2,3}(x,t)$ can be written down by doing the appropriate permutations. This is the complex amplitude representation.

5.2 Derivation of the Amplitude Equations without using Renormalization Group

The first attempt to derive the free energy in this representation is to note that Eq. (5.5), ignoring the nonlinear gradient terms, can be written as

$$\frac{\partial A_j}{\partial t} = -\frac{\delta F_{dyn}[A_j(x,t)]}{\delta A_j^*}, \tag{5.6}$$

where the free energy F_{dyn} is given by the free energy density

$$\begin{aligned} f_{dyn} &= -\sum_{j=1}^{3} A_j^*(1-L_j)(\Gamma - L_j^2)A_j + 3\sum_{j,k=1}^{3}|A_j|^2|A_k|^2 \\ &\quad -\frac{3}{2}\sum_{j=1}^{3}|A_j|^4 + 6\rho_0(A_1A_2A_3 + A_1^*A_2^*A_3^*). \end{aligned} \tag{5.7}$$

At first glance, this seems sensible and correct. We, however, observe that the dynamics given by Eq. (5.6) is purely dissipative, as oppose to the density-conserving dynamics in the original PFC equation, Eq. (5.2). This is alarming. In fact, we observe that the coefficient of the highest order gradient operator, ∇^6, is negative, which would destabilize the dynamics on small scales.

To resolve this conundrum, we note that Eq. (5.7) is derived from the dynamical equations of A_j, which in turn, are derived from the PFC equation, Eq. (5.2), the density-conserving information in the original PFC equation is propagated to the free energy, Eq. (5.7). However, density conservation should only be exhibited in the dynamical equation of motion and not be represented in the equilibrium free energy. This can be seen in the original equations: density conservation appears only in the dynamical equation, Eq. (5.2), but not in the free energy, Eq. (5.1).

Thus, the correct way to derive the free energy in the complex amplitude representation is to derive it from the original PFC free energy, Eq. (5.1). The easiest way to do that is to substitute the ansatz, Eq. (5.3), into the free energy, Eq. (5.1). The first term of Eq. (5.1) can then be computed by using the identity

$$(1+\nabla^2)\rho = \sum_{j=1}^{3}\left(e^{i\vec{k}_j\cdot\vec{x}}L_jA_j + c.c.\right) + \rho_0, \tag{5.8}$$

where *c.c.* stands for complex conjugate. By performing an integration by parts, we find

$$\frac{\rho}{2}(1+\nabla^2)^2\rho = \frac{1}{2}[(1+\nabla^2)\rho]^2 \tag{5.9}$$

$$= \sum_{j=1}^{3} A_j^*L_j^2A_j, \tag{5.10}$$

where in the last line constants and terms with the rapidly oscillating factor $\exp(i\vec{k}_j \cdot \vec{x})$ are neglected. We can neglect the oscillating terms because the complex amplitudes, A_j, are slowly varying on that scale, so the terms cancel themselves upon integration over space. Other terms in the free energy can be transformed in a similar fashion. The resulting free energy is given by

$$\begin{aligned} f_{amp} &= -\sum_{j=1}^{3} A_j^*(\Gamma - L_j^2)A_j + 3\sum_{j,l=1}^{3} |A_j|^2|A_l|^2 \\ &\quad -\frac{3}{2}\sum_{j=1}^{3} |A_j|^4 + 6\rho_0(A_1A_2A_3 + A_1^*A_2^*A_3^*). \end{aligned} \tag{5.11}$$

Note that this free energy is different from Eq. (5.7). The $1 - L_j$ operator in the first term in Eq. (5.7) is absent here. This is to be expected because this operator arises from the conservative Laplacian in the dynamical equation, and according to our discussion above, it should not appear in the free energy. The transformation of the dynamical equation, Eq. (5.2), into the complex amplitude representation can be performed by observing that for any function, $f(x)$, the identity,

$$\int_{-\infty}^{\infty} d^2x[(L_j - 1)f(x)]e^{i\vec{k}_j\cdot\vec{x}} \equiv 0, \tag{5.12}$$

holds. This resembles the identity,

$$\int_{-\infty}^{\infty} d^2x\nabla^2 g(x) = 0, \tag{5.13}$$

for any function $g(x)$. In fact, if we define $g(x) = f(x)e^{i\vec{k}_j\cdot\vec{x}}$, Eq. (5.13) implies Eq. (5.12). This shows that when we make the change of variables from the density, ρ, to the complex amplitudes, A_j, the Laplacian in the conservative dynamical equation has also to be transformed to $L_j - 1$. We thus arrive at the equation of motion

$$\frac{dA_j}{dt} = (L_j - 1)\frac{\delta F_{amp}}{\delta A_j^*}, \tag{5.14}$$

which, when written out explicitly, is,

$$\begin{aligned} \frac{dA_1}{dt} &= (1 - L_1)\big[(\Gamma - L_1^2)A_1 - 6\rho_0 A_2^*A_3^*, \\ &\quad -3A_1(|A_1|^2 + 2|A_2|^2 + 2|A_3|^2)\big] \end{aligned} \tag{5.15}$$

with appropriate permutations for $A_{2,3}(x,t)$. By construction, these equations conserve the density of the system.

Upon comparison, Eq. (5.15) is exactly the same as Eq. (5.5) with all the nonlinear gradient terms included. Our derivation shows that the inclusion of the nonlinear gradient terms is crucial for density conservation, and shows that all those terms can actually be written in the condensed form of Eq. (5.15). Note, however, that our derivation does not use any renormalization group argument, but follows from the integral identity, Eq. (5.12). Of course, we did make a coarse-graining assumption after Eq. (5.10), where we naively asserted that the rapid oscillation averages to zero.

With this correct free energy in the complex amplitude representation, we can now proceed and derive the nonlinear elastic properties of the model.

5.3 Nonlinear Elasticity

The goal of this section is to derive the free energy as a function of the strain tensor, when the PFC crystal is deformed under a general deformation

$$x'_m = F_{mn} x_n, \tag{5.16}$$

where F_{mn} is the deformation gradient. Einstein's summation convention is used throughout, except for the index j in $\vec{k}_j$, A_j and L_j. In general, the deformation gradient can be written as[166]

$$F_{mn} = R_{mp} U_{pn} \tag{5.17}$$

where R_{mp} is a pure rotation matrix and U_{pn} is a positive-definite, pure deformation matrix. Since our system is rotationally covariant, we expect that the free energy should only depend on the function $U^T U$, where U^T is the transpose of the matrix U.

Under the deformation, Eq. (5.16), the complex amplitudes transform as

$$A_j \to A'_j = Ae^{ik_{jm}D_{mn}x_n}, \tag{5.18}$$

where we defined $D_{mn} \equiv R_{mk}U_{kn} - \delta_{mn}$ and assumed that $|A_j| = A$ for all j, where A is a constant. k_{jm} is the m-th component of the vector $\vec{k}_j$. Because the deformation gradient only enter the complex amplitude through its phase, the only relevant terms in the free energy are the gradient terms given by

$$E \equiv \sum_{j=1}^{3} A_j^* L_j^2 A_j. \tag{5.19}$$

Other terms in the free energy, Eq. (5.11), only contribute when we minimize the free energy with respect to A at the end of the calculation. By using Eq. (5.18) and differentiating, we obtain

$$L_j A_j = (-k_{jm}k_{jn}R_{mp}R_{na}U_{pq}U_{aq} + 1)A_j. \tag{5.20}$$

Apply L_j again and substitute the result into Eq. (5.19) to obtain

$$E = A^2(E_1 - 2E_2 + 3), \tag{5.21}$$

where

$$E_1 = \left(\sum_{j=1}^{3} k_{jm}k_{jn}k_{ju}k_{jv}\right) F_{mq}F_{nq}F_{uw}F_{vw}, \tag{5.22}$$

and,

$$E_2 = \left(\sum_{j=1}^{3} k_{jm}k_{jn}\right) F_{mq}F_{nq}. \tag{5.23}$$

The rest of the derivation concerns the evaluation of E_1 and E_2. We first evaluate E_2. By using the definition of $\vec{k}_j$ from Eq. (5.4), we obtain

$$k_{1m}k_{1n} = \delta_{my}\delta_{ny} = \delta_{mn}\delta_{my}, \tag{5.24}$$

$$k_{2m}k_{2n} = \frac{3}{4}\delta_{mx}\delta_{nx} + \frac{1}{4}\delta_{my} - \frac{\sqrt{3}}{4}(\delta_{mx}\delta_{ny} + \delta_{nx} + \delta_{my}), \tag{5.25}$$

and,

$$k_{3m}k_{3n} = \frac{3}{4}\delta_{mx}\delta_{nx} + \frac{1}{4}\delta_{my} + \frac{\sqrt{3}}{4}(\delta_{mx}\delta_{ny} + \delta_{nx} + \delta_{my}). \tag{5.26}$$

Combining these three equations we have

$$\sum_{j=1}^{3} k_{jm}k_{jn} = \frac{3}{2}\delta_{mn}(\delta_{mx} + \delta_{my}) = \frac{3}{2}\delta_{mn}. \tag{5.27}$$

Thus, E_2 is given by

$$E_2 = \frac{3}{2}F_{pq}F_{pq} = \frac{3}{2}U_{pq}U_{pq} = \frac{3}{2}\mathtt{Tr}[U^T U], \tag{5.28}$$

where we used the property of the rotation matrix, that $R_{im}R_{jm} = R_{mi}R_{mj} = \delta_{ij}$, $\mathtt{Tr}[A]$ and A^T are the trace and transpose of the matrix A respectively. The evaluation of E_1 is more involved. We note that

$$k_{1m}k_{1n}k_{1u}k_{1v} = \delta_{mn}\delta_{nu}\delta_{uv}\delta_{my}, \tag{5.29}$$

and observe that the term

$$k_{2m}k_{2n}k_{2u}k_{2v} + k_{3m}k_{3n}k_{3u}k_{3v} \tag{5.30}$$

is equal to the term

$$2 \times [k_{2m}k_{2n}k_{2u}k_{2v} \ \mathtt{terms\ with\ positive\ coefficients}]. \tag{5.31}$$

By exploring this relation and using the definition of $\vec{k}_j$, Eq. (5.4), we obtain

$$\begin{aligned}\sum_{j=1}^{3} k_{jm}k_{jn}k_{ju}k_{jv} &= \frac{3}{8}(\Delta_{xxyy} + \Delta_{yyxx} + \Delta_{xyxy}) \\ &\quad + \frac{3}{8}(\Delta_{xyyx} + \Delta_{yxxy} + \Delta_{yxyx}) \\ &\quad + \frac{9}{8}(\Delta_{xxxx} + \Delta_{yyyy}),\end{aligned} \tag{5.32}$$

where we defined $\Delta_{abcd} \equiv \delta_{ma}\delta_{nb}\delta_{uc}\delta_{vd}$ for convenience. By this, we have

$$\begin{aligned}
&\left(\sum_{j=1}^{3} k_{jm}k_{jn}k_{ju}k_{jv}\right) R_{mp}R_{na}R_{us}R_{vt} \\
= \;& \frac{3}{8}[R_{xp}R_{xa}R_{ys}R_{yt} + R_{yp}R_{ya}R_{xs}R_{xt}] \\
&+\frac{3}{8}[R_{xp}R_{ya}R_{xs}R_{yt} + R_{yp}R_{xa}R_{ys}R_{xt}] \\
&+\frac{3}{8}[R_{xp}R_{ya}R_{ys}R_{xt} + R_{yp}R_{xa}R_{xs}R_{yt}] \\
&+\frac{9}{8}[R_{xp}R_{xa}R_{xs}R_{xt} + R_{yp}R_{ya}R_{ys}R_{yt}] \qquad (5.33)
\end{aligned}$$

To evaluate this expression, we note that we can combine terms appropriately. For example, by using the property of the rotation matrix, we obtain

$$R_{xp}R_{xa}R_{ys}R_{yt} + R_{xp}R_{xa}R_{xs}R_{xt} = R_{xp}R_{xa}\delta_{st}, \qquad (5.34)$$

and,

$$R_{yp}R_{ya}R_{xs}R_{xt} + R_{yp}R_{ya}R_{ys}R_{yt} = R_{yp}R_{ya}\delta_{st}. \qquad (5.35)$$

The sum of Eq. (5.34) and (5.35) then give

$$\begin{aligned}
&R_{xp}R_{xa}R_{ys}R_{yt} + R_{xp}R_{xa}R_{xs}R_{xt} \\
&+R_{yp}R_{ya}R_{xs}R_{xt} + R_{yp}R_{ya}R_{ys}R_{yt} = \delta_{st}\delta_{ap} \qquad (5.36)
\end{aligned}$$

Repeating this for all the terms in Eq. (5.33), we obtain

$$\begin{aligned}
&\left(\sum_{j=1}^{3} k_{jm}k_{jn}k_{ju}k_{jv}\right) R_{mp}R_{na}R_{us}R_{vt} \\
= \;& \frac{3}{8}[\delta_{ap}\delta_{st} + \delta_{sp}\delta_{at} + \delta_{as}\delta_{pt}]. \qquad (5.37)
\end{aligned}$$

Substituting into into Eq. (5.22), and then into Eq. (5.21), we obtain

$$E = 3A^2\Delta, \qquad (5.38)$$

where

$$\Delta = \frac{1}{8}\left\{[\mathtt{Tr}(U^TU)]^2 + 2\mathtt{Tr}(U^TUU^TU)\right\} - \mathtt{Tr}(U^TU) + 1. \qquad (5.39)$$

By using the relation

$$U^T_{mp}U_{pn} = \delta_{mn} + 2u_{mn}, \tag{5.40}$$

where $u_{ij} \equiv (\partial_i u_j + \partial_j u_i + (\partial_k u_i)(\partial_k u_j))/2$ is the strain tensor, we obtain

$$\Delta = \left(\frac{3}{2}u^2_{xx} + \frac{3}{2}u^2_{yy} + u^2_{xy} + u^2_{yx} + u_{xx}u_{yy}\right). \tag{5.41}$$

.

Finally, we put this back into the free energy, Eq. (5.11), and minimize the whole expression with respect to A to obtain

$$A(\Delta) = \frac{1}{5}\left(-\rho \pm \frac{1}{3}\sqrt{9\rho^2 + 15(\Gamma - \Delta)}\right), \tag{5.42}$$

which gives the free energy density as

$$f(\Delta) = \frac{45}{2}A^4(\Delta) + 12\rho_0 A^3(\Delta) - 3(\Gamma - \Delta)A^2(\Delta). \tag{5.43}$$

This formula completely defines the elastic properties of the PFC model, and provides a starting point for conventional continuum mechanical applications of nonlinear elasticity theory.

By expanding the free energy around the ground state, we can write

$$f - f_0 = 3A_0^2\Delta + \frac{3\rho_0 A_0 - \Gamma}{6\rho_0^2 + 10\Gamma}\Delta^2 + O(\Delta^3), \tag{5.44}$$

where f_0 is the ground state energy and the first order term of this equation is the usual elastic energy of an isotropic medium.

To summarize, we have shown how the phase variation in the Renormalization Group equation of the PFC model yields a complete derivation of nonlinear elasticity, one whose parameters can be related to microscopic parameters present in the original PFC equation.

Chapter 6

Plasticity

In the last chapter, we showed that the phase field crystal (PFC) model captures the correct form of nonlinear elasticity. In this chapter, we study the plastic properties of the model by examining its response under external shearing. We observed dislocation creation, annihilation and avalanches. We found that the resulting avalanche statistics resembles that of the externally driven random field Ising model and other dislocation avalanching systems, which can be described by a non-equilibrium critical point. By scaling the avalanche distributions of different shearing rates, we obtained a data collapse and extracted from it the critical exponents.

6.1 Introduction

Materials yield and deform plastically under large external stress. While the yield surface and the plastic flow have been two important topics in material science, and are well described by various continuum theories[167–169], what happens microscopically during a plastic deformation is still not fully understood. On atomic scales, external stress is not carried uniformly by a smooth deformation of the crystal structure, but is carried by localized crystal defects, such as dislocations and disclinations. Under stress, crystal defects are created and they interact with each other. Al-

though the properties of individual defects and the interaction between them are well known[47; 170–172], their collective behavior under external stress is complicated and often gives rise to scale invariant, power-law distributed, phenomena[66; 67; 173–177], in strong resemblance to the scaling behavior near a critical point.

One prime example of such a non-equilibrium critical point can be found in the random field Ising model (RFIM)[17; 63; 64; 178; 179]. As the external magnetic field oscillates between a large negative and a large positive values, the magnetization of the Ising ferromagnet oscillates accordingly. Hysteresis loops are then formed due to the energy barrier of flipping clusters of spins. While these loops are smooth on macroscopic scales, they are actually composed of many small steps, each of which corresponds to flipping of a localized ferromagnetic cluster. The distribution of sizes of such steps depends on the amount of disorder in the system. Dahmen and Sethna showed that there is a non-equilibrium critical point around which the system exhibits universal scaling behavior. By properly scaling the event size distributions, with an event being the flipping of a ferromagnetic cluster, the distributions of different amounts of disorder can be collapsed onto a single curve—a fingerprint of critical phenomena. They also calculated the critical exponents by an epsilon expansion and compared them with numerical studies[63].

The hysteresis loops, which can be thought of as 'yielding' of magnetization under external magnetic field, are analogous to the yielding of a crystal under external stress. Under external stress, the crystal creates many dislocations, which move and interact with each other, creating dislocation avalanches of various sizes. In the light of this analogy, there might be a similar nonequilibrium critical point in plastic flow. The goal of this chapter is to study this critical point, by applying the knowledge and techniques from the scaling of the RFIM.

There is currently a great interest in the existence of a non-equilibrium critical point in plastic flow and its scaling behavior. Weiss *et al.* have measured the acoustic

emission signal from creep deformation experiments on single crystal ice and found that the event size distribution follows a power law over 4 decades[173; 174]. Miguel *et al.* have conducted dislocation dynamics simulations in two dimensions and found that the event size distribution also follows a power law, with a rate-dependent cutoff, over approximately 2 decades[67]. In addition, Zapperi *et al.* have discovered a data collapse of the event size distribution with different external stresses[66]. A review on the subject can be found in Ref. [66; 173].

In this chapter, we study dislocation avalanches during plastic flows using the phase field crystal (PFC) model[60; 61], which has been shown to capture the correct form of nonlinear elasticity and dislocation interactions. We begin by adding an advective term to the model as a shearing force. By adjusting the shearing force and measuring the resulting avalanche statistics, a data collapse is obtained, in analogy to the dynamics of RFIM. This is a strong indication of the presence of a non-equilibrium critical point in the system. We also extracted the critical exponents and the scaling function from the collapse.

6.2 The Model

We recall that the phase field crystal (PFC) model is given by the free energy density[60; 61]

$$f = \frac{\rho}{2}(\nabla^2 + 1)^2\rho + \frac{r}{2}\rho^2 + \frac{\rho^4}{4}, \tag{6.1}$$

where r is the undercooling and $\rho(\vec{x}, t)$ is the order parameter. The dynamics associated with this free energy is conservative, relaxational and diffusive. Because we would like to study the plastic response of the PFC model under shearing, we add a shearing term to the dynamical equation, resulting in

$$\frac{\partial^2\rho}{\partial t^2} + \beta\frac{\partial\rho}{\partial t} = \alpha^2\nabla^2\frac{\delta F}{\delta\rho} + v(y)\frac{\partial\rho}{\partial x} + \eta, \tag{6.2}$$

where

$$v(y) = \begin{cases} v_0 e^{-y/\lambda} & \text{for} \quad 0 < y < L_y/2 \\ -v_0 e^{-(L_y - y)/\lambda} & \text{for} \quad L_y/2 < y < L_y \end{cases} \tag{6.3}$$

is the shearing profile with v_0 being the magnitude of the shearing, λ is the penetration depth, α and β controls the range and time scale of elastic interactions (phonon excitations) propagating through the medium[151], $F \equiv \int f(\vec{x}) d^d x$ is the total free energy and η is the thermal noise satisfying the fluctuation-dissipation theorems

$$\langle \eta(\vec{x}, t) \eta(\vec{x}', t') \rangle = -\epsilon \nabla^2 \delta(\vec{x} - \vec{x}') \delta(t - t'), \tag{6.4}$$

with ϵ being the noise amplitude, which is directly proportional to the temperature, $k_B T$. The value of v_0 controls the magnitude of the shearing force, the penetration depth, λ, controls how deep the shearing force goes into the material. In all of our simulations, we set $\lambda \ll L_y$, so the actual value of λ does not affect our simulation results.

One of the advantages of using the PFC model to simulate dislocation avalanches is that we do not have to impose any ad hoc assumptions about the creation and annihilation of dislocations. Recall that in dislocation dynamics simulations, dislocations are treated as elementary particles and usually only the far field interaction between dislocations is captured. When dislocations get too close to each other (a few atomic spacings), the highly nonlinear interaction between them is not captured and more importantly, the annihilation of dislocations is not accounted for. The standard practice is then to impose some annihilation rules for dislocations—dislocations of opposite topological charges will be destroyed together when they get too close to each other[67]. The same is true for creation of dislocations, dislocations have to be created by hand when the local strain is high. Although these rules are consistent with our physical intuition, particular ways of implementing them are sometimes difficult to justify. However, because the model captures the nonlinear elastic behavior of a crystal, the interaction between dislocations is completely captured. In addition,

because the PFC model simulates the atoms in the lattice, but not the dislocations themselves, creation and annihilation of them are also naturally captured as collective excitations of the lattice. No *ad hoc* rules or assumptions have to be imposed.

We solved Eq. (6.2) in a 2D rectangular domain. The crystal under shear is initially perfectly triangular. As the crystal is sheared, dislocations are created near the boundaries and propagate into the bulk. They interact with each other and form various kinds of avalanches. To quantify the avalanche activity, we calculate the total speed of all dislocations in the domain,

$$\tilde{V}(t) = \sum_{i=1}^{N_{dis}(t)} |\vec{u}_i|, \tag{6.5}$$

where $N_{dis}(t)$ is the number of dislocations in the system at time t and $\vec{u}_i$ is the velocity of the i-th dislocation. This is intended to be a measure similar to the acoustic emission signal in Weiss *et al.*'s single crystal ice experiments. As dislocations are generated and interact with each other in the domain, in additional to the fast avalanching dynamics, quasi-static structures, such as grain boundaries, can form. These slow dynamics should not be measured because they are really not part of the avalanches. This leads to the distinction between fast-moving and slowly-moving dislocations introduced by Miguel *et al.*[67]. In essence, they introduced a cutoff in dislocation speed and measure only dislocations with speed higher than the cutoff. In that way, they tried to retain only the avalanche activities in the acoustic emission signals.

Another way to eliminate the slow dynamics is to study the power spectrum of the signal, instead of studying the signal itself. The slow dynamics, which contributes to a locally smooth background in the total signal then translates into the low frequency end of the power spectrum, which can easily be eliminated. This method is employed by Travesset *et al.* in their study of crackling noise in RFIM[65], in whose work the scaling of the power spectrum is also derived.

We employed yet another method to tackle this problem. Instead of simulating a

very large system, in which all sorts of dislocation activities are present, we simulated a moderate size of system with approximately 10000 atoms. It is found that for this system size, dislocation avalanches come and go, *i.e.,* not many dislocations are left in the system after every avalanche. As a result, no grain boundaries, or slow dynamics, are present and we are able to obtain a very clean avalanche data. It is fair to mention that this method severely limits the system size, and thus the resulting avalanche sizes. The system size we chose contains approximately 100 dislocations in the largest avalanche events. The tradeoff, which we exploit, is the cleanness of the avalanche signal and the speed of the resulting simulations. Different methods, such as those we mentioned above, would have to be employed if larger avalanche sizes are desired.

The method we used to extract the motion of dislocations from the order parameter is described in Appendix B. In short, we count the number of nearest neighbors of each atom, n_i, using the Delaunay triangulation method in computational geometry[180; 181]. Because we have $n_i = 6$ for every atom in a perfectly triangular crystal, and because there is no vacancies in the PFC model (see Chapter 7 for a detailed discussion on vacancies), any atom having $n_i \neq 6$ is sitting next to a dislocation. So these 'defect atoms' are tracking the locations of dislocations. Instead of measuring the total sum of dislocation speeds, $\tilde{V}(t)$, then, we can measure the total sum of speeds of these defect atoms,

$$V(t) = \sum_{i=1}^{N(t)} |\vec{v}_i|, \tag{6.6}$$

where $N(t)$ is the number of defect atoms and $\vec{v}_i$ is the velocity of defect atom i. Note that the velocity of a defect atom is not the velocity of any atom in the system, but the velocity of the dislocation it is tracking. Because the two measures, $\tilde{V}(t)$ and $V(t)$ are proportional to each other with the proportionality constant being the mean number of defect atoms sitting next to a dislocation, we can use the latter for convenience.

Fig. 6.1 shows the typical time dependence of $N(t)$ from a simulation with parameters $dx = 3\pi/8$, $dt = 0.025$, $Lx = Ly = 512$, $\alpha^2 = 255$, $\beta = 0.9$, $v = 1.581$, $\rho_0 = 0.3$ and $r = -0.5$. $N(t)$ changes as dislocations are being created and annihilated. There are intermittent events of creation of dislocations, with number of dislocations involved ranging from a few to 80.

Fig 6.2 shows the acoustic emission signal, $V(t)$, in the same simulation. Similar to $N(t)$, the signal ranges from 0 to 400, with intermittent pulses of various sizes. In order to measure the avalanche event size, we introduce a cutoff $V_{cut} = 15$ to the signal. The signal is then partitioned into individual avalanche events. The probability density of the event energy,

$$E = \int_{t_{begin}}^{t_{end}} V^2(t)dt, \tag{6.7}$$

where t_{begin} and t_{end} are the starting and ending time of the event respectively, can be measured. Different values of V_{cut} has been used and the result is found to be insensitive to it because the cutoff, $V_{cut} = 15$, which corresponds to activities of approximately $3 - 4$ dislocations in the system, is small compared with the signal.

Different shearing rates are applied. For each shearing rate, at least 10 different realizations are run to obtain a statistically meaningful result. This results in about 8000 avalanche events for each shearing rate. Fig 6.3 shows the event size distribution for different shearing rates. We found that the distribution follows a power law for small event size and cuts off at larger sizes, with the cutoff size depending on the shearing rate. The data is noisier towards the end of large event size because large events are rare. This is analogous to the power-law distribution of crackling noise in RFIM, with the cutoff event size depending on the amount of disorder in the system.

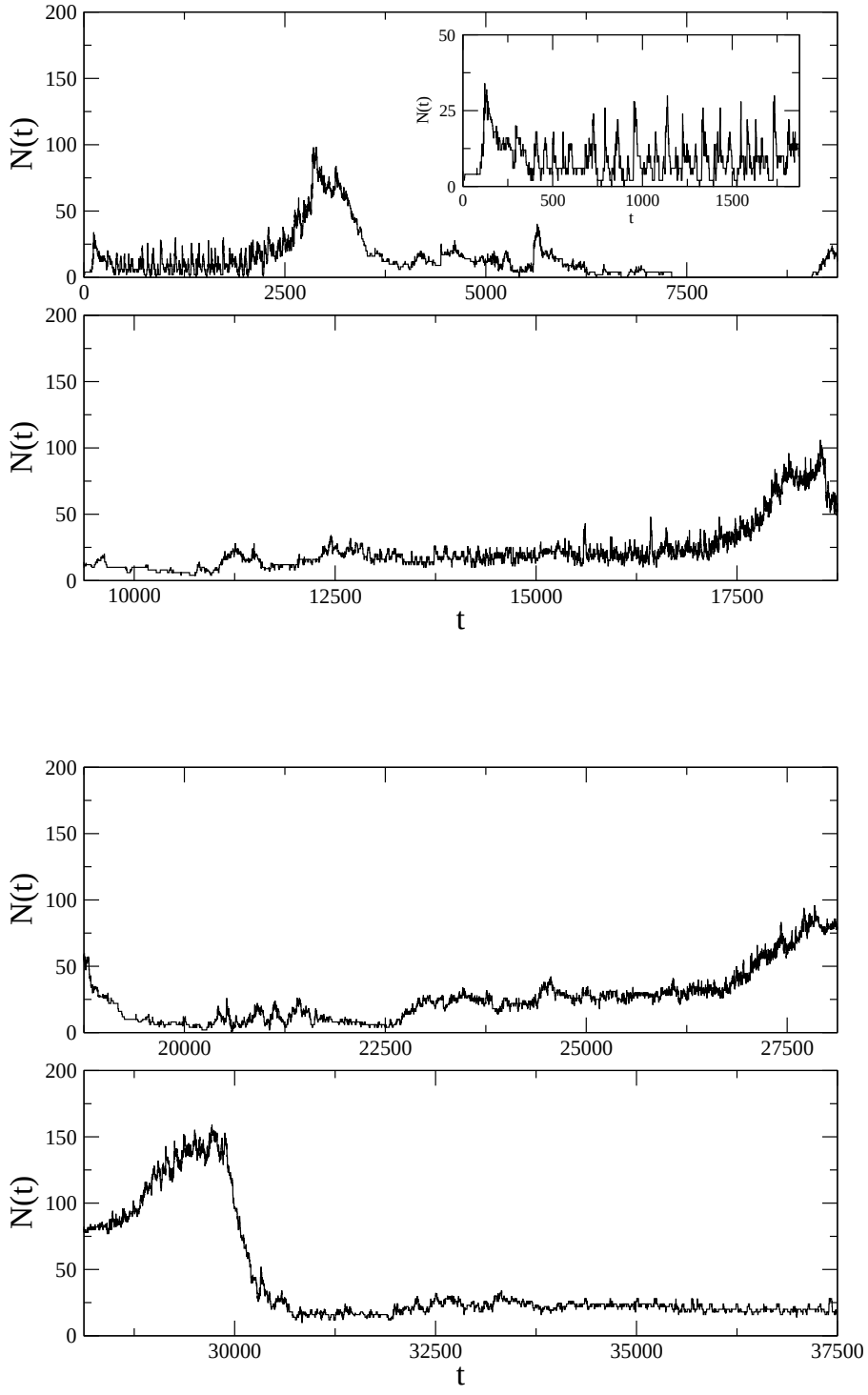

Figure 6.1: The number of dislocations in a sheared PFC crystal. Intermittent events with sizes differing in orders of magnitude is observed. Parameters are $\alpha^2 = 255$, $\beta = 0.9$, $v = 1.581$, $\rho_0 = 0.3$ and $r = -0.5$.

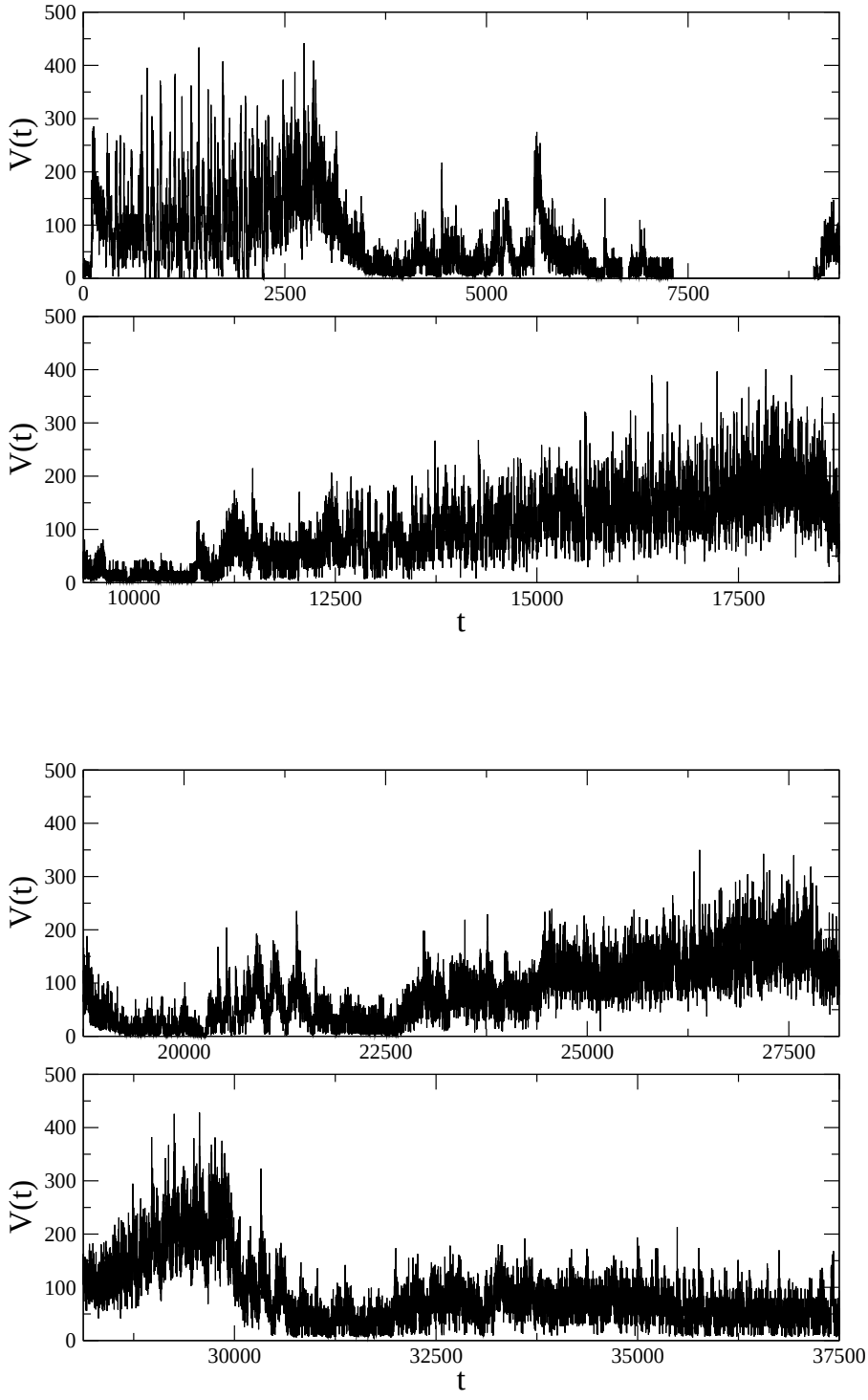

Figure 6.2: The total speed of defect atoms in a sheared PFC crystal. Intermittent events with sizes differing in orders of magnitude is observed. Parameters are $\alpha^2 = 255$, $\beta = 0.9$, $v = 1.581$, $\rho_0 = 0.3$ and $r = -0.5$.

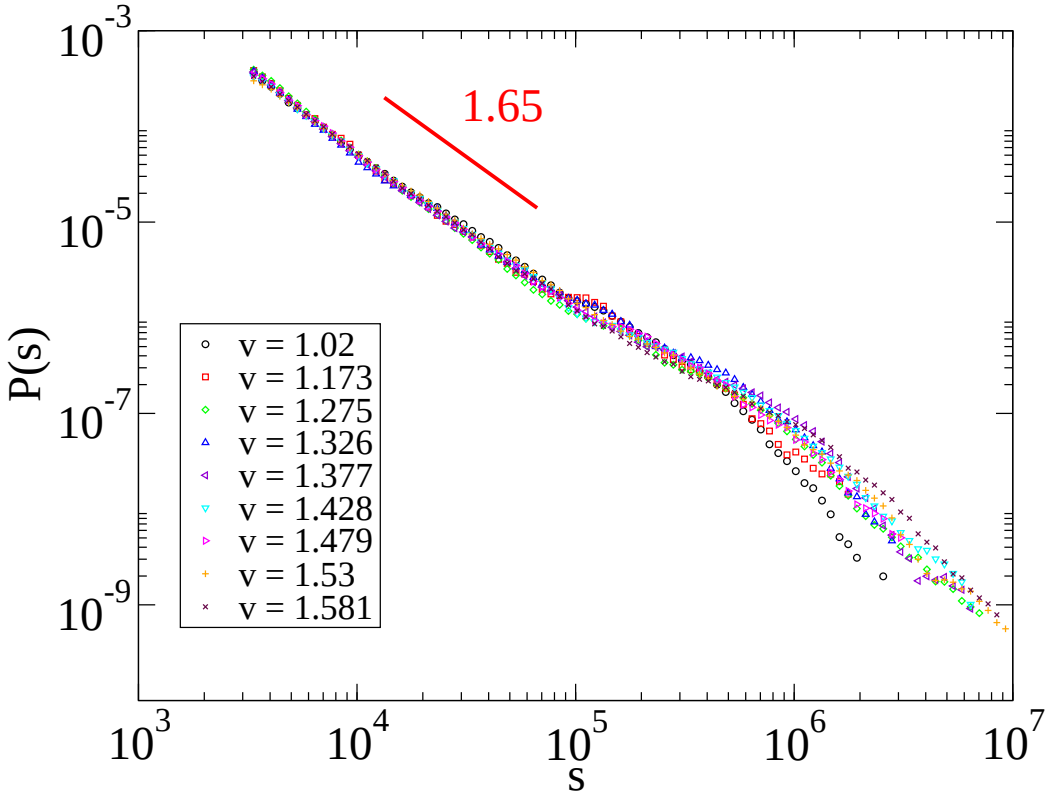

Figure 6.3: (Color online) The probability density of the event energy during dislocation avalanches, for different values of the shearing rates. They follow a power law with an exponent 1.65, with rate-dependent cutoffs.

6.3 Scaling Behavior

We would like to study the scaling behavior of the avalanches. Analogous to the scaling behavior in the RFIM, we propose that there should be a non-equilibrium critical point, $v = v_c$, in the system and we expect, as $s \to \infty$, the data around the critical point to collapse in the form

$$P(s, \bar{v}) = s^{-\alpha} f(s^{\beta} \bar{v}), \tag{6.8}$$

where $P(s, \bar{v})$ is the probability density of event energy, s, $\bar{v} \equiv 1 - v/v_c$ is the reduced shearing rate with v being the shearing rate and v_c being the critical shearing rate. α and β are two critical exponents. As $\bar{v} \to 0$, $P(s, \bar{v})$ tends to a power law

$$P(s, \bar{v}) \sim s^{-\alpha}. \tag{6.9}$$

Fig. 6.4 shows an attempt to collapse the data in this way, with $\alpha = 1.65 \pm 0.2$, $\beta = 1.0 \pm 0.3$ and $v_c = 1.7595 \pm 0.05$. Logarithmic binning with about 100 bins is performed and singletons are ignored to obtain $P(s, \bar{v})$. We see that there is a satisfactory data collapse over 4 decades, with $\bar{v}$ ranging from 0.03 to 0.38. Note that as $s \to 0$, the curve tends to a constant, which agrees with Eq. (6.9). It should be noted that the quality of the data collapse for large s is compromised by the fact that large events are rarer and good statistics are difficult to obtain.

To the authors' knowledge, this is the first attempt to examine the scaling behavior of plastic flow under shearing. A related studies was carried out by Miguel *et al.*. They examined the 2D dislocation avalanches of a crystal under compression by performing dislocation dynamics simulations and found that the probability density follows a power law with exponent 1.8 ± 0.2[67], which is very close to the exponent we obtained. The relation between the scaling behavior under shearing and under compression is yet to be discovered.

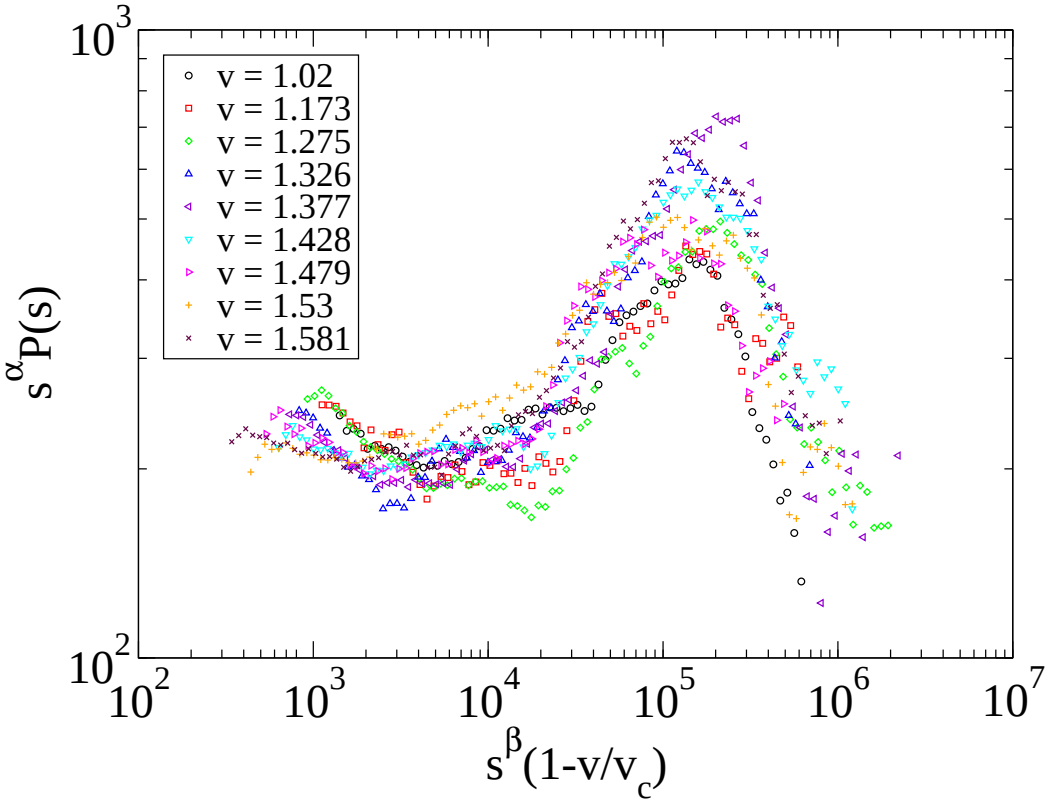

Figure 6.4: (Color online) Data collapse of the probability density of the event energy during dislocation avalanches, with $\alpha = 1.65$, $\beta = 1.0$ and $v_c = 1.7595$.

6.4 Conclusion

To conclude, by shearing a PFC crystal and measuring the resulting dislocation avalanches, we found that there is a non-equilibrium critical point governing this dynamics, analogous to the critical dynamics of the random field Ising model (RFIM). We obtained a data collapse and found the critical exponents and the scaling functions associated with this critical point.

This is the first attempt to study the scaling behavior of plastic flow under shearing. The data collapse of the event energy distribution is the chief indicator of the non-equilibrium critical point. By analogy with the scaling behavior of the RFIM, we anticipate a variety of other scaling phenomena. These include the scaling of the power spectrum, event duration, time lapse between events, event shape and various correlation functions.

Together with the last chapter, we have shown that by introducing a periodic ground state, the PFC model not only captures the correct form of nonlinear elasticity, it even captures microscopic dislocation avalanches and the resulting macroscopic plastic properties of multicrystalline materials. The PFC model appears to be a flexible and efficient way to model multiscale phenomena in materials.

Chapter 7

Vacancies

7.1 Introduction

By encouraging the ground state to be spatially periodic and penalizing any derivation from it, the phase field crystal (PFC) model[60; 61] puts the microscopic and macroscopic scales on equal footing and provides a theoretical framework to describe both crystallography and elasticity of crystals. This enables us to study a variety of phenomena including multicrystalline solidification, grain growth, dislocation dynamics, linear and nonlinear elasticity, as well as plasticity, as we have seen in previous chapters.

Although the PFC model contains such microscopic information, the model is only a description of the collective, or emergent, properties of the crystal; it does not attempt to describe the motion of each individual atom. For example, the number of PFC 'atoms' is not well defined in the model because the order parameter, $\rho(\vec{x}, t)$, can form many peaks ('atoms') as long as that helps to minimize the total energy of the system. This negligence of the actual atomic configuration and the resulting absence of vacancies in the description prevent us from using the model to describe a range of microscopic phenomena, such as those that involve vacancy diffusion and atomic hopping. For this reason, we would like to modify the PFC model to accommodate

the exact atomic configuration.

The goal of this chapter is carry out the above modification—to modify the PFC model such that it not only describes the collective behavior, but also the motions of individual atoms. We will see that this can be done by constraining the value of the order parameter. By doing so, instead of being an abstract order parameter, $\rho(\vec{x}, t)$ becomes a physical density—the number of atoms in the model can be controlled by adjusting the value of ρ_0. The resulting theory is very much like molecular dynamics: we can specify the temperature, number of atoms and the interaction potential between atoms. We can even use the PFC model to simulate a simple liquid.

7.2 Inclusion of Vacancies

In real materials, vacancies are present when the local density is low, *i.e.,* when there are not enough atoms to fill up the space. In the PFC model, however, even if the value of the order parameter is small, which is analogous to the low density situation, a perfectly periodic configuration can still be formed because there is no constraint, or energy penalty, for negative values of the order parameter. The system can always 'borrow more field' by going negative, and thus there is no such situation as 'not enough atoms.' Therefore, as long as the system is in the triangular phase, any uniform configuration would evolve to a spatially periodic one in equilibrium. The notion of vacancies is not respected in this model. If a vacancy is created through a special initial condition, the free volume will simply diffuse throughout the crystal.

We show below that we can stabilize vacancies by imposing a constraint on the order parameter—we forbid the order parameter to be negative. In this case, if the local order parameter is not high enough, instead of forming a periodic state that extends to negative values, the system can form a periodic structure in some region, while leaving a very low, or zero, density in another. The number of atoms in this

case would then be conserved and these zero density regions are vacancies.

In order to justify the above intuition, we have to show mathematically that the addition of the constraint, $\rho(\vec{x},t) > 0$ for all $\vec{x}$, does indeed allow vacancies in the ground state. We will refer to this as the positivity of density constraint. We would like also to identify the region of the phase diagram in which vacancies are present. This can be done by calculating the energy of a state with vacancies.

We begin our investigation by reviewing the calculation of the ground state energy in the original PFC model. In two dimension, if we put the ansatz for the triangular state,

$$\rho(\vec{x}) = A\sum_{j=1}^{3}\left(e^{i\vec{k}_j\cdot\vec{x}} + e^{-i\vec{k}_j\cdot\vec{x}}\right) + \rho_0, \tag{7.1}$$

into the PFC free energy density,

$$f = \frac{\rho}{2}\left(r + (1+\nabla^2)^2\right)\rho + \frac{\rho^4}{4}, \tag{7.2}$$

and average over the whole system, we get the free energy density as a function of the constant amplitude, A,

$$f_0(\rho_0, A) = \frac{45}{2}A^4 - 12A^3\rho_0 + \frac{\rho_0^2}{4}(2 + 2r + \rho_0^2) + 3A^2(r + 3\rho_0^2). \tag{7.3}$$

By minimizing $f_0(\rho_0, A)$ with respect to A, we found that the two solutions for A are

$$A_\pm(\rho_0) = \frac{1}{15}\left(3\rho_0 \pm \sqrt{-15r - 36\rho_0^2}\right), \tag{7.4}$$

where the solution $A = A_+(A_-)$ minimizes the energy for $\rho_0 > 0$ (< 0).

Now, let us consider the effect of the positivity of density constraint. The only additional consideration is the constraint that the order parameter, $\rho(\vec{x},t)$, has to be non-negative in all space. By using the ansatz, Eq. (7.1), this is equivalent to requiring $|A| \le \rho_0/6$. However, we note that from Eq. (7.4) that $|A_+(\rho_0)| > \rho_0/6$ for all values of r and ρ_0, so the original PFC ground state is forbidden by the constraint. This is because ρ can become negative in some regions, independent of ρ_0. The ground state has to be given by some other configuration.

There are at least two possible configurations for the ground state. First, the ground state can still be perfectly periodic with an amplitude $A \neq A_+$ satisfying $|A| < \rho_0/6$. Second, the ground state can partition itself into two domains—a perfectly periodic domain with density ρ_1 and amplitude A_1 satisfying $|A_1| \leq \rho_1/6$, and a domain with $\rho(\vec{x}) = 0$. The second domain would then correspond to vacancies. We have to calculate the energy of these two states and the ground state would be the one with lower energy.

Let us first calculate the free energy density of a perfectly triangular state. Again, we substitute the ansatz Eq. (7.1) into the free energy and minimize the resulting energy with respect to A. As we have seen, the amplitude of the ground state is given by $A = A_+(\rho_0)$. But since $A_+(\rho_0) > \rho_0/6$ for all r and ρ_0, this amplitude is actually forbidden. We are left with several options for A, namely, $A = A_-$, which is the other local minimum of the free energy, $A = \rho_0/6$ and $A = -\rho_0/6$. The latter two are the boundary values satisfying the condition $|A| \leq \rho_0/6$. Because $f_0(\rho_0, \rho_0/6) \leq f_0(\rho_0, -\rho_0/6)$, however, we can ignore the $A = -\rho_0/6$ solution, the free energy density in this case is then given by

$$f_{periodic}(\rho_0) = \begin{cases} f_0\left(\rho_0, \rho_0/6\right) & \text{if } |A_-(\rho_0)| > \frac{\rho_0}{6} \\ \text{Min}(f_0(\rho_0, A_-(\rho_0)), f_0(\rho_0, \rho_0/6)) & \text{otherwise,} \end{cases}$$

where $\text{Min}(a, b)$ denotes the minimum of a and b. Explicitly, we have

$$f_0(\rho_0, A_-(\rho_0)) = \frac{-13}{500}\rho_0^4 + \frac{7r+25}{50}\rho_0^2 - \frac{20r\rho_0 + 48\rho^3}{375}\sqrt{-15r - 36\rho_0^2} - \frac{1}{10}r^2, \quad (7.5)$$

and,

$$f_0\left(\rho_0, \frac{\rho_0}{6}\right) = \frac{1}{288}(133\rho_0^4 + (144 + 168r)\rho_0^2). \quad (7.6)$$

Now, let us compare the energy of these two possible ground states. If the system is perfectly periodic over the whole domain, the free energy is given by

$$f_{whole}(\rho_0) = B_0 f_{periodic}(\rho_0), \quad (7.7)$$

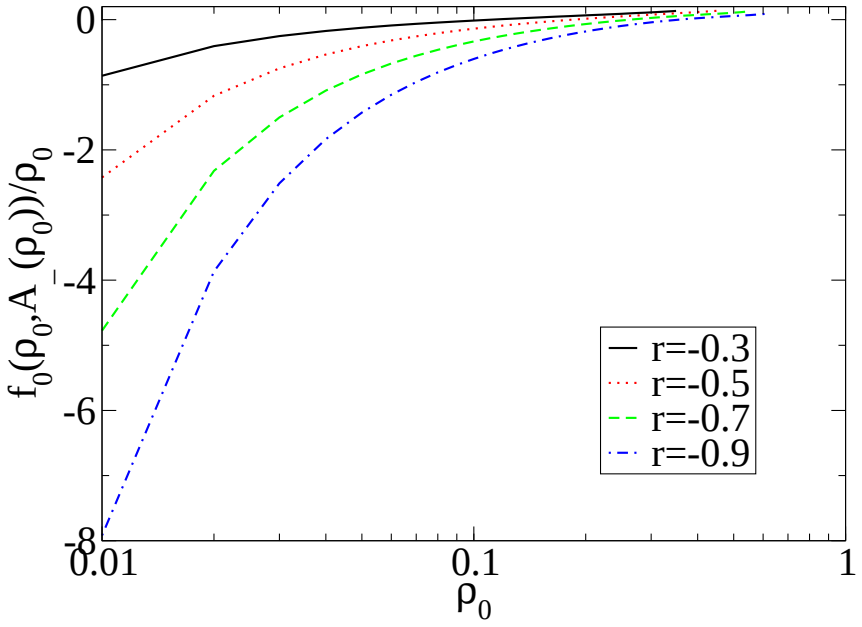

Figure 7.1: The plot $f_0(\rho_0, A_-(\rho_0))/\rho_0$. It is an increasing function of ρ_0, for various values of r. The x-axis is plotted on logarithmic scale in order to resolve the curves.

where B_0 is the area of the whole system. If the system partitions itself into a domain with triangular phase and a domain with $\rho = 0$, the free energy is given by (for simplicity, surface energy between the two phases is neglected in this calculation.)

$$f_{vac}(\rho_0) = b_1 f_{periodic}(\rho_1) = \frac{\rho_0 B_0}{\rho_1} f_{periodic}(\rho_1), \tag{7.8}$$

where b_1 is the area of the triangular domain and ρ_1 is the averaged density within that domain. The second equality is obtained by using the conservation of density $\rho_0 B_0 = \rho_1 b_1$. The difference between these two free energies, $\Delta f \equiv f_{whole} - f_{vac}$, is

$$\Delta f = B_0 \rho_0 \left(\frac{f_{periodic}(\rho_0)}{\rho_0} - \frac{f_{periodic}(\rho_1)}{\rho_1} \right). \tag{7.9}$$

It is important to note that ρ_1 is a parameter we can choose to minimize the energy of the second possible state; the only constraint is that $\rho_1 \geq \rho_0$ because $b_1 \leq B_0$.

For vacancies to exist, we require that $\Delta f > 0$ for some values of $\rho_1 > \rho_0$. We note, however, that for the solution $A = A_-$, $f_0(\rho_0, A_-(\rho_0))/\rho_0$ is an increasing function of

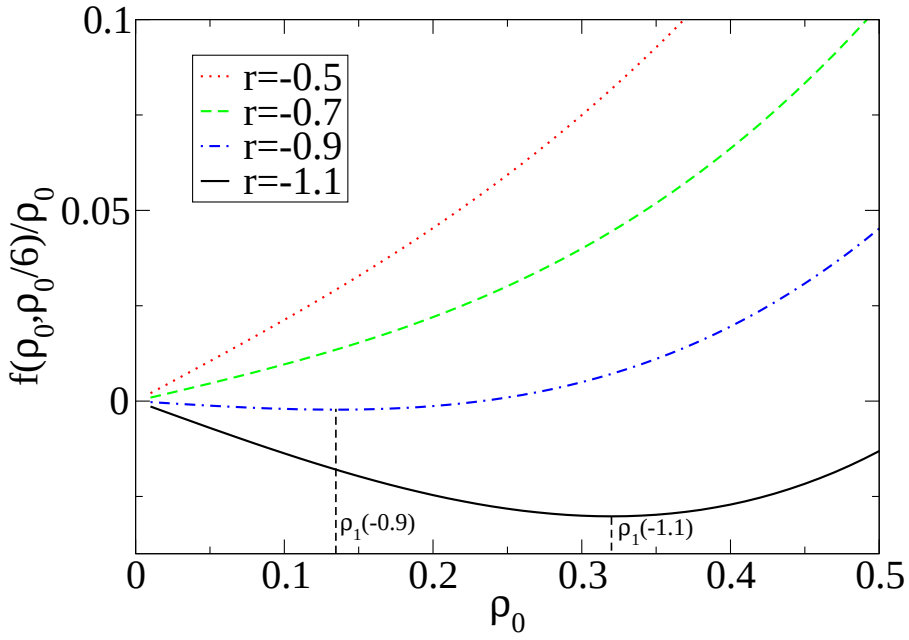

Figure 7.2: The plot of $f_0(\rho_0, \rho_0/6)/\rho_0$. For $r \geq -72/84$, it is an increasing function of ρ_0. For $r < -72/84$, there is a minimum, $\rho_1 = \sqrt{(-48-56r)/133}$.

ρ_0 (see fig. 7.1) and so Δf is positive for this branch of the solution. In other words, no vacancy is present in this solution. In order to have vacancies in the ground state, then, we require this branch of the solutions to be forbidden by the constraint; that is, we require $|A_-(\rho)| > \rho/6$, which is equivalent to requiring

$$\rho_0, \rho_1 < \sqrt{\frac{-12r}{53}}. \tag{7.10}$$

On the other hand, we note that,

$$\frac{f_0(\rho_0, \rho_0/6)}{\rho_0} = \frac{1}{288}(133\rho_0^3 + (144+168r)\rho_0). \tag{7.11}$$

There is a minimum at $\rho_0 = \sqrt{(-48-56r)/133}$ if $r < -72/84$ (see fig. 7.2). In other words, if $\rho_0 < \sqrt{(-48-56r)/133}$ and $r < -72/84$, the system can minimize the free energy by rolling down the energy landscape and arrive at the minimum

$$\rho_1 = \sqrt{\frac{-48-56r}{133}}. \tag{7.12}$$

In this case, only part of the domain, whose area is given by

$$b_1 = \frac{B_0\rho_0}{\rho_1} = \frac{\sqrt{133}B_0\rho_0}{\sqrt{-48-56r}} \tag{7.13}$$

would be composed of atoms; the remainder of the domain, whose area is $B_0 - b_1$, would have zero density. This corresponds to the presence of vacancies. We also note that the area of the triangular phase, b_1, is directly proportional to the mean density, ρ_0. So by adjusting ρ_0, we can control the number of atoms in the PFC model. This shows that the addition of the constraint, $\rho(\vec{x}) > 0$ for all $\vec{x}$, does indeed promote the $\rho(\vec{x})$ from an abstract order parameter to a physical density, which dictates the number of atoms in the system.

Together with the constraint on ρ_1, Eq. (7.10), we have shown that for the region

$$\rho_0 < \sqrt{\frac{-48-56r}{133}} \quad \text{and} \quad \frac{-636}{343} < r < \frac{-72}{84}, \tag{7.14}$$

in the triangular phase, the ground state is composed of a triangular phase of area b_1, density ρ_1 and amplitude $A_1 = \rho_1/6$. The rest of the domain, whose area is $B_0 - b_1$, has zero density and thus are vacancies.

7.3 Implementation

Although the constraint does stabilize vacancies in the PFC model, it is mathematically difficult to solve the PFC dynamical equation with such a constraint. An alternative method to mimic the effect of such a constraint is to add a vacancy term, $f_{vac}(\rho)$, to the free energy functional,

$$F[\rho(x)] = \int d^dx \left[\frac{\rho(x)}{2}(r + (1+\nabla^2)^2)\rho(x) + \frac{\rho(x)^4}{4} + f_{vac}(\rho(x))\right]. \tag{7.15}$$

The term $f_{vac}(\rho)$ penalizes any negative values of $\rho(\vec{x}, t)$. If the penalty is large enough, the vacancy term would serve the same purpose as the positivity of density constraint. There are many possible choices for $f_{vac}(\rho)$, for example, we can simply

choose it to be the step function

$$f_{vac}(\rho) = H\Theta(-\rho), \tag{7.16}$$

where H is a real positive number, or,

$$f_{vac}(\rho) = H(|\rho|^n - \rho^n), \tag{7.17}$$

for any odd number n, or we can choose,

$$f_{vac}(\rho) = He^{-\rho/\lambda_{vac}}, \tag{7.18}$$

where λ_{vac} is the penetration depth of the field into negative values. The physical meaning of $f_{vac}(\rho)$ is to add a chemical potential to $\rho(x)$. As long as the repulsion from negative values is strong enough to avoid $\rho < 0$, the result should not depend on any particular choice of $f_{vac}(\rho)$. In the rest of this work, we will use Eq. (7.17) with $n = 3$ and $H = 1500$ because this turns out to be numerically convenient and stable.

With the vacancy term, Eq. (7.17), we can verify our analytical analysis about the vacancy term by comparing it with our simulations. Fig. (7.3) shows simulations with $r = -0.9$ and different values of ρ_0, we see that the number of atoms increases with ρ_0. In addition, fig. (7.4) shows that the PFC atomic density (*i.e.,* the number of atoms per unit area) indeed increases linearly with ρ_0, in agreement with Eq. (7.13). However, the curve starts to saturate at around $\rho_0 = 0.15$, as opposed to the prediction $\rho_0 = \sqrt{(-48 - 56r)/133} \approx 0.134$ from Eq. (7.14). This discrepancy is expected because, first, in the calculation, we have not taken into account the surface energy between the triangular phase and the vacancies, and second, there are thermal fluctuations present in the simulation, which help the system to equilibrate faster; these were not accounted for in the analytic calculation.

Now, the PFC simulation looks very much like a molecular dynamics simulation! But operating on diffusive time scales many orders of magnitude faster than pure

molecular dynamics[61]. We can control the number of atoms and the temperature in the system by adjusting ρ_0 and the magnitude of thermal noise, ϵ, respectively. The interaction potential between individual PFC atoms is specified by the PFC free energy (specifically the gradient terms) and is controlled by the undercooling r. In fact, by decreasing the value of ρ_0 such that the system is dilute enough, we can simulate a liquid using the PFC model! We simulated such a liquid with parameters $r = -0.9$, $\rho_0 = 0.09$, $\alpha = 15$ and $\beta = 0.9$,and a typical result is shown in Fig. (7.3b). Fig. (7.5) shows the two point correlation function, $g(x)$, extracted from the simulation. It resembles the two point correlation function of a liquid—a correlation hole, a strong nearest neighbor correlation and a weak correlation with atoms one or two atomic spacings away[182; 183].

It is important to note that although we have only added a single term to the PFC model, the nature of the order parameter is completely changed. In the original PFC model, $\rho(\vec{x}, t)$ is not a physical density because it can be negative; it is only an abstract mathematical construct, whose function is to keep track of the crystallographic and elastic properties of the underlying crystal it represents. No association to atoms or density should be made. The addition of the vacancy term, however, makes the order parameter a physical density, whose value dictates the number of atoms in the system and whose configuration is the actual atomic configuration. This makes the two models very different.

To conclude, we have shown that with the constraint $\rho(\vec{x}, t) > 0$ in the free energy, vacancies in the PFC model are stabilized and the number of atoms is linearly proportional to the mean value of the order parameter, ρ_0. The effect of the constraint can be mimicked by a vacancy term that penalizes any negative value of the order parameters. Instead of having an abstract order parameter containing only the crystallographic and topological information, which is what we have in the original PFC model, the order parameter is now proportional to the physical density and we

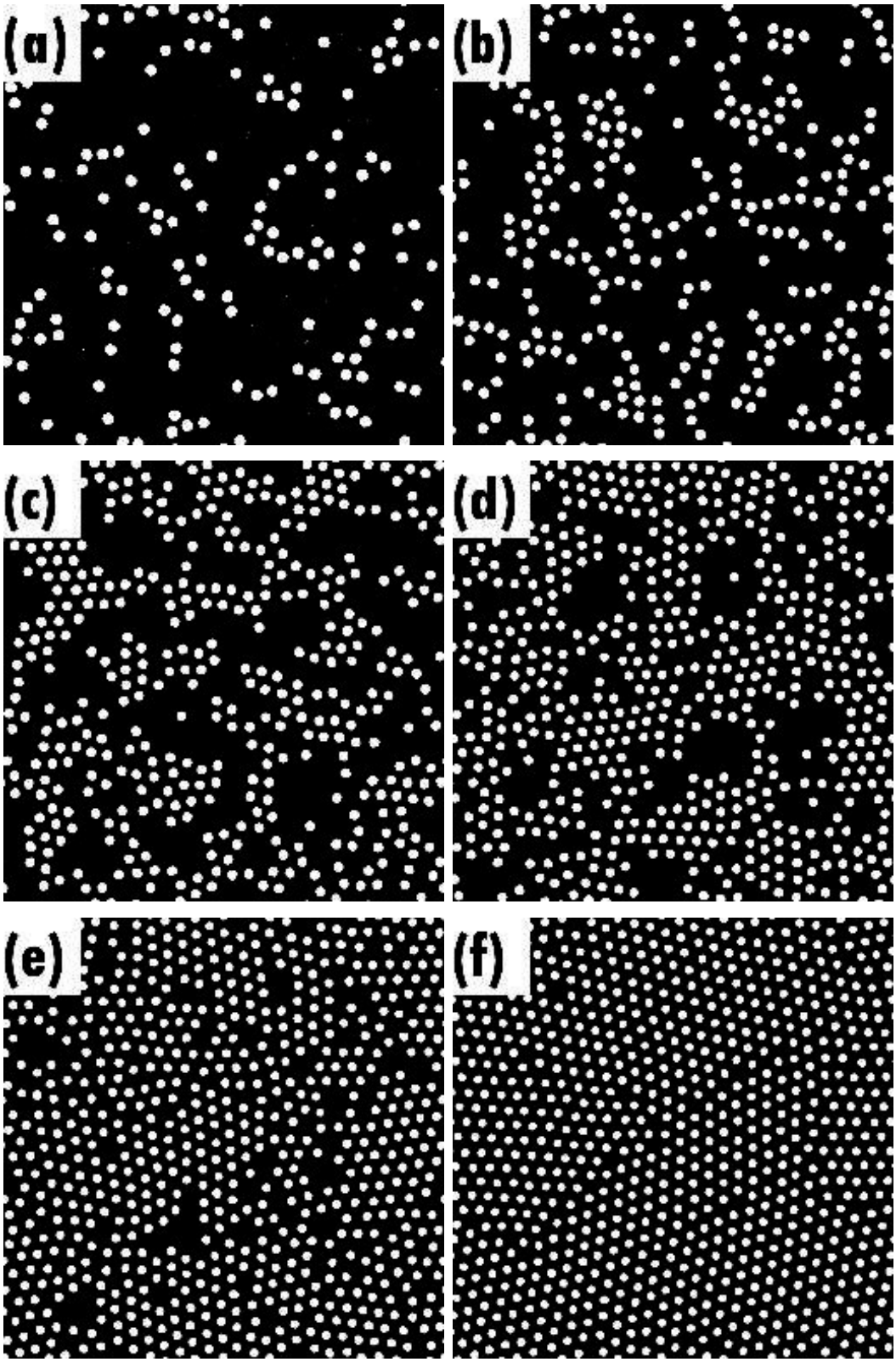

Figure 7.3: PFC simulations with different values of ρ_0 at $r = -0.9$. The number of atoms increases with ρ_0. Figures (a), (b), (c), (d), (e) and (f) correspond to $\rho_0 = 0.06$, 0.08, 0.10, 0.12, 0.14 and 0.16.

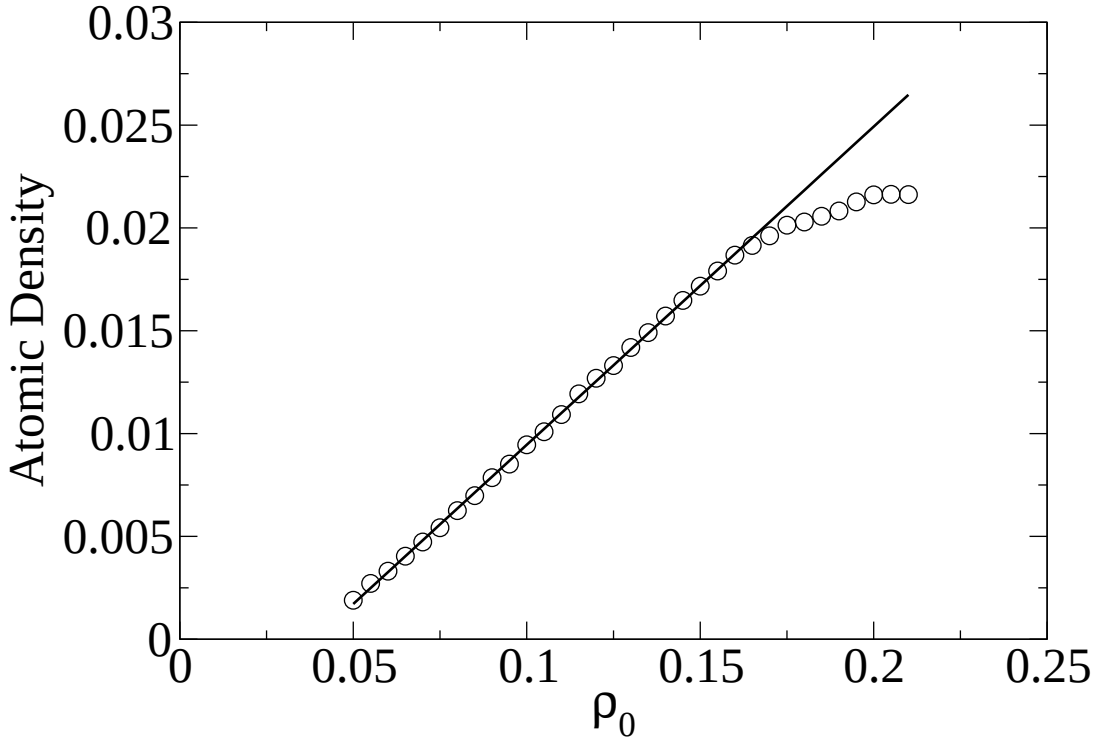

Figure 7.4: The PFC atomic density increases linearly with the order parameter, ρ_0, when the vacancy term is added to the model. $r = -0.9$ is used. The curve starts to saturate at around $\rho_0 = 0.15$, as opposed to the theoretical prediction $\rho_0 = \sqrt{(-48 - 56r)/133} = 0.134$.

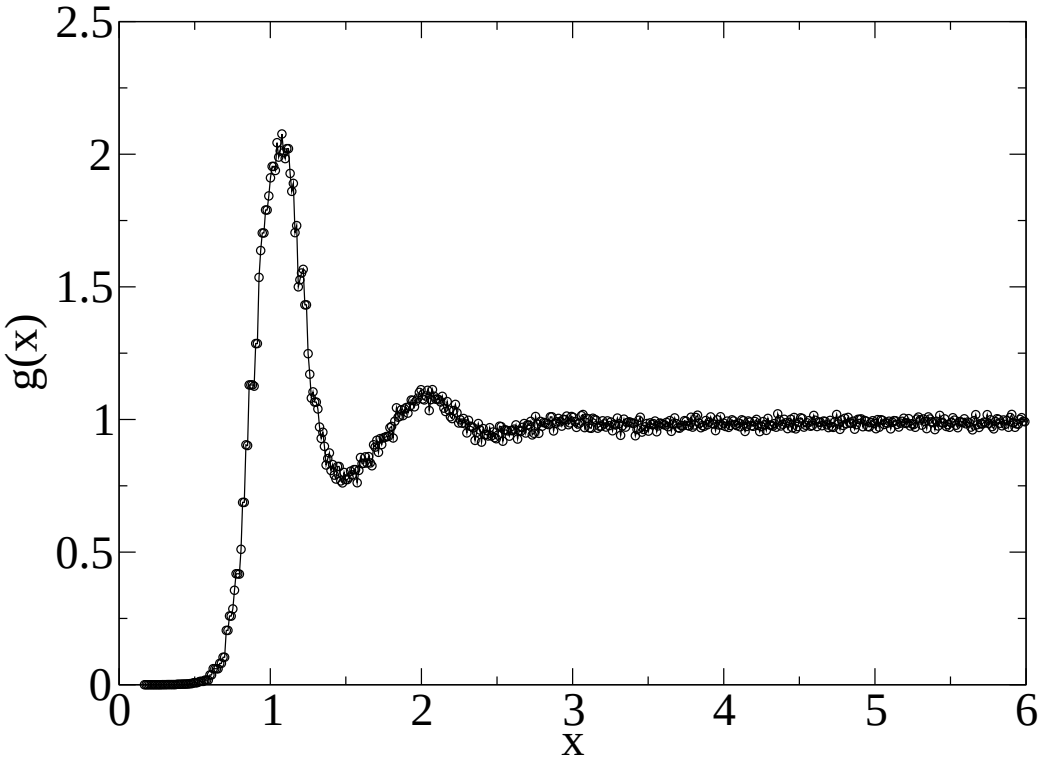

Figure 7.5: The two point correlation function of a liquid using the PFC model. Parameters are $r = -0.9$, $\rho_0 = 0.09$, $\alpha = 15$ and $\beta = 0.9$.

now are able to simulate the actual atomic configuration. The resulting PFC model, in essence, is a molecular dynamics simulation from a partial differential equation, and by varying ρ_0, we can go from simulating a triangular crystal to a liquid.

Chapter 8

Binary Alloys

8.1 Extension of the PFC model

We are now ready to extend the PFC model to binary alloys. Binary alloys are composed of two kinds of atoms. The natural way to model a binary alloy is to put together two PFC free energies for two density fields, ρ_A and ρ_B. But because each individual PFC free energy only specify the interactions between atoms of the same kind, an interaction energy between atoms A and B has to be added. We propose that the interaction free energy density should be of the form

$$f_{int}^{AB}(\rho_A, \rho_B) = \lambda_{AB}\rho_A(q_{AB}^2 + \nabla^2)^2\rho_B + \frac{a}{2}\rho_A^2\rho_B^2 + \frac{b}{2}\left(\nabla\delta c\right)^2, \tag{8.1}$$

where λ_{AB}, a, b are constants and

$$\delta c \equiv \frac{\rho_A - \rho_B}{\rho_{A0} + \rho_{B0}}, \tag{8.2}$$

with ρ_{A0} and ρ_{B0} being the mean values of the order parameters, is the difference in the two densities. The first term in Eq. (8.1) resembles the differential operator in the PFC model; it encourages spatial periodicity among the A and B atoms and in the language of molecular dynamics, specifies the interaction potential between them. The second term imposes a hard core repulsion between the two densities and the

third term avoids any sudden change in the difference in density, which might arise from, say, a mixed atom. The second and third terms together ensure that there is only one dominant field in each PFC atom, *i.e.,* there is no atom with 'mixed fields', *i.e.,* a PFC atom that cannot be uniquely associated with either A or B. Putting all the terms together, our PFC free energy density for binary alloys reads

$$f = f^A_{PFC}(\rho_A) + f^B_{PFC}(\rho_B) + f^{AB}_{int}(\rho_A, \rho_B), \tag{8.3}$$

where

$$f^A_{PFC}(\rho_A) = \frac{\lambda_A}{2}\rho_A[r_A + (q_A^2 + \nabla^2)^2]\rho_A + \frac{u_A}{4}\rho_A^4 + H(|\rho_A|^3 - \rho_A^3). \tag{8.4}$$

Eq. (8.4) is the pure PFC model with the vacancy term, where λ_A, u_A and H are constants, r_A is the undercooling and q_A controls the lattice spacing between A atoms. f^B_{PFC} is defined similarly.

The dynamics is imposed to be dissipative and conservative,

$$\frac{\partial^2 \rho_{A,B}}{\partial t^2} + \beta_{A,B}\frac{\partial \rho_{A,B}}{\partial t} = \alpha^2_{A,B}\nabla^2\left(\frac{\delta f}{\delta \rho_{A,B}}\right) + \eta_{A,B}, \tag{8.5}$$

where $\alpha_{A,B}$ and $\beta_{A,B}$ are constants specifying the instantaneous elastic interactions in the system[151], the Laplacian on the right conserves the total densities $\rho_{A,B}$ and $\eta_{A,B}$ is the thermal noise satisfying the fluctuation-dissipation theorem

$$\langle \eta_i(\vec{x}, t), \eta_j(\vec{x}', t')\rangle = -\epsilon\nabla^2\delta_{ij}\delta(\vec{x} - \vec{x}')\delta(t - t'), \tag{8.6}$$

with ϵ being the noise amplitude proportional to the temperature k_BT.

There are 17 parameters in this model. Just as with the pure PFC model, three parameters, namely λ_A, q_A and u_A, can be absorbed into a rescaling of units. The exact values of a, b and H are not important because their roles are to ensure, respectively, that there are no mixed atoms and that vacancies are stable. λ_B, λ_{AB}, u_B control the relative strength of various terms and in doing so, control the energies of the bonds between the atoms. A larger λ_B, for example, gives a stronger interaction

between atoms B. r_A and r_B are the undercoolings. q_B and q_{AB} control the equilibrium lattice spacing among atoms B, and that between atoms A and atoms B respectively. Finally, $\alpha_{A,B}$ and $\beta_{A,B}$ determine the propagation speed and lifetime of phonons[151]. In most of our simulations, we only change q_B, q_{AB}, r_A, r_B and the noise amplitude, ϵ. Other parameters are fixed to be $a = 200$, $b = 0.1$, $H = 1500$, $\alpha_{A,B} = 1$, $\beta_{A,B} = 0.01$ and $\lambda_B = \lambda_{AB} = u_B = 1$. Fig. 8.1 shows examples of simulations with different values of q_B and q_{AB}.

It is worthwhile to note that a similar model for binary alloys was recently proposed by Elder *et al.*[154]. In their paper, they proposed a PFC model for binary alloys by relating the PFC to density functional theory and regular solution theory. They showed that the model is capable of describing binary alloy solidification, phase segregation, grain growth, elasticity and plasticity. We note that their model and ours are very similar. The two models both capture the microscopic crystallographic and the macroscopic elastic properties of binary alloys. The only difference is that while their model is a direct extension of the pure PFC model to binary alloys, ours is such an extension with the vacancy terms, which makes studying vacancy dynamics and atomic hopping possible. In other words, their model is coarse-grained in both time and composition: time because any atomic vibration is coarsened and only diffusive behavior is retained; composition because although their model retains the crystal orientation, the local composition is averaged out. Our model, however, coarse-grains only in time: we retain the diffusive behavior of the alloys, but we do not coarse-grain in composition, instead, we keep the exact atomic configuration by enforcing the vacancy terms. Our model can be thought of as a more microscopic model, where the actual atomic configurations is resolved, and Elder *et al.*'s coarsens out that configuration. In fact, by coarse-graining the order parameters in our model, one can derive Elder *et al.*'s model[1].

[1]Zhi Huang and Jonathan Dantzig, private communication.

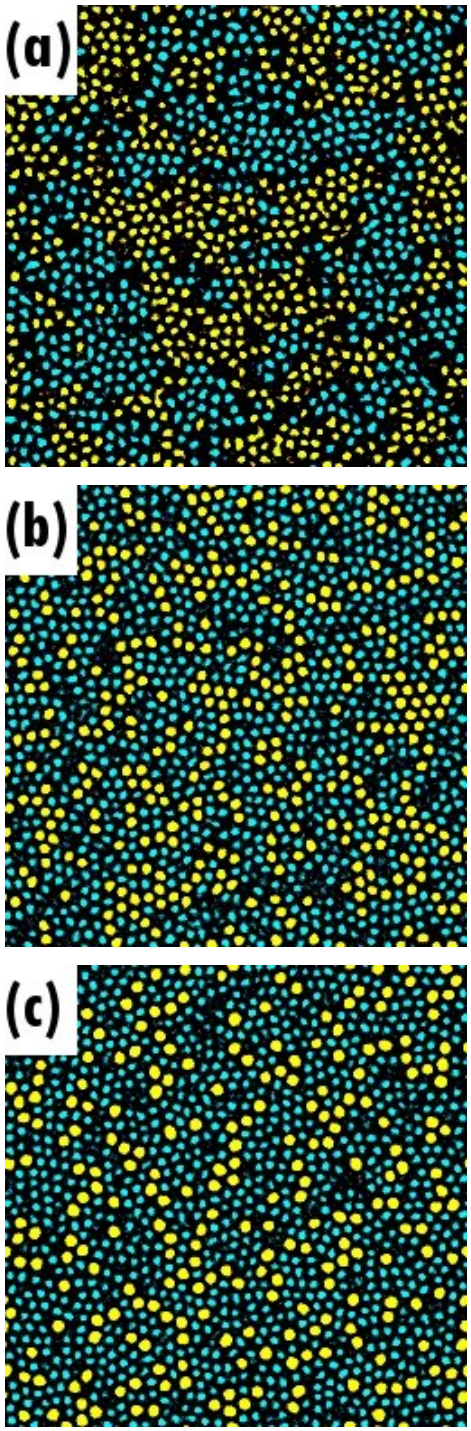

Figure 8.1: (Color online) PFC simulations of binary alloys with different values of q_B and q_{AB}. Blues (yellow) are A (B) atoms. The sizes of the atoms can be controlled by varying q_B and q_{AB}. Figures (a), (b) and (c) corresponds to $q_B = q_{AB} = 1$, 0.9 and 0.8 respectively. $r_A = r_B = -0.9$, $\rho_{A0} = 0.075$ and $\rho_{B0} = 0.06$ are used in all simulations.

8.2 Diffusion

We benchmark our model with a standard diffusion problem. We prepare a rectangular domain with size $L_x \times L_y$, with periodic boundary conditions in both directions. We put atoms A on the left half of the box and atoms B on the right half, that is, we specify the initial condition to be

$$\rho_A(\vec{x}, t=0) = \begin{cases} 2\rho_{A0} & \text{if} \quad x < L_x/2 \\ 0 & \text{if} \quad x \leq L_x/2, \end{cases} \tag{8.7}$$

and,

$$\rho_B(\vec{x}, t=0) = \begin{cases} 0 & \text{if} \quad x \leq L_x/2 \\ 2\rho_{B0} & \text{if} \quad x > L_x/2. \end{cases} \tag{8.8}$$

At the beginning of the simulation, the two uniform fields crystallize and form two crystals with atoms A and B. Then, the two kinds of atoms start to diffuse into each other. Fig. 8.2 shows snapshots of such a simulation with $L_x = 1024$, $L_y = 512$, $dx = 1$, $dt = 0.05$, $\rho_{A0} = \rho_{B0} = 0.08$, $r_A = r_B = -0.9$ and $\epsilon = 1 \times 10^{-4}$ for different times. We observed that the initially separated atoms diffuse into each other. Both the microscopic atomic hopping and macroscopic diffusive profile are captured in the simulations.

To compare this result with a standard one-dimensional diffusion problem, we define the averaged concentration

$$C(x,t) \equiv \frac{1}{2\rho_{A0} L_y} \int_0^{L_y} \rho_A(L_x x, y, t) dy. \tag{8.9}$$

The initial condition can then be written as

$$C(x, t=0) = \begin{cases} 1 & \text{if} \quad x < 0.5 \\ 0 & \text{if} \quad x > 0.5, \end{cases} \tag{8.10}$$

with $0 \leq x \leq 1$. Fig. 8.3 shows the plot of $C(x,t)$ at different time.

We can extract the diffusion coefficient from $C(x,t)$. Recall that for a standard diffusion equation,

$$\frac{\partial u(x,t)}{\partial t} = D\frac{\partial^2 u(x,t)}{\partial x^2}, \tag{8.11}$$

with the periodic boundary conditions $u(0,t) = u(L_x,t)$, the solution is given by the Fourier series expansion

$$u(x,t) = \sum_{n=0}^{\infty} e^{-k_n^2 Dt}[a_n \cos(k_n x) + b_n \sin(k_n x)], \tag{8.12}$$

where $k_n \equiv 2\pi n/L_x$, a_n and b_n are constants determined by the initial condition. So, we can extract the Fourier coefficient

$$C_n(t) = \frac{2}{L_x}\int_0^1 C(x,t)\sin(k_n x)dx \tag{8.13}$$

from the diffusion profile of the simulation, and the diffusion coefficient can be extracted by fitting $C_n(t)$ to

$$C_n(t) = C_n(0)e^{-k_n^2 Dt}, \tag{8.14}$$

or,

$$k_n^{-2}\ln(C_n(t)) = -Dt + k_n^{-2}\ln(C_n(0)). \tag{8.15}$$

We extracted $C_1(t)$ from the simulation. Fig. 8.4 shows that $k_1^{-2}\ln(C_1(t))$ does indeed decrease linearly with time t. This confirms that the dynamics of the binary alloy follows the diffusion equation on the macroscopic scale. The diffusion coefficient, which is the magnitude of the slope of the line, is fitted to be $D = 0.32$ in this particular case.

This recovery of the diffusive behavior is not trivial. Instead of having a smooth diffusive field, which is what we would have in a standard diffusion equation, we have the atomic configuration in the PFC model. In other words, the overall diffusive behavior consists of individual events of atomic hopping. In fact, we can see from the simulation that various diffusion mechanics, such as ring diffusion and diffusion

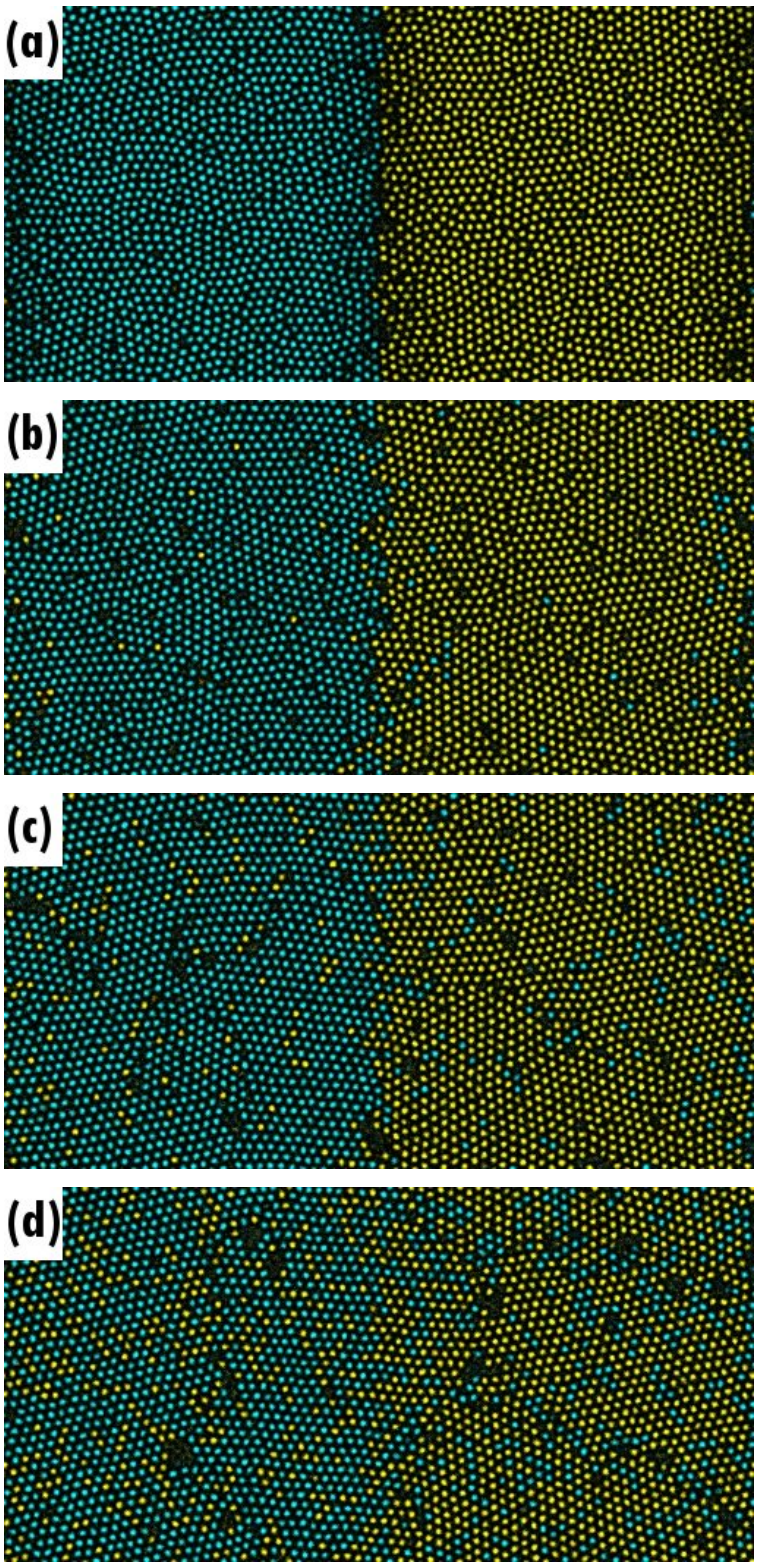

Figure 8.2: (Color online) PFC simulations of a diffusion couple of size 512×256. Parameters values are $\rho_{A0} = \rho_{B0} = 0.08$, $r_A = r_B = -0.9$ and $\epsilon = 1 \times 10^{-4}$. Fig. (a), (b), (c) and (d) correspond to $t = 60$, 300, 3000 and 15000 respectively.

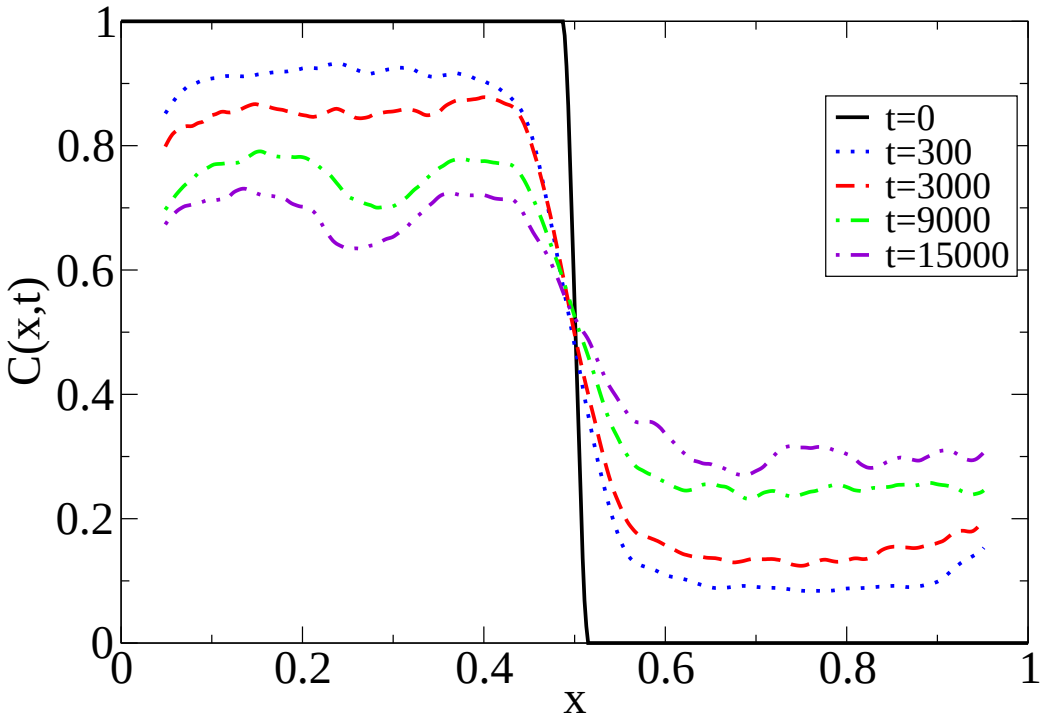

Figure 8.3: (Color online) The concentration profile of a diffusion couple. The profile is smoothed by doing a local average with bin size 0.05. Parameters values are $\rho_{A0} = \rho_{B0} = 0.08$, $r_A = r_B = -0.9$ and $\epsilon = 1 \times 10^{-4}$.

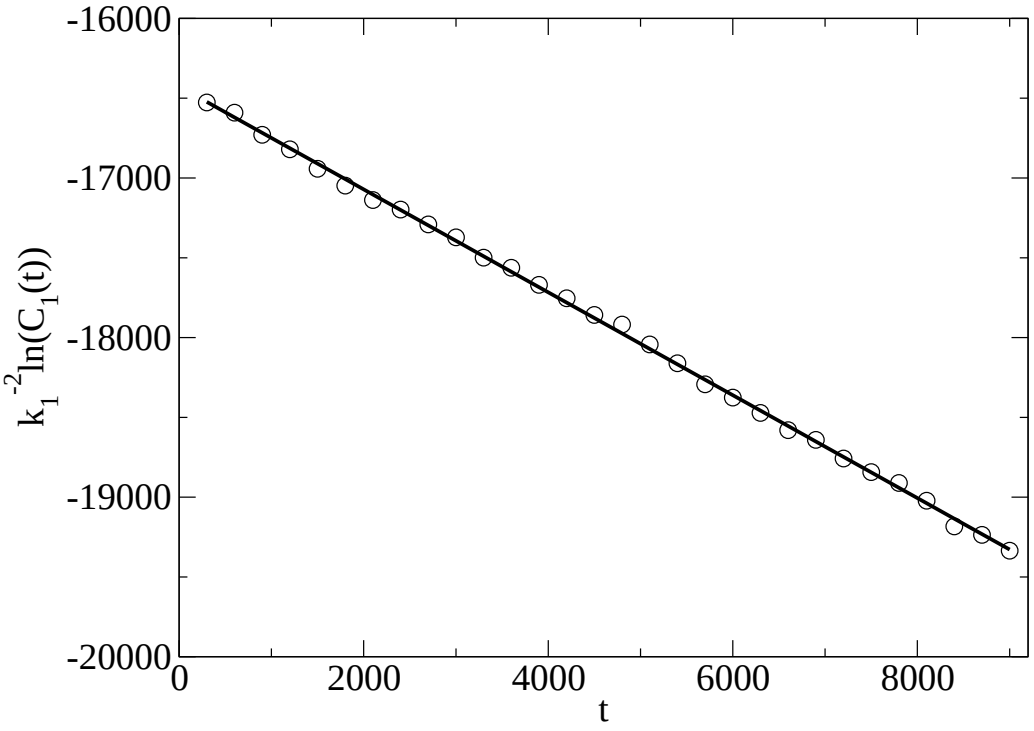

Figure 8.4: The first Fourier coefficient of the concentration profile, $C_1(t)$, is fitted to the theoretical prediction, Eq. (8.14). The diffusion coefficient, D, is fitted to be 0.32.

along grain boundaries, are at work in the model. We are simulating the macroscopic diffusion and the microscopic hopping at the same time.

The temperature dependence of the diffusion coefficient, $D(\epsilon)$, is also studied. We run simulations with various values of the noise amplitude, ϵ. Because r_A and r_B are the undercooling parameters

$$r_{A,B} = \frac{T - T_c^{A,B}}{T_c^{A,B}} = \frac{\epsilon - \epsilon_c^{A,B}}{\epsilon_c^{A,B}}, \tag{8.16}$$

where $T_c^{A,B}$ or $\epsilon_c^{A,B}$ are the melting temperatures for solids A and B, they also have to be varied consistently. Fig. 8.5 shows the temperature dependence of $D(\epsilon)$ over the range $1{\times}10^{-4} < \epsilon < 1.6{\times}10^{-4}$, with parameters $\epsilon_c^{A,B} = 1{\times}10^{-3}$ and $\rho_{A0} = \rho_{B0} = 0.08$. We found that $D(\epsilon)$ follows the activated Arrhenius form $D(\epsilon) = D_0 e^{-E_{act}/\epsilon}$[184], with $D_0 = 682$ and $E_{act} = 3.3 \times 10^{-4}$.

8.3 Conclusion

We have extended the PFC model to binary systems. We have shown that the resulting model not only describes microscopic crystallography, atomic hopping and vacancy diffusion, but also describes the macroscopic diffusive behavior. By varying the noise amplitude in the simulation, we have shown that the diffusion coefficient implied by the PFC model satisfies the standard Arrhenius form, $D(T) = D(0)e^{-E_{act}/k_B T}$.

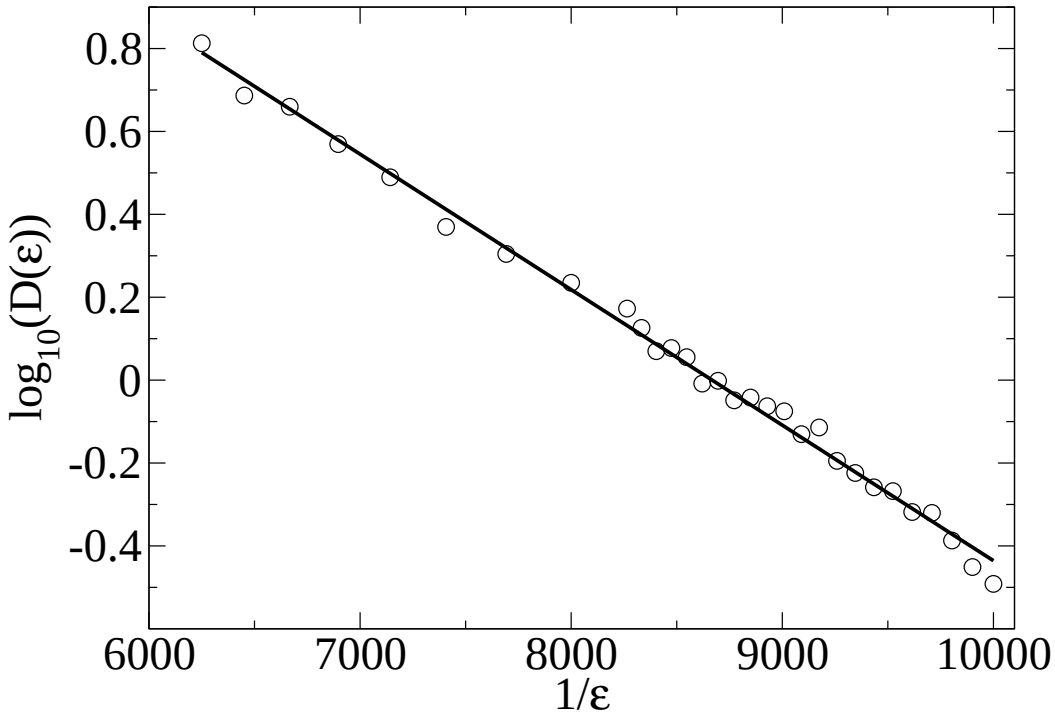

Figure 8.5: Temperature dependence of the diffusion coefficient. The diffusion coefficient follows the Arrhenius form, $D(\epsilon) = D_0 e^{-E_{act}/\epsilon}$, with $D_0 = 682$ and $E_{act} = 3.3 \times 10^{-4}$.

Chapter 9

Conclusions

In this dissertation, I presented numerical and analytical work on three physical systems, of increasing complexity. The overarching theme across these systems is scaling behavior, which is universal and depends only on symmetry, dimensionality and phenomenology of the systems.

I first discussed the peculiar scaling near the Griffiths-paramagnetic transition point in Griffiths ferromagnets, *i.e.,* ferromagnets with disorder. Because disorder is present throughout the system and it partitions the whole ferromagnet, a Griffiths ferromagnet, heuristically, can be thought of as an ensemble of weakly interacting pure ferromagnetic islands, each of a different size, and thus, of a different critical temperature, T_c. The scaling behavior of each ferromagnetic island is given by the scaling behavior of a finite-size Ising model. Because the total magnetization is the sum of the contributions from individual islands, and at $T = T_c$, the magnetization of the island is singular in external field h, the total magnetization of the system is singular in h at temperature T, for T equals to the critical temperature of one of the ferromagnetic islands. As the distribution of the island sizes becomes continuous in the thermodynamic limit, the total magnetization becomes (weakly) singular in h for a range of temperature, $T_c < T < T_G$, where T_c (T_G) is the smallest (largest) critical temperature among that of the islands. This is the Griffiths phase.

The scaling behavior of Griffiths ferromagnets is qualitatively different from that of conventional ferromagnets, due to the essential singularity in h. In fact, the scaling behavior of Griffiths ferromagnets was not known and there was no clear experimental evidence supporting the existence of such a phase in disordered ferromagnets, despite decades of theoretical and experimental efforts. By using an ansatz for the Yang-Lee zero density, however, we succeeded in deriving the scaling behavior and the asymptotics of magnetization of Griffiths ferromagnets. We found excellent agreement between our theory and the experimental data on $La_{0.7}Ca_{0.3}MnO_3$, from which we also extracted the critical exponent. This is the first direct experimental evidence of the existence of the Griffiths phase.

We then studied geophysical precipitation pattern formation near geothermal hot springs. As hot spring water flows out from the vent and then down the landscape, spring water cools down and precipitates carbonates onto the surface. This changes the surface, which in turn changes the flow path of the spring water. This dynamic interplay between fluid flow, surface growth and precipitation dynamics give rises to all sort of beautiful and interesting travertine patterns observed in the Yellowstone National Park.

I introduced an analytical framework to study this complex pattern forming dynamics. It was composed of three nonlinear coupled partial differential equations, describing the fluid flow, surface growth and precipitation dynamics. Although the equations are complicated, I succeeded in solving them in cases of simple geometry and found that the solutions agree with the shapes of spherically symmetric domes and the stalactites observed near geothermal hot springs and in limestone caves respectively. We also calculated the linear stability of the solutions and found that while stalactites are unconditionally stable, domes are not. We attributed this difference in stability to the different roles of surface tension in the system and the absence of surface tension in our analysis.

In the case of domes, I also found that our analytical theory deviates from the field observations beyond a critical angle θ_c. This is because as the fluid flows down the dome and covers more surface, it thins out and at some point, breaks into rivulets due to surface tension. Although our theory does not take into account the effect of surface tension, it does predict a scaling behavior of θ_c. We verified this scaling behavior by using a CDS model.

It is not trivial to solve the analytical equations in complicated geometry, and thus it is difficult to study the full nonlinear regime of the equations, but by calculating the linear stability spectrum, we found that a turbulent flow down a constant slope is unstable in all scales. This is consistent with the scale free terraced landscape observed in the field.

This study is one of the first attempts to quantitatively model pattern formation in carbonate precipitating systems, in the new and exciting research area of geophysical pattern formation. We anticipate similar theoretical advances to be made on other precipitation pattern forming systems, such as terraced landscapes found near silicious springs.

In the last project we studied multiscale phenomena in materials using the phase field crystal (PFC) model. The PFC model is essentially a density functional theory describing the perioidic ground state of multicrystalline materials. It is already shown that the model can describe a variety of material behaviors, including multicrystalline solidification, linear elasticity, coarsening and defect dynamics. Together with Renormalization Group techniques and adaptive mesh refinement, the model can be used to simulate macroscopically large ($\sim mm$) samples over diffusive timescales (sec) within several days using a single core desktop computer. It is a promising tool to multiscale modeling in materials and our work has mainly been to illustrate various fundamental properties of the model.

We first showed that the PFC model can be rewritten in terms of the complex

amplitudes—the spatially varying envelope of the density wave. We showed, in addition, that this complex amplitude representation does incorporate the correct form of nonlinear elasticity. We then studied the plastic properties of the model by applying a shearing force. Dislocation creation, annihilation and avalanches are observed, resembling to the scaling behavior in driven ferromagnetic systems and other dislocation avalanching systems. Critical exponents are extracted from data collapse extending over 5 decades. This shows that the PFC model captures the nonlinear elastic and even plastic properties of multicrystalline materials.

We then noticed that the notion of 'atoms' is not valid in the PFC approach, because the order parameter is not a positive definite quantity and as a result it can form many peaks ('atoms') from a constant field configuration('vacuum'). Because of this, we modified the PFC model to accommodate the actual atomic configurations and vacancies by forbidding the order parameter to be negative. We also calculated the resulting phase diagram for vacancies. By this modification, the PFC model becomes a molecular dynamics simulation machine. We succeeded in simulating a liquid using the model and reproducing the two-point correlation function. Finally, we extended the PFC model to binary systems. The resulting theory was shown to describe both the atomic hopping events on microscopic scales and diffusion on macroscopic scales. By varying the temperature, we also recovered the activated Arrhenius form of the diffusion coefficient.

All these successes show that the PFC model is an excellent approach to study multiscale phenomena in multicrystalline materials. It opens up a whole array of possibilities to model materials across scales. While further applications of the model to other multiscale problems, such as eutectic solidification and precipitation hardening, as well as the extension of the model to three dimensions, are anticipated, the application of the core idea of the PFC approach—to formulate a macroscopic theory with a symmetry consistent with the microscopic phenomenology—to other systems,

such as liquid crystal, complex liquid and even glassy systems, is also a potentially interesting and rewarding direction.

Appendix A

Numerical Implementations

The PFC equation is solved numerically using finite difference methods. A forward Euler method is used to approximate the time derivative and second order central difference method is used to approximate the spatial derivatives. This scheme follows closely from the one Athreya *et al.* used in [62]. We describe the discretization of various operators in this appendix.

A.1 Gradients

A uniform rectangular grid of grid spacing Δx is used throughout all simulations. To avoid any anisotropy introduced from the grid orientation, we approximate the gradient of a function $f(x, y)$ at a grid point $(x_i, y_j) \equiv (i\Delta x, j\Delta x)$ as the average of two central difference schemes—$\nabla_{\oplus} f|_{i,j}$ and $\nabla_{\otimes} f|_{i,j}$—which discretize the gradient in two orthogonal directions. A similar discretization scheme is discussed in [185].

$\nabla_{\oplus} f$ is the central difference scheme in the $x = 0$ and $y = 0$ directions. It is given by

$$\nabla_{\oplus} f_{i,j} \equiv \left(\frac{f_{i+1,j} - f_{i-1,j}}{2\Delta x} \right) \hat{x} + \left(\frac{f_{i,j+1} - f_{i,j-1}}{2\Delta x} \right) \hat{y} + O(\Delta x^2), \tag{A.1}$$

and $\nabla_{\otimes} f$ is the central difference scheme in the $y = \pm x$ directions. It is given by

$$\begin{aligned} \nabla_{\otimes} f|_{i,j} &= \left(\frac{f_{i+1,j+1} - f_{i-1,j-1}}{2\sqrt{2}\Delta x}\right)\left(\frac{\hat{x}+\hat{y}}{\sqrt{2}}\right) \\ &\quad + \left(\frac{f_{i-1,j+1} - f_{i+1,j-1}}{2\sqrt{2}\Delta x}\right)\left(\frac{-\hat{x}+\hat{y}}{\sqrt{2}}\right) + O(\Delta x^2). \end{aligned} \tag{A.2}$$

By taking the average of these two schemes, the gradient is discretized as

$$\nabla f|_{i,j} = \frac{1}{2}\left(\nabla_{\otimes} f|_{i,j} + \nabla_{\oplus} f|_{i,j}\right) + O(\Delta x^2) \tag{A.3}$$

$$\begin{aligned} &= \left(\frac{f_{i+1,j+1} + 2f_{i+1,j} - f_{i-1,j-1} - f_{i-1,j+1} - 2f_{i-1,j} + f_{i+1,j-1}}{8\Delta x}\right)\hat{x} \\ &\quad + \left(\frac{f_{i+1,j+1} + 2f_{i,j+1} - f_{i-1,j-1} + f_{i-1,j+1} - 2f_{i,j-1} - f_{i+1,j-1}}{8\Delta x}\right)\hat{y} \\ &\quad + O(\Delta x^2). \end{aligned} \tag{A.4}$$

A.2 Laplacian

An isotropic discretization scheme for the Laplacian operator can also be obtained by a similar procedure. The resulting discretization is

$$\begin{aligned} \nabla^2 f|_{i,j} &= \frac{f_{i+1,j} + f_{i-1,j} + f_{i,j+1} + f_{i,j-1}}{2\Delta x^2} + \frac{f_{i+1,j+1} + f_{i-1,j-1} + f_{i-1,j+1} + f_{i+1,j-1}}{4\Delta x^2} \\ &\quad - \frac{3f_{i,j}}{\Delta x^2} + O(\Delta x^2). \end{aligned} \tag{A.5}$$

The Fourier transform of this discretization is shown to be a very good approximation of the exact operator, $-k^2$[186].

A.3 Thermal Noise

Non-conserved Gaussian white noise can be generated numerically by the Box-Muller transformation[187]: Suppose x_1 and x_2 are two independent random valuables that are uniformly distributed in the interval $(0, 1]$, then

$$z_1 \equiv \sqrt{-2\ln x_1}\cos(2\pi x_2), \tag{A.6}$$

and,

$$z_2 \equiv \sqrt{-2\ln x_1}\sin(2\pi x_2) \tag{A.7}$$

are two independent random variables with standard normal distributions.

For conserved noise in a partial differential equation

$$\frac{\partial u}{\partial t} = \nabla^2 f(u) + \eta, \tag{A.8}$$

where η is the conserved noise satisfying the fluctuation-dissipation theorems

$$\langle \eta(\vec{x}, t)\eta(\vec{x}', t')\rangle = -\epsilon\nabla^2\delta(\vec{x} - \vec{x}')\delta(t - t'), \tag{A.9}$$

we can rewrite the equation as

$$\frac{\partial u}{\partial t} = \nabla \cdot (\nabla f(u) - \xi), \tag{A.10}$$

where ξ is a vector whose components are independent Gaussian white noise, which can be computed by the Box-Muller transformation described above. The same approach is employed in Ref. [141].

Appendix B

Visualization

In this appendix, we discuss techniques of extracting the locations of PFC atoms, those of defects and the local grain orientation from the order parameter, $\rho(\vec{x}, t)$, of the phase field crystal (PFC) model.

B.1 PFC Atoms

While a quick way to extract the locations of the PFC atoms is to find the maximum (minimum) of the order parameter, $\rho(\vec{x}, t)$, a more accurate method is to first put a threshold in $\rho(\vec{x}, t)$ and digitalize the order parameter by the transformation

$$\rho_{binary} = \begin{cases} 1 & \text{if} \quad \rho(\vec{x}, t) > \bar{\rho} \\ 0 & \text{otherwise,} \end{cases} \tag{B.1}$$

where $\bar{\rho}$ is the threshold. After applying this transformation, all PFC atoms become clusters of pixels with $\rho_{binary} = 1$. We can then locate the atoms by finding the center of each cluster.

B.2 Grain Orientation

After extracting the positions of the PFC atoms, the local grain orientation can be found by computing the angle

$$\phi_i = \theta_i \mod \frac{\pi}{3}, \tag{B.2}$$

where θ_i is the angle between a fixed axis and the line that joins atom i and its nearest neighbor. This method is simple and can easily be implemented, but one has to first find the nearest neighbor of each atom and the resulting orientation field is only defined at the location of the atoms. Some sort of extrapolation has to be done to obtain a continuous orientation field.

A more elaborated method to extract the orientation field is developed by Singer and Singer[150]. They made use of the fact that the ground state of the PFC model is a perfectly triangular state and introduced a two dimensional wavelet transformation

$$\tilde{\rho}(x,y) = \int_{-\infty}^{\infty}\int_{-\infty}^{\infty}\left(\int_{-\infty}^{\infty}\int_{-\infty}^{\infty}\rho(t,u)w_{s_0}(t-v,u-w)dtdu\right)G(v-x,w-y)dvdw, \tag{B.3}$$

where

$$w_{s_0}(x,y) = w_{s_0}(\vec{x}) = \frac{1}{\sqrt{\pi\sigma}}e^{-(x^2+y^2)/2\sigma}(\cos(\vec{k}_{s_0}\cdot\vec{x}) + \cos(\vec{k}_{s_1}\cdot\vec{x}) + \cos(\vec{k}_{s_2}\cdot\vec{x})), \tag{B.4}$$

$$G(x,y) = \frac{1}{\sqrt{\pi\sigma_2}}e^{-(x^2+y^2)/2\sigma_2}, \tag{B.5}$$

and $\vec{k}_{s_0}$, $\vec{k}_{s_1}$ and $\vec{k}_{s_2}$ are the three lattice vectors, σ and σ_2 are two parameters. The wavelet transformation with kernel $w_{s_0}(x,y)$ transform the order parameter to an orientation-dependent function by projecting out the relevant component from the order parameter; the Gaussian transformation smoothes out the remaining atomic-scales oscillations. The result, $\tilde{\rho}(x,y)$, is a function that depends only on the local grain orientation.

B.3 Defects

Because topological defects distort the surrounding orientation field, we can pinpoint the locations of defects by calculating the Laplacian of the orientation field. The locations of defects are places where there is a high value of Laplacian. While this method is fast, it does not work well when the defect density is high—when dislocations are clustered together, for example on a grain boundary, instead of getting distinct points with high Laplacian, one might end up getting a line. It might then be difficult to resolve individual defects.

Another method to extract the defect locations is to count the number of nearest neighbor, N_i, of each PFC atom. Recall that we have $N_i = 6$ for every atom on a perfectly triangular lattice. If the atom is sitting right next to a defect, however, we have $N_i = 5$ or $N_i = 7$. So a quick way to locate the defects is to measure N_i for each atom and those with $N_i \neq 6$ are right next to the defects.

A quick way to measure the number of nearest neighbors is to employ the Delaunay triangulation method in computational geometry[180; 181]. The same methodology is used in [188; 189] in studying coarsening dynamics in 2D hexagonal systems.

It is tempting to try to reconstruct the exact locations of defects from the locations of atoms right next to them. It turned out that this is a difficult task because there are more than one atom sitting next to a single defect and if the defect density is high, it is difficult to tell which atom is sitting next to which defect. Fortunately, in the simulations we have presented in this thesis, the only signal we need is the total speed of the dislocations in the system. This is directly proportional to the total speed of the atoms sitting right next to the dislocations, with the proportionality constant being the mean number of atoms next to the defects. So by simply counting the number of atoms with $N_i \neq 6$ and measuring their speeds, we get the signal we need.

References

[1] N. Goldenfeld, *Lectures on phase transitions and the renormalization group*. Addison-Wesley Reading, MA, 1992.

[2] H. Stanley, "Scaling, universality, and renormalization: Three pillars of modern critical phenomena," *Reviews of Modern Physics*, vol. 71, no. 2, pp. 358–366, 1999.

[3] M. Peskin, *An Introduction to Quantum Field Theory*. Basic Books, 1995.

[4] J. Cardy, *Scaling and renormalization in statistical physics*. Cambridge University Press, 1996.

[5] M. W. Choptuik, "Universality and scaling in gravitational collapse of a massless scalar field," *Phys. Rev. Lett.*, vol. 70, p. 9, Jan 1993.

[6] M. Carfora and K. Piotrkowska, "Renormalization group approach to relativistic cosmology," *Phys. Rev. D*, vol. 52, pp. 4393–4424, Oct 1995.

[7] O. Iguchi, A. Hosoya, and T. Koike, "Renormalization group approach to the einstein equation in cosmology," *Phys. Rev. D*, vol. 57, pp. 3340–3350, Mar 1998.

[8] Y. Sota, T. Kobayashi, K.-i. Maeda, T. Kurokawa, M. Morikawa, and A. Nakamichi, "Renormalization group approach in Newtonian cosmology," *Phys. Rev. D*, vol. 58, p. 043502, Jun 1998.

[9] N. Goldenfeld, "Roughness-Induced Critical Phenomena in a Turbulent Flow," *Physical Review Letters*, vol. 96, no. 4, p. 44503, 2006.

[10] J. Veysey and N. Goldenfeld, "Simple viscous flows: From boundary layers to the renormalization group," *Reviews of Modern Physics*, vol. 79, no. 3, pp. 883–927, 2007.

[11] L. Smith and S. Woodruff, "Renormalization-group analysis of turbulence," *Annual Review of Fluid Mechanics*, vol. 30, no. 1, pp. 275–310, 1998.

[12] N. Goldenfeld, B. P. Athreya, and J. A. Dantzig, "Renormalization group approach to multiscale simulation of polycrystalline materials using the phase field crystal model," *Phys. Rev. E*, vol. 72, p. 020601, 2005.

[13] B. P. Athreya, N. Goldenfeld, and J. A. Dantzig, "Renormalization-group theory for the phase-field crystal equation," *Phys. Rev. E*, vol. 74, p. 011601, 2006.

[14] M. Kardar, G. Parisi, and Y.-C. Zhang, "Dynamic scaling of growing interfaces," *Phys. Rev. Lett.*, vol. 56, pp. 889–892, Mar 1986.

[15] L. Pietronero, A. Vespignani, and S. Zapperi, "Renormalization scheme for self-organized criticality in sandpile models," *Phys. Rev. Lett.*, vol. 72, pp. 1690–1693, Mar 1994.

[16] A. Erzan, L. Pietronero, and A. Vespignani, "The fixed-scale transformation approach to fractal growth," *Reviews of Modern Physics*, vol. 67, no. 3, pp. 545–604, 1995.

[17] J. Sethna, K. Dahmen, and C. Myers, "Crackling noise," *Nature*, vol. 410, pp. 242–250, 2001.

[18] G. Ódor, "Universality classes in nonequilibrium lattice systems," *Reviews of Modern Physics*, vol. 76, no. 3, pp. 663–724, 2004.

[19] G. I. Barenblatt, *Scaling, self-similarity, and intermediate asymptotics*, vol. 14 of *Cambridge Texts in Applied Mathematics*. Cambridge University Press, 1996.

[20] L. Chen, N. Goldenfeld, and Y. Oono, "Renormalization group and singular perturbations: Multiple scales, boundary layers, and reductive perturbation theory," *Physical Review E*, vol. 54, no. 1, pp. 376–394, 1996.

[21] B. Mandelbrot, "Renormalization and fixed points in finance, since 1962," *Physica A*, vol. 263, no. 1, pp. 477–487, 1999.

[22] B. Mandelbrot, *Fractals and scaling in finance: discontinuity, concentration, risk: selecta volume E*. Springer, 1997.

[23] Y. Oono and S. Puri, "Study of phase-separation dynamics by use of cell dynamical systems. I. Modeling," *Physical Review A*, vol. 38, no. 1, pp. 434–453, 1988.

[24] S. Puri and Y. Oono, "Study of phase-separation dynamics by use of cell dynamical systems. II. Two-dimensional demonstrations," *Physical Review A*, vol. 38, no. 3, pp. 1542–1565, 1988.

[25] M. Mondello and N. Goldenfeld, "Scaling and vortex dynamics after the quench of a system with a continuous symmetry," *Physical Review A*, vol. 42, no. 10, pp. 5865–5872, 1990.

[26] M. Mondello and N. Goldenfeld, "Scaling and vortex-string dynamics in a three-dimensional system with a continuous symmetry," *Physical Review A*, vol. 45, no. 2, pp. 657–664, 1992.

[27] A. Murray and C. Paola, "A cellular model of braided rivers," *Nature*, vol. 371, pp. 54–57, 2002.

[28] J. Veysey, *Complex fluid dynamics: From laminar to geophysical flow*. PhD thesis, University of Illinois at Urbana-Champaign, 2006.

[29] N. Goldenfeld and L. Kadanoff, "Simple Lessons from Complexity," *Science*, vol. 284, no. 5411, pp. 87–89, 1999.

[30] R. Batterman, *The Devil in the Details: Asymptotic Reasoning in Explanation, Reduction, and Emergence*. Oxford University Press US, 2002.

[31] H. Martin, *Statistical analysis of highly-correlated systems in biology and physics*. PhD thesis, University of Illinois at Urbana-Champaign, 2004.

[32] K. Vetsigian, *Collective evolution of biological and physical systems*. PhD thesis, University of Illinois at Urbana-Champaign, 2005.

[33] N. Goldenfeld and C. Woese, "Biology's next revolution," *Nature*, vol. 445, p. 369, 2007.

[34] R. B. Griffiths, "Nonanalytic behavior above the critical point in a random Ising ferromagnet," *Phys. Rev. Lett.*, vol. 23, p. 17, 1969.

[35] M. B. Salamon and S. H. Chun, "Griffiths singularities and magnetoresistive manganites," *Phys. Rev. B*, vol. 68, p. 014411, 2003.

[36] P. Chan, N. Goldenfeld, and M. Salamon, "Critical behavior of Griffiths ferromagnets," *Phys. Rev. Lett.*, vol. 97, p. 137201, 2006.

[37] T. D. Lee and C. N. Yang, "Statistical theory of equations of state and phase transitions. i. theory of condensation," *Phys. Rev.*, vol. 87, p. 404, 1952.

[38] A. J. Bray and D. Huifang, "Griffiths singularities in random magnets: Results for a soluble model," *Phys. Rev. B*, vol. 40, p. 6980, 1989.

[39] D. Laundau and K. Binder, *A Guide to Monte Carlo Simulations in Statistical Physics*. Cambridge University Press, 2005.

[40] G. Bhanot, "The Metropolis algorithm," *Reports on Progress in Physics*, vol. 51, no. 3, pp. 429–457, 1988.

[41] D. Rapaport, *The Art of Molecular Dynamics Simulation*. Cambridge University Press, 2004.

[42] J. Haile, *Molecular Dynamics Simulation: Elementary Methods*. Wiley-Interscience, 2001.

[43] P. Hohenberg and W. Kohn, "Inhomogeneous electron gas," *Phys. Rev.*, vol. 136, pp. B864–B871, Nov 1964.

[44] W. Kohn and L. J. Sham, "Self-consistent equations including exchange and correlation effects," *Phys. Rev.*, vol. 140, pp. A1133–A1138, Nov 1965.

[45] M. Levy, "Universal Variational Functionals of Electron Densities, First-Order Density Matrices, and Natural Spin-Orbitals and Solution of the v-Representability Problem," *Proceedings of the National Academy of Sciences*, vol. 76, no. 12, pp. 6062–6065, 1979.

[46] W. Kohn, "Nobel lecture: Electronic structure of matter-wave functions and density functionals," *Rev. Mod. Phys.*, vol. 71, pp. 1253–1266, Oct 1999.

[47] R. Phillips, *Crystals, Defects and Microstructures Modeling Across Scales*. Cambridge University Press, 2001.

[48] R. Nieminen, "From atomistic simulation towards multiscale modelling of materials," *Journal of Physics: Condensed Matter*, vol. 14, no. 11, pp. 2859–2876, 2002.

[49] D. Vvedensky, "Multiscale modelling of nanostructures," *J. Phys.: Condens. Matter*, vol. 16, pp. R1537–R1576, 2004.

[50] E. Tadmor, M. Ortiz, and R. Phillips, "Physics of Condensed Matter: Structure, Defects and Mechanical Properties," *Philos. Mag. A*, vol. 73, no. 6, pp. 1529–1563, 1996.

[51] V. B. Shenoy, R. Miller, E. B. Tadmor, R. Phillips, and M. Ortiz, "Quasicontinuum models of interfacial structure and deformation," *Phys. Rev. Lett.*, vol. 80, pp. 742–745, Jan 1998.

[52] J. Knap and M. Ortiz, "An analysis of the quasicontinuum method," *J. Mech. Phys. Solids*, vol. 49, no. 9, pp. 1899–1923, 2001.

[53] R. Miller and E. Tadmor, "The Quasicontinuum Method: Overview, applications and current directions," *Journal of Computer-Aided Materials Design*, vol. 9, no. 3, pp. 203–239, 2002.

[54] W. E, B. Engquist, and Z. Huang, "Heterogeneous multiscale method: A general methodology for multiscale modeling," *Phys. Rev. B*, vol. 67, p. 092101, Mar 2003.

[55] W. E and Z. Huang, "Matching conditions in atomistic-continuum modeling of materials," *Phys. Rev. Lett.*, vol. 87, p. 135501, Sep 2001.

[56] R. E. Rudd and J. Q. Broughton, "Coarse-grained molecular dynamics and the atomic limit of finite elements," *Phys. Rev. B*, vol. 58, pp. R5893–R5896, Sep 1998.

[57] J. Q. Broughton, F. F. Abraham, N. Bernstein, and E. Kaxiras, "Concurrent coupling of length scales: Methodology and application," *Phys. Rev. B*, vol. 60, pp. 2391–2403, Jul 1999.

[58] C. Denniston and M. Robbins, "Mapping molecular models to continuum theories for partially miscible fluids," *Physical Review E*, vol. 69, no. 2, p. 21505, 2004.

[59] S. Curtarolo and G. Ceder, "Dynamics of an inhomogeneously coarse grained multiscale system," *Phys. Rev. Lett.*, vol. 88, p. 255504, Jun 2002.

[60] K. R. Elder, M. Katakowski, M. Haataja, and M. Grant, "Modeling elasticity in crystal growth," *Phys. Rev. Lett.*, vol. 88, p. 245701, 2002.

[61] K. R. Elder and M. Grant, "Modeling elastic and plastic deformations in nonequilibrium processing using phase field crystals," *Phys. Rev. E*, vol. 70, p. 051605, 2004.

[62] B. P. Athreya, *Phase-Fields and the Renormalization Group: A Continuum Approach to Multiscale Modeling of Materials*. PhD thesis, University of Illinois at Urbana-Champaign, 2006.

[63] K. Dahmen and J. P. Sethna, "Hysteresis, avalanches, and disorder-induced critical scaling: A renormalization-group approach," *Phys. Rev. B*, vol. 53, pp. 14872–14905, Jun 1996.

[64] M. C. Kuntz and J. P. Sethna, "Noise in disordered systems: The power spectrum and dynamic exponents in avalanche models," *Phys. Rev. B*, vol. 62, pp. 11699–11708, Nov 2000.

[65] A. Travesset, R. A. White, and K. A. Dahmen, "Crackling noise, power spectra, and disorder-induced critical scaling," *Phys. Rev. B*, vol. 66, p. 024430, Jul 2002.

[66] M. Zaiser, "Scale invariance in plastic flow of crystalline solids," *Advances in Physics*, vol. 55, no. 1, pp. 185–245, 2006.

[67] M. Miguel, A. Vespignani, S. Zapperi, J. Weiss, and J. Grasso, "Intermittent dislocation flow in viscoplastic deformation," *Nature*, vol. 410, no. 6829, pp. 667–671, 2001.

[68] N. Goldenfeld, P. Y. Chan, and J. Veysey, "Dynamics of Precipitation Pattern Formation at Geothermal Hot Springs," *Physical Review Letters*, vol. 96, no. 25, p. 254501, 2006.

[69] P. Yuen Chan and N. Goldenfeld, "Steady states and linear stability analysis of precipitation pattern formation at geothermal hot springs," *eprint arXiv: 0706.3230*, 2007.

[70] A. Harris and T. Lubensky, "Renormalization-Group Approach to the Critical Behavior of Random-Spin Models," *Physical Review Letters*, vol. 33, no. 26, pp. 1540–1543, 1974.

[71] D. Khmelnitskii, "Phase transition of the second kind in inhomogeneous bodies," *Zh. Eksp. Teor. Fiz*, vol. 68, p. 1960, 1975.

[72] G. Grinstein and A. Luther, "Application of the renormalization group to phase transitions in disordered systems," *Physical Review B*, vol. 13, no. 3, pp. 1329–1343, 1976.

[73] A. J. Bray, "Nature of Griffths phase," *Phys. Rev. Lett.*, vol. 59, p. 586, 1987.

[74] A. J. Bray and M. A. Moore, "Scaling theory of the random-field Ising model," *J. Phys. C: Solid State Phys.*, vol. 18, p. L927, 1985.

[75] J. Ruiz-Lorenzo, "Griffiths singularities in the two-dimensional diluted Ising model," *Journal of Physics A: Mathematical and General*, vol. 30, no. 2, pp. 485–493, 1997.

[76] V. S. Dotsenko, "Griffiths singularities and the replica instantons in the random ferromagnet," *J. Phys. A: Math. Gen.*, vol. 32, p. 2949, 1999.

[77] V. S. Dotsenko, "Griffiths singularity in the random Ising ferromagnet," *J. Stat. Phys.*, vol. 122, p. 197, 2006.

[78] M. B. Salamon and P. Lin, "Colossal magnetoresistance is a Griffiths singularity," *Phys. Rev. Lett.*, vol. 88, p. 197203, 2002.

[79] X. Z. Z. Wei Li, H. P. Kunkel and G. Williams, "Estimates of the critical exponents of single-crystal $La_{0.73}Ba_{0.27}Mno_3$," *Phys. Rev. B*, vol. 70, p. 214413, 2004.

[80] J. Deisenhofer, D. Braak, H. Krug von Nidda, J. Hemberger, R. Eremina, V. Ivanshin, A. Balbashov, G. Jug, A. Loidl, T. Kimura, *et al.*, "Observation of a Griffiths Phase in Paramagnetic $La_{1-x}Sr_xMnO_3$," *Physical Review Letters*, vol. 95, no. 25, p. 257202, 2005.

[81] C. Magen, P. A. Algarabel, L. Morellon, J. P. Araujo, C. Ritter, M. R. Ibarra, P. A. M., and S. J. B., "Obervation of a Griffiths-like Phase in the Magnetocaloric Compound $Tb_5Si_2Ge_2$"," *Phys. Rev. Lett.*, vol. 96, p. 167201, 2006.

[82] C. Itzykson, R. B. Pearson, and J. B. Zuber, "Distribution of zeros in Ising and gauge models," *Nucl. Phys. B*, vol. 220, p. 415, 1983.

[83] C. Binek, "Density of zeros on the lee-yang circle obtained from magnetization data of a two-dimensional Ising ferromagnet," *Phys. Rev. Lett.*, vol. 81, p. 5644, 1998.

[84] R. A. Wooding, "Growth of natural dams by deposition from steady supersaturated shallow flow," *J. Geophysical Res.*, vol. 96, pp. 667–682, 1991.

[85] B. W. Fouke, J. D. Farmer, D. J. D. Marais, L. Pratt, N. C. Sturchio, and M. K. Discipulo, "Depositional facies and aqueous-solid geochemistry of travertine-depositing hot springs (angel terrace, mammoth hot springs, yellowstone national park, usa).," *J. Sed. Res.*, vol. 70, pp. 265–285, 2000.

[86] B. W. Fouke, "Depositional facies and aqueous-solid geochemistry of travertine-depositing hot springs (Angel Terrace, Mammoth Hot Springs, Yellowstone National Park, usa).," *J. Sed. Res.*, vol. 71, pp. 497–500, 2001.

[87] O. Hammer, D. Dysthe, and B. Jamtveit, "The dynamics of travertine terrace formation," *Arxiv preprint physics/0601116*, 2006.

[88] M. B. Short, J. C. Baygents, J. W. Beck, D. A. Stone, R. S. T. III, and R. E. Goldstein, "Stalactite growth as a free-boundary problem: A geometric law and its platonic ideal," *Phys. Rev. Lett.*, vol. 94, pp. 018501–018504, 2005.

[89] M. B. Short, J. C. Baygents, and R. E. Goldstein, "Stalactite growth as a free-boundary problem," *Phys. Fluids*, vol. 17, pp. 083101–083112, 2005.

[90] K. Pye and H. Tsoar, *Aeolian sand and sand dunes*. Unwin Hyman Boston, 1990.

[91] N. Lancaster, *Geomorphology of Desert Dunes*. Routledge, 1996.

[92] R. Kerr and J. Turner, "Crystallization and gravitationally controlled ponding during the formation of mound springs, terraces, and black smoker?flanges," *Journal of Geophysical Research*, vol. 101, no. 11, pp. 25–125, 1996.

[93] L. Goehring, S. Morris, and Z. Lin, "Experimental investigation of the scaling of columnar joints," *Physical Review E*, vol. 74, no. 3, p. 36115, 2006.

[94] A. Murray and C. Paola, "A cellular model of braided rivers," *Nature*, vol. 371, no. 6492, pp. 54–57, 1994.

[95] J. S. Herman and M. M. Lorah, "Co_2 outgassing and calcite precipitation in falling spring creek, Virginia, U.S.A.," *Chemical Geology*, vol. 62, pp. 251–262, 1987.

[96] D. D. Zhang, Y. Zhang, A. Zhu, and X. Cheng, "Physical mechanisms of river waterfall tufa (travertine) formation," *J. Sed. Res.*, vol. 71, pp. 205–216, 2001.

[97] I. Barnes and J. R. O'Neil, "Calcium magnesium carbonate solid solutions from holocene conglomerate cements and travertine in the coast range of California," *Geochimica et Cosmochimica Acta*, vol. 35, pp. 699–718, 1971.

[98] H. S. Chafetz, P. F. Rush, and N. M. Utech, "Microenvironmental controls on mineralogy and habit of caco3 precipitates: an example from an active travertine system," *Sedimentology*, vol. 38, pp. 107–126, 1991.

[99] E. Busenberg and L. N. Plummer, "A comparative study of the dissolution and crystal growth kinetics of calcite and aragonite," in *US Geological Survey, Bulletin 1578* (F. A. Mumpton, ed.), pp. 139–168, 1986.

[100] R. W. Renaut and B. Jones, "Controls on aragonite and calcite precipitation in hot spring travertine at chemurkeu, lake bogoria, kenya," *Canadian Journal of Earth Sciences*, vol. 34, pp. 801–818, 1996.

[101] J. Veysey and N. Goldenfeld, "Watching rocks grow.".

[102] R. Brower, D. Kessler, J. Koplik, and H. Levine, "Geometrical Approach to Moving-Interface Dynamics," *Physical Review Letters*, vol. 51, no. 13, pp. 1111–1114, 1983.

[103] E. Ben-Jacob, N. Goldenfeld, J. S. Langer, and G. Schon, "Dynamics of interfacial pattern formation," *Phys. Rev. Lett.*, vol. 51, pp. 1930–1932, 1983.

[104] R. C. Brower, D. A. Kessler, J. Koplik, and H. Levine, "Geometrical models of interface evolution," *Phys. Rev. A*, vol. 29, pp. 1335–1342, 1984.

[105] J. A. Campbell and T. J. Hanratty, "Mass transfer between a turbulent fluid and a solid boundary: linear theory," *AlChE Journal*, vol. 28, p. 988, 1982.

[106] J. A. Campbell and T. J. Hanratty, "Turbulent velocity fluctuations that control mass transfer to a solid boundary," *AlChE Journal*, vol. 29, p. 215, 1983.

[107] A. Chézy, "Formula to find the uniform velocity that the water will have in a ditch or in a canal of which the slope is known," 1776. File No. 847, Ms. 1915 in the library of Ecole des Ponts et Chaussées. English translation in H. Clemens, On the origin of the Chézy formula, Journal Association of Engineering Societies, v. 18, pp. 363-369, (1897).

[108] B. D. Saint-Venant *Comptes Rendus Académie des Sciences, Paris, Tome 73, July*, 1871.

[109] A. N. Kolmogorov, "Local structure of turbulence in incompressible fluid at a very high reynolds number," *Dokl. Akad. Nauk. SSSR*, vol. 30, pp. 299–302, 1941. [English translation in Proc. R. Soc. London Ser. A 434 (1991)].

[110] K. R. Sreenivasan, "Fluid turbulence," *Rev. Mod. Phys.*, vol. 71, pp. S383–S395, 1999.

[111] R. F. Dressler, "New nonlinear shallow-flow equations with curvature," *J. Hydraul. Res.*, vol. 16, p. 205, 1978.

[112] N. S. Sivakumaran, R. Hosking, and T. Tingsanchali, "Steady shallow flow over a spillway," *J. Fluid Mech.*, vol. 111, p. 411, 1981.

[113] I. Friedman, "Some investigations of the deposition of travertine from hot springs: I. the isotope chemistry of a travertine-depositing spring," *Geochimica et Cosmochimica Acta*, vol. 34, pp. 1303–1315, 1970.

[114] A. Pentecost, "The formation of travertine shrubs: Mammoth hot springs, Wyoming," *Geol. Mag.*, vol. 127, pp. 159–168, 1990.

[115] F. Liu and N. Goldenfeld, "Linear stability of needle crystals in the boundary-layer model of dendritic solidification," *Physical Review A*, vol. 38, no. 1, pp. 407–417, 1988.

[116] M. Barber, A. Barbieri, and J. Langer, "Dynamics of dendritic sidebranching in the two-dimensional symmetric model of solidification," *Physical Review A*, vol. 36, no. 7, pp. 3340–3349, 1987.

[117] R. Pieters and J. Langer, "Noise-Driven Sidebranching in the Boundary-Layer Model of Dendritic Solidification," *Physical Review Letters*, vol. 56, no. 18, pp. 1948–1951, 1986.

[118] R. González-Cinca, L. Ramírez-Piscina, J. Casademunt, and A. Hernández-Machado, "Sidebranching induced by external noise in solutal dendritic growth," *Phys. Rev. E*, vol. 63, p. 051602, Apr 2001.

[119] E. Ben-Jacob, N. Goldenfeld, B. Kotliar, and J. Langer, "Pattern Selection in Dendritic Solidification," *Physical Review Letters*, vol. 53, no. 22, pp. 2110–2113, 1984.

[120] D. Kessler, J. Koplik, and H. Levine, "Geometrical models of interface evolution. III. Theory of dendritic growth," *Physical Review A*, vol. 31, no. 3, pp. 1712–1717, 1985.

[121] G. Bales and A. Zangwill, "Morphological instability of a terrace edge during step-flow growth," *Physical Review B*, vol. 41, no. 9, pp. 5500–5508, 1990.

[122] L.-Q. Chen, "Phase-field modes for microstructure evolution," *Annu. Rev. Mater. Res.*, vol. 32, p. 113, 2002.

[123] J. Cahn and J. Hilliard, "Free energy of a nonuniform system," *IJ Chem Phys*, vol. 28, p. 258, 1958.

[124] A. Wheeler, W. Boettinger, and G. McFadden, "Phase-field model for isothermal phase transitions in binary alloys," *Physical Review A*, vol. 45, no. 10, pp. 7424–7439, 1992.

[125] S. Allen and J. Cahn, "Coherent and incoherent equilibria in iron-rich iron-aluminium alloys," *Acta Metall*, vol. 23, no. 10, pp. 1017–26, 1975.

[126] S. Allen and J. Cahn, "Mechanisms of Phase Transformations Within the Miscibility Gap of Fe Rich Fe-A1 Alloys," *Acta Metallurgica*, vol. 24, pp. 425–437, 1976.

[127] S. Allen and J. Cahn, "A Microscope Theory for Antiphase Boundary Motion and its Application to Antiphase Domain Coarsening," *Acta Metall.*, vol. 27, no. 6, pp. 1085–1095, 1979.

[128] J. Collins and H. Levine, "Diffuse interface model of diffusion-limited crystal growth," *Physical Review B*, vol. 31, no. 9, pp. 6119–6122, 1985.

[129] B. Grossmann, K. Elder, M. Grant, and J. Kosterlitz, "Directional solidification in two and three dimensions," *Physical Review Letters*, vol. 71, no. 20, pp. 3323–3326, 1993.

[130] K. Elder, F. Drolet, J. Kosterlitz, and M. Grant, "Stochastic eutectic growth," *Physical Review Letters*, vol. 72, no. 5, pp. 677–680, 1994.

[131] F. Drolet, K. Elder, M. Grant, and J. Kosterlitz, "Phase-field modeling of eutectic growth," *Physical Review E*, vol. 61, no. 6, pp. 6705–6720, 2000.

[132] A. Karma, "Phase field methods," *Encyclopedia of Materials Science and Technology*, p. 6873, 2001.

[133] J. Warren and W. Boettinger, "Prediction of dendritic growth and microsegregation patterns in a binary alloy using the phase-field method," *Acta Metallurgica Et Materialia*, vol. 43, no. 2, pp. 689–703, 1995.

[134] I. Aranson, V. Kalatsky, and V. Vinokur, "Continuum Field Description of Crack Propagation," *Physical Review Letters*, vol. 85, no. 1, pp. 118–121, 2000.

[135] A. Karma, D. Kessler, and H. Levine, "Phase-Field Model of Mode III Dynamic Fracture," *Physical Review Letters*, vol. 87, no. 4, p. 45501, 2001.

[136] V. Vaithyanathan, C. Wolverton, and L. Chen, "Multiscale Modeling of Precipitate Microstructure Evolution," *Physical Review Letters*, vol. 88, no. 12, p. 125503, 2002.

[137] L. Chen and W. Yang, "Computer simulation of the domain dynamics of a quenched system with a large number of nonconserved order parameters: The grain-growth kinetics," *Physical Review B*, vol. 50, no. 21, pp. 15752–15756, 1994.

[138] N. Moelans, B. Blanpain, and P. Wollants, "A phase field model for the simulation of grain growth in materials containing finely dispersed incoherent second-phase particles," *Acta Materialia*, vol. 53, no. 6, pp. 1771–1781, 2005.

[139] N. Moelans, B. Blanpain, and P. Wollants, "Phase field simulations of grain growth in two-dimensional systems containing finely dispersed second-phase particles," *Acta Materialia*, vol. 54, no. 4, pp. 1175–1184, 2006.

[140] Y. Suwa, Y. Saito, and H. Onodera, "Phase field simulation of grain growth in three dimensional system containing finely dispersed second-phase particles," *Scripta Materialia*, vol. 55, no. 4, pp. 407–410, 2006.

[141] A. Karma and W. Rappel, "Phase-field method for computationally efficient modeling of solidification with arbitrary interface kinetics," *Physical Review E*, vol. 53, no. 4, pp. R3017–R3020, 1996.

[142] K. Elder, M. Grant, N. Provatas, and J. Kosterlitz, "Sharp interface limits of phase-field models," *Physical Review E*, vol. 64, no. 2, p. 21604, 2001.

[143] N. Provatas, M. Greenwood, B. Athreya, N. Goldenfeld, and J. Dantzig, "Multiscale Modeling of Solidification: Phase-field Methods to Adaptive Mesh Refinement," *International Journal of Modern Physics B*, vol. 19, no. 31, pp. 4525–4565, 2005.

[144] R. Kobayashi, J. Warren, and W. Carter, "Vector-valued phase field model for crystallization and grain boundary formation," *Physica D*, vol. 119, no. 3, pp. 415–423, 1998.

[145] R. Kobayashi, J. Warren, and W. Craig Carter, "A continuum model of grain boundaries," *Physica D*, vol. 140, no. 1, pp. 141–150, 2000.

[146] A. E. Lobkovsky and J. A. Warren, "Sharp interface limit of a phase-field model of crystal grains," *Phys. Rev. E*, vol. 63, p. 051605, Apr 2001.

[147] J. Warren, R. Kobayashi, A. Lobkovsky, and W. Craig Carter, "Extending phase field models of solidification to polycrystalline materials," *Acta Materialia*, vol. 51, no. 20, pp. 6035–6058, 2003.

[148] A. Onuki, *Phase Transition Dynamics*. Cambridge University Press, 2002.

[149] A. J. Bray, "Theory of phase ordering kinetics," *Adv. Phys.*, vol. 43, p. 357, 1994.

[150] H. M. Singer and I. Singer, "Analysis and visualization of multiply oriented lattice structures by a two-dimensional continuous wavelet transform," *Phys. Rev. E*, vol. 74, p. 031103, 2006.

[151] P. Stefanovic, M. Haataja, and N. Provatas, "phase-field crystals with elastic interactions," *Phys. Rev. Lett.*, vol. 96, p. 225504, 2006.

[152] J. Berry and M. Grant, "Diffusive atomistic dynamics of edge dislocations in two dimensions," *Phys. Rev. E*, vol. 73, p. 031609, 2006.

[153] C. V. Achim, M. Karttunen, K. R. Elder, E. Granato, T. Ala-Nissila, and S. C. Ying, "Phase diagram and commensurate-incommensurate transitions in the phase field crystal model with an external pinning potential," *Phys. Rev. E*, vol. 74, p. 021104, 2006.

[154] K. Elder, N. Provatas, J. Berry, P. Stefanovic, and M. Grant, "Phase-field crystal modeling and classical density functional theory of freezing," *Physical Review B*, vol. 75, no. 6, p. 64107, 2007.

[155] N. Goldenfeld, O. Martin, Y. Oono, and F. Liu, "Anomalous dimensions and the renormalization group in a nonlinear diffusion process," *Phys. Rev. Lett.*, vol. 64, p. 1361, 1990.

[156] L. Chen, N. Goldenfeld, and Y. Oono, "Renormalization group theory for the modified porous medium equation," *Phys. Rev. A*, vol. 44, p. 6544, 1991.

[157] R. Graham, "Systematic derivation of a rotationally covariant extension of the two-dimensional Newell-Whitehead-Segel equation," *Phys. Rev. Lett.*, vol. 76, p. 2185, 1996.

[158] Y. Shiwa, "Renormalization-group theoretical reduction of the Swift-Hohenberg model," *Phys. Rev. E*, vol. 63, p. 016119, 2000.

[159] K. Nozaki, Y. Oono, and Y. Shiwa, "Reductive use of renormalization group," *Phys. Rev. E*, vol. 62, p. R4501, 2000.

[160] C. M. Bender and S. A. Orszag, *Advanced Mathematical Methods for Scientists and Engineers Asymptotic Methods and Perturbation Theory*. Springer, 233 Spring Street, New York, NY 10013, USA: Springer, 1999.

[161] G. H. Gunaratne, Q. Ouyang, and H. L. Swinney, "Pattern formation in the presence of symmetries," *Phys. Rev. E*, vol. 50, p. 2082, 1994.

[162] N. Provatas, N. Goldenfeld, and J. Dantzig, "Efficient computation of dendritic microstructures using adaptive mesh refinement," *Phys. Rev. Lett.*, vol. 80, p. 3308, 1998.

[163] N. Provatas, N. Goldenfeld, and J. A. Dantzig, "Adaptive mesh refinement computation of solidification microstructures using dynamic data structures," *J. Comp. Phys.*, vol. 148, p. 265, 1999.

[164] J.-H. Jeong, N. Goldenfeld, and J. A. Dantzig, "Phase field model for three-dimensional dendritic growth with fluid flow," *Phys. Rev. E*, vol. 64, p. 041602, 2001.

[165] A. Eringen, *Nonlinear Theory of Continuous Media*. McGraw-Hill, 1962.

[166] R. Atkin and N. Fox, *An introduction to the theory of elasticity*. Longman, 1980.

[167] A. Cottrell, *Dislocations and Plastic Flow in Crystals*. Oxford University Press, 1953.

[168] A. Mendelson, *Plasticity: Theory and Application*. Macmillan New York, 1968.

[169] W. Hosford, *Mechanical Behavior of Materials*. Cambridge University Press, 2005.

[170] J. Hirth and J. Lothe, *Theory of Dislocations*. 1982.

[171] F. Nabarro, *Theory of crystal dislocations*. Dover, 1987.

[172] H. Kleinert, *Gauge fields in condensed matter*. World Scientific Teaneck, NJ, 1989.

[173] J. Weiss, "Scaling of Fracture and Faulting of Ice on Earth," *Surveys in Geophysics*, vol. 24, no. 2, pp. 185–227, 2003.

[174] J. Weiss and J. Grasso, "Acoustic emission in single crystals of ice," *J. Phys. Chem*, vol. 101, pp. 6113–6117, 1997.

[175] T. Richeton, J. Weiss, and F. Louchet, "Breakdown of avalanche critical behaviour in polycrystalline plasticity.," *Nat Mater*, vol. 4, no. 6, pp. 465–9, 2005.

[176] M. Bharathi, M. Lebyodkin, G. Ananthakrishna, C. Fressengeas, and L. Kubin, "Multifractal Burst in the Spatiotemporal Dynamics of Jerky Flow," *Physical Review Letters*, vol. 87, no. 16, p. 165508, 2001.

[177] M. Bharathi and G. Ananthakrishna, "Chaotic and power law states in the Portevin-Le Chatelier effect," *Europhysics Letters*, vol. 60, no. 2, pp. 234–240, 2002.

[178] A. Travesset, R. White, and K. Dahmen, "Crackling noise, power spectra, and disorder-induced critical scaling," *Physical Review B*, vol. 66, no. 2, p. 24430, 2002.

[179] O. Perković, K. Dahmen, and J. Sethna, "Avalanches, Barkhausen Noise, and Plain Old Criticality," *Physical Review Letters*, vol. 75, no. 24, pp. 4528–4531, 1995.

[180] J. Sack and J. Urrutia, *Handbook of computational geometry*. North-Holland Publishing Co. Amsterdam, The Netherlands, The Netherlands, 2000.

[181] J. O'Rourke, *Computational Geometry in C*. Cambridge University Press, 1998.

[182] S. Rice and P. Gray, "The Statistical Mechanics of Simple Liquids (Interscience, New York, 1965)."

[183] P. Résibois and M. de Leener, *Classical kinetic theory of fluids*. John Wiley, 1977.

[184] M. Glicksman, *Diffusion in solids: field theory, solid-state principles, and applications*. J. Wiley, 2000.

[185] J. Sethian and J. Strain, "Crystal growth and dendritic solidification," *Journal of Computational Physics*, vol. 98, no. 2, pp. 231–253, 1992.

[186] H. Tomita, "Preservation of Isotropy at the Mesoscopic Stage of Phase Separation Processes," *Progress of Theoretical Physics*, vol. 85, no. 1, pp. 47–56, 1991.

[187] G. Box and M. Muller, "A Note on the Generation of Random Normal Deviates," *The Annals of Mathematical Statistics*, vol. 29, no. 2, pp. 610–611, 1958.

[188] L. Gómez, E. Vallés, and D. Vega, "Lifshitz-Safran Coarsening Dynamics in a 2D Hexagonal System," *Physical Review Letters*, vol. 97, no. 18, p. 188302, 2006.

[189] C. Harrison, D. Angelescu, M. Trawick, Z. Cheng, D. Huse, P. Chaikin, D. Vega, J. Sebastian, R. Register, and D. Adamson, "Pattern coarsening in a 2D hexagonal system," *Europhysics Letters*, vol. 67, no. 5, pp. 800–806, 2004.

Author's Biography

Pak Yuen Chan was born in Hong Kong SAR, China. He enrolled in the undergraduate program in the Department of Physics at the Chinese University of Hong Kong in 2000. After receiving his B.S. in Physics in 2003, he entered the graduate program in the Department of Physics at the University of Illinois at Urbana-Champaign and joined Nigel Goldenfeld's research group.